

## RESEARCH ARTICLE

10.1002/2017JB014501

## MMA-EoS: A Computational Framework for Mineralogical Thermodynamics

## Key Points:

- We present a new open-source Gibbs energy minimizer MMA-EoS for mantle mineralogy that incorporates existing thermodynamics models
- We emphasize code validation by comparison to previous results and available experimental data, with increasing complexity of composition
- We evaluate homogeneous mantle composition versus mechanical mixture of slab components in interpreting 1-D seismic profiles

## Supporting Information:

- Supporting Information S1
- Text S1
- Figure S1
- Figure S2
- Figure S3
- Figure S4
- Figure S5
- Figure S6
- Figure S7
- Figure S8
- Figure S9
- Figure S10
- Figure S11
- Figure S12
- Figure S13
- Figure S14
- Table S1
- Table S2
- Table S3

## Correspondence to:

T. C. Chust,  
thomas.chust@uni-bayreuth.de

## Citation:

Chust, T. C., Steinle-Neumann, G., Dolejs, D., Schuberth, B. S., & Bunge, H. P. (2017). MMA-EoS: A computational framework for mineralogical thermodynamics. *Journal of Geophysical Research: Solid Earth*, 122, 9881–9920. <https://doi.org/10.1002/2017JB014501>

Received 31 MAY 2017

Accepted 12 NOV 2017

Accepted article online 17 NOV 2017

Published online 26 DEC 2017

T. C. Chust<sup>1,2</sup>, G. Steinle-Neumann<sup>1</sup>, D. Dolejs<sup>3</sup>, B. S. A. Schuberth<sup>2</sup>, and H.-P. Bunge<sup>2</sup>
<sup>1</sup>Bayerisches Geoinstitut, Universität Bayreuth, Bayreuth, Germany, <sup>2</sup>Department of Earth and Environmental Sciences, Geophysics Section, Ludwig-Maximilians-Universität München, Munich, Germany, <sup>3</sup>Institute of Earth and Environmental Sciences, Albert-Ludwigs-Universität Freiburg, Freiburg, Germany

**Abstract** We present a newly developed software framework, MMA-EoS, that evaluates phase equilibria and thermodynamic properties of multicomponent systems by Gibbs energy minimization, with application to mantle petrology. The code is versatile in terms of the equation-of-state and mixing properties and allows for the computation of properties of single phases, solution phases, and multiphase aggregates. Currently, the open program distribution contains equation-of-state formulations widely used, that is, Caloric-Murnaghan, Caloric-Modified-Tait, and Birch-Murnaghan–Mie-Grüneisen-Debye models, with published databases included. Through its modular design and easily scripted database, MMA-EoS can readily be extended with new formulations of equations-of-state and changes or extensions to thermodynamic data sets. We demonstrate the application of the program by reproducing and comparing physical properties of mantle phases and assemblages with previously published work and experimental data, successively increasing complexity, up to computing phase equilibria of six-component compositions. Chemically complex systems allow us to trace the budget of minor chemical components in order to explore whether they lead to the formation of new phases or extend stability fields of existing ones. Self-consistently computed thermophysical properties for a homogeneous mantle and a mechanical mixture of slab lithologies show no discernible differences that require a heterogeneous mantle structure as has been suggested previously. Such examples illustrate how thermodynamics of mantle mineralogy can advance the study of Earth's interior.

## 1. Introduction

Knowledge of stable phase assemblages and their material properties is a prerequisite in diverse areas of geosciences, material sciences, and chemistry. Examples include the geophysical interpretation of seismic wave speed variations imaged by tomography (e.g., Cobden et al., 2008; Matas et al., 2007; Schuberth et al., 2009a) or the construction of geodynamic models of mantle convection (e.g., Ita & King, 1994, 1998; Schuberth et al., 2009b; Simmons et al., 2009) but also engineering topics such as rocket engine design (e.g., McBride et al., 2002). Strategies to determine phase stability and compute the material properties rely on thermodynamic models and use various mathematical methods such as linear or nonlinear optimization (e.g., Bale et al., 2009; Connolly, 2005; Dantzig, 1963; Eriksson & Rosen, 1973) or nonlinear equation solvers (e.g., Ohtani, 2006; Powell et al., 1998). Models use internally consistent thermodynamic data sets to describe the behavior of minerals and other materials (Aranovich & Berman, 1996; Berman & Aranovich, 1996; Fabrichnaya et al., 2004; Holland & Powell, 1998, 2011; Stixrude & Lithgow-Bertelloni, 2005a, 2011), and they share the fundamental principle that phase stability criteria are specified in terms of a thermodynamic potential. Pressure  $P$ , temperature  $T$ , and bulk composition  $x$  often form the most convenient choice of independent variables, with Gibbs energy being the corresponding potential. The stable phase assemblage is then obtained by minimizing Gibbs energy of the system (e.g., de Capitani & Brown, 1987; Stowe, 2007; White et al., 1958).

The functional form of Gibbs energy also includes sufficient information to derive equilibrium thermodynamic properties linked to the state of the system and its phases, for example, density, compressibility, or heat capacity. A thermodynamic model for mineral phases and aggregates, that is, bulk material or a rock, provides a natural framework to analyze the dependence of these thermomechanical properties on  $P$ ,  $T$ , and  $x$  and to determine their relationships consistently. Combined with the possibility to compute phase assemblages, thermodynamics offers a comprehensive solution for modeling equilibrium properties of geological

materials, interpolation between experimental results, or extrapolation to conditions that may not be readily accessible in experiments. In the context of mineral physics of Earth's interior, models that have superior extrapolation behavior to very high pressures are particularly valuable.

In a very limited number of cases, conditions of chemical equilibrium between some phases can be determined analytically, for example, by matching the chemical potentials of coexisting binary solutions. Such strategies can be found in software like Thermo-Calc (Powell et al., 1998) and SOLV CALC (Wen & Nekvasil, 1994). Alternatively, Gibbs energy can be minimized with linear algebraic algorithms, as in the widely used petrological and geochemical software packages MELTS (e.g., Asimow & Ghiorso, 1998; Ghiorso & Sack, 1994, 1995), Perple\_X (Connolly, 2005), or Theriak (e.g., de Capitani & Petrakakis, 2010). In our work we take an approach similar to Perple\_X or Theriak, where the mathematical formulation of Gibbs energy minimization is essentially a linear programming problem, complicated by the presence of solution phases, which introduce nonlinearity. In terms of computational speed, such algorithms scale well to dozens of phases (Spielman & Teng, 2001); only the processing of the nonlinear behavior of individual solutions can negatively affect the performance.

In this manuscript we introduce a new open-source phase equilibrium solver for application in mantle petrology, MMA-EoS, which independently implements various thermodynamic formulations, tests their internal consistency, and facilitates the construction of new model combinations or extensions. The code is built as a combination of easily interpretable interfaces and native code for performance critical tasks. The former allows for easy and flexible manipulation of input and output, while the latter assures good performance on a wide range of computer platforms, including clusters with parallelization through MPI support.

We start this manuscript with a review of the thermodynamic principles underlying MMA-EoS, where we build up the model with increasing complexity. Section 2 provides an overview of the concepts, while details for different models and approaches are presented in section S1 of the supporting information in a comprehensive way. We start with the description of various choices for the equation-of-state of individual phases, address the formulation of solution properties, before we discuss aggregate properties. Similarly, the programming approach taken in the construction of MMA-EoS are presented in terms of the general approach in section 3, while implementation details are given in the supporting information (section S2). We then illustrate the use of the thermodynamic models by examples, with the same increasing complexity as in the model description, compare to available data and other thermodynamic results, and critically assess differences and shortcomings of available models (sections 4, 5, and 7.1). MMA-EoS has no implicit temperature and pressure limitations and can be applied to all conditions for which the thermodynamic database in use has been calibrated. With the model parameters by Stixrude and Lithgow-Bertelloni (2011), the software is applicable to pressures and temperatures throughout the entire mantle of the Earth. Results on phase relations for mantle compositions and associated physical properties are then compared to geophysical observations and models of mantle structure (sections 6 and 7.2). Symbols and notations used throughout the paper are summarized in Table 1.

## 2. Thermodynamic Models

Thermodynamic properties of pure, stoichiometric substances are related to reference conditions, usually  $T_0 = 298.15$  K and  $P_0 = 10^5$  Pa (1 bar). Calculating Gibbs energy of a pure phase at  $P$  and  $T$  of interest requires a theoretical or empirical physical model, that is, an equation-of-state (e.g., Connolly, 2009; Poirier, 2000). Conventionally, most models combine two additive energy contributions, which are computed along two alternative integration path segments (Figure 1):

1. isobaric heating to  $T$  at  $P_0$  (caloric contribution), followed by isothermal compression to  $P$  at constant  $T$  (elastic contribution):

$$G(P, T) = G_0 + [G(P_0, T)]_{T_0}^T + [G(P, T)]_{P_0}^P, \quad (1)$$

or

2. isothermal compression to  $P$  at  $T_0$  (elastic contribution), followed by isochoric heating to  $T$  at constant  $V = V(P, T_0)$  (thermal contribution):

$$G(P, T) = G_0 + [G(P, T_0)]_{P_0}^P + [G(V, T)]_{T_0}^T, \quad (2)$$

where the thermal contribution to Gibbs energy ( $G$ ) is obtained through the relation to Helmholtz energy ( $A$ ):

$$G(V, T) = A(V, T) + P(V, T) \cdot V. \quad (3)$$

**Table 1**  
Summary of Symbols and Notations Used in the Current Manuscript

Description	Symbol	SI units
<i>Thermodynamic Potentials</i>		
Internal energy	$E$	$\text{J mol}^{-1}$
Enthalpy	$H$	$\text{J mol}^{-1}$
Gibbs energy	$G$	$\text{J mol}^{-1}$
Additional Gibbs energy in Landau model	$G_L$	$\text{J mol}^{-1}$
Helmholtz energy	$A$	$\text{J mol}^{-1}$
Interaction energy in solution model	$W$	$\text{J mol}^{-1}$
<i>First-Order Derivatives</i>		
Pressure	$P$	Pa
Phase transition pressure	$P_{\text{tr}}$	Pa
Thermodynamic temperature	$T$	K
Molar volume	$V$	$\text{m}^3 \text{mol}^{-1}$
Total volume	$V_{\text{tot}}$	$\text{m}^3$
Maximum volume of disorder in Landau model	$V_{L,\text{max}}$	$\text{m}^3 \text{mol}^{-1}$
Entropy	$S$	$\text{J K}^{-1} \text{mol}^{-1}$
Configurational entropy	$S_{\text{cf}}$	$\text{J K}^{-1} \text{mol}^{-1}$
<i>Elastic Parameters</i>		
Isothermal compressibility	$\beta$	$\text{Pa}^{-1}$
Isothermal bulk modulus	$K$	Pa
Adiabatic bulk modulus	$\kappa$	Pa
Adiabatic shear modulus	$\mu$	Pa
P-wave velocity	$v_p$	$\text{m s}^{-1}$
S-wave velocity	$v_s$	$\text{m s}^{-1}$
Mass density	$\rho$	$\text{kg m}^{-3}$
<i>Thermal Parameters</i>		
Thermal expansivity	$\alpha$	$\text{K}^{-1}$
Heat capacity at constant pressure	$C_p$	$\text{J K}^{-1} \text{mol}^{-1}$
Heat capacity at constant volume	$C_v$	$\text{J K}^{-1} \text{mol}^{-1}$
Maximum entropy of disorder in Landau model	$S_{L,\text{max}}$	$\text{J K}^{-1} \text{mol}^{-1}$
Critical temperature	$T_C$	K
Debye temperature	$\theta_D$	K
Einstein temperature	$\theta_E$	K
Grüneisen parameter	$\gamma$	
Logarithmic volume derivative of the Grüneisen parameter	$q$	
<i>Other Quantities</i>		
Molar mass	$M$	$\text{kg mol}^{-1}$
Total mass	$M_{\text{tot}}$	kg
Number of atoms per formula unit	$N$	
Mole fraction	$x$	
Mole amount	$X$	mol
Shear strain derivative of the Grüneisen parameter	$\eta_S$	
Third-order Debye function	$D_3$	
Landau model order parameter	$Q$	
Solution model end-member size parameter	$d$	
Subscript for reference conditions	$X_0$	
Subscript for elastic part	$X_{\text{el}}$	
Subscript for thermal part	$X_{\text{th}}$	
Subscript for ordered phase used in Landau model	$X_{\text{ord}}$	
Subscript for disordered phase used in Landau model	$X_{\text{dis}}$	

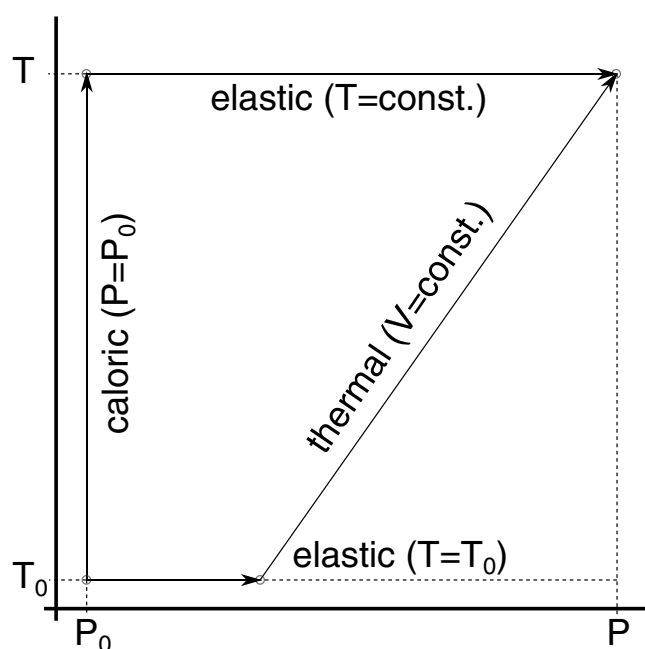


**Figure 1.** Integration path segments in  $P$ - $T$  space used in the physical models implemented in the MMA-EoS software. Starting at reference conditions ( $P_0$ ,  $T_0$ ), the computation of Gibbs energy of a phase may follow either isobaric heating at  $P_0$  (caloric) and then isothermal compression at  $T$  (elastic) or isothermal compression at  $T_0$  (elastic) and then isochoric heating (thermal), keeping the volume fixed.

The caloric contribution in equation (1) has traditionally been modeled using isobaric heat capacity ( $C_p$ ), which is frequently described by polynomials of  $T$ , calibrated by experimental measurements. The functional form of the heat capacity polynomials remains empirical, which can result in poor extrapolation behavior to low or high  $T$ . In addition, such integration paths may pass through unstable regions, for which the calibration for  $C_p$  is not applicable. By contrast, the thermal contribution at constant volume in equation (2) is well suited for an analytical treatment based on statistical mechanics, such as in the Einstein or Debye model (e.g., Poirier, 2000). This approach achieves acceptable extrapolation behavior and predictions of theoretical limits at the expense of accurate reproduction of experimental data.

The isothermal elastic contribution in either equation (1) or (2) is frequently based on a second- or third-order Birch-Murnaghan equation-of-state (e.g., Poirier, 2000).

In caloric models, the temperature effect on volume and compressibility is typically incorporated through phenomenological models using thermal expansivity and/or heat capacity (e.g., Fabrichnaya et al., 2004; Holland & Powell, 1998; Matas, 1999). The approximations for thermal expansivity, similar to  $C_p$ , are mainly empirical polynomials with fitted or inferred coefficients. Thermodynamic consistency of such a combined model is not always guaranteed (Brosh et al., 2007). In assessing a thermodynamic model applicable to Earth's upper mantle and transition zone, Holland and Powell (2011) and Holland et al. (2013) adopted the polynomial caloric approximation, combined with the modified Tait equation-of-state, to calibrate more than 250 mineral phases and melt species.

Stixrude and Lithgow-Bertelloni (2005a, 2011) have refined the physical model of Ita and Stixrude (1992) based on the Birch-Murnaghan–Mie–Grüneisen–Debye theory and compiled a thermodynamic data set for many relevant mantle phases, which has been used widely in geophysical studies of mantle structure (e.g., Cobden et al., 2008, 2009; Cammarano et al., 2011; Davies et al., 2012; Nakagawa et al., 2009; Schuberth et al., 2012, 2015).

Details of the model formulations by Fabrichnaya et al. (2004) (Caloric–Murnaghan), Holland et al. (2013) (Caloric–Modified–Tait) and Stixrude and Lithgow-Bertelloni (2005a, 2011) (Birch–Murnaghan–Mie–Grüneisen–Debye) are presented in the supporting information (sections S1.1–S1.3). The MMA-EoS software implements these three models to calculate Gibbs energy of condensed phases at elevated pressure and temperature.

Thermodynamic properties of minerals with a second-order phase transition (e.g.,  $\alpha$ -quartz– $\beta$ -quartz or stishovite– $\text{CaCl}_2$ -structured  $\text{SiO}_2$ ) or with changes in element ordering between multiple crystallographic sites (e.g., feldspar or spinel) are treated with order-disorder theory. Carpenter et al. (1994) and Holland and Powell (1998) introduced the Landau tricritical theory to mineral physics applications. There, the standard thermodynamic properties refer to a completely disordered phase ( $G_{\text{dis}}$ ) and the Landau contribution ( $G_L$ ), which accounts for progressive ordering with decreasing temperature, is added to obtain a value for the partially ordered phase ( $G_{\text{ord}}$ ):

$$G_{\text{ord}}(P, T) = G_{\text{dis}}(P, T) + G_L(P, T). \quad (4)$$

The treatment of  $G_L$  is discussed further in section S1.5 of the supporting information.

Numerous minerals of geological and geophysical interest have variable chemical composition and are described as solutions. Their thermodynamic properties consist of a linear combination of end-member properties (mixing), configurational (ideal), and excess (nonideal) mixing contributions (e.g., Ganguly, 2008; Hillert & Steffansson, 1970):

$$G = \sum_i x_i G_i - TS_{\text{cf}} + G_{\text{ex}}, \quad (5)$$

where  $i$  refers to the solution end-members and  $G_i$  is their standard Gibbs energy.  $S_{\text{cf}}$  represents the configurational entropy of the solution, and  $G_{\text{ex}}$  is the excess Gibbs energy of mixing. The treatment of the configurational and excess contributions to Gibbs energy in solutions is detailed in section S1.6.

Thermodynamic and other properties of mineral assemblages or multiphase aggregates are computed as linear combinations with appropriate weights. Different properties (extensive versus elastic) require different weights, as discussed further in the supporting information (section S1.7).

### 3. Software Implementation

MMA-EoS is a software package that performs calculations of phase equilibria and associated material properties, individually or for a multiphase aggregate. This scope of functionality is similar to other multicomponent Gibbs energy minimizers such as Perple\_X (Connolly, 2005), Theriak (de Capitani & Petrakakis, 2010), or HeFESTo (Stixrude & Lithgow-Bertelloni, 2005a, 2011). In contrast to many of the other software packages applicable, MMA-EoS is distributed freely, both as source code and in executable form. An open-source distribution guarantees transparency in several aspects: it permits users not only to check, debug, and test the source code but also to seamlessly integrate other tasks. As such, the implementation itself can be verified independently and computations using the software are reproducible. We have programmed MMA-EoS in a modular way to make it easily extensible to various equation-of-state formulations or mixing models beyond the symmetric version implemented currently. With the distribution of the source code, MMA-EoS is portable to a wide range of platforms and can take advantage of system-specific features, such as optimized linear algebra routines, MPI parallelization support, and low-level memory management.

The central task of a phase equilibrium computation is the solution to the optimization problem defined by minimizing Gibbs energy of a multiphase assemblage, whose identity is not known a priori. The total Gibbs energy of all candidate phases forms a linear objective function that is minimized. We use the `lp_solve` library (<http://lpsolve.sourceforge.net/5.5/>) to solve this algebraic problem. The library has been embedded in the MMA-EoS package and customized for safe memory management. The optimization process implemented in MMA-EoS consists of three steps:

1. The Gibbs energies of all candidate phases are computed using their equations-of-state; solid solutions are represented by one or more candidates with constant composition. This step uses thermodynamic parameters from a configurable database file;
2. Linear optimization selects a set of phases with minimal Gibbs energy, subject to the constraint of bulk composition. The number of phases corresponds to the number of independent system components, as required by the phase rule for two degrees of freedom ( $P, T$ );
3. Nonlinear optimization attempts to improve the solution compositions.

Steps (1) through (3) are repeated until no further improvement for the current phase assemblage and its composition can be found. After a stable phase assemblage has been determined, aggregate material properties may be computed, which in turn rely on single-phase properties.

The implementation of MMA-EoS contains three main areas of functionality (Figure S2):

1. the core of MMA-EoS implements the basic infrastructure to manage a collection of phases, provides uniform access to all kinds of phases, solutions, and aggregates, and offers generic implementations of functionality applicable to any physical model;
2. each of the thermodynamic models described in sections 2 and S1 is implemented as an independent module, but with common, uniform interfaces as defined by the core;
3. the Gibbs energy optimizer forms a separate module that extends collections of phases with functionality to compute a stable assemblage.

The high degree of modularization ensures extensibility of the software and its usefulness as a “toolbox” that can be integrated in other work. MMA-EoS can process input and output in easily scriptable data formats, including spreadsheet applications, text processing languages, such as AWK, or plotting tools (e.g., GMT Wessel et al., 2013, or gnuplot). In that sense it can be handled in a similar way as the BurnMan thermoelastic “toolbox” for mantle structure (Cottaar et al., 2014) that is entirely programmed in Python. At the same time, the command line interface of MMA-EoS makes it very suitable for applications on supercomputers and linux clusters, for which we provide MPI support. In addition, the modules are easily extracted



from the MMA-EoS package and may also be used as programming libraries for other applications. Similar to the output, the database entries are clearly structured, such that they can be manipulated easily. Further details of the code, including language choice and numerical implementation are provided in section S2 of the supporting information.

MMA-EoS can be accessed and downloaded from the project website, where extensive documentation and examples are provided (<https://bitbucket.org/chust/eos>). In particular, material is deposited that allows for a direct reproduction of all figures presented in the current manuscript. We have also set up a forum that facilitates discussion among users and between users and the authors (<https://mma-eos.slack.com>).

## 4. Basic Phase Equilibria and Property Parameters

### 4.1. Mineral Properties

We compute volumetric, caloric, and energetic properties of representative silicate phases over a wide  $P$ - $T$  range using the thermodynamic data sets by Stixrude and Lithgow-Bertelloni (2011) for the Birch-Murnaghan–Mie-Grüneisen-Debye model and Holland et al. (2013) for the Caloric–Modified-Tait model. In the following discussion, we have retained all thermodynamic parameters as calibrated in the original studies (Holland et al., 2013; Stixrude & Lithgow-Bertelloni, 2011) in order to preserve internal consistency of each data set.

#### 4.1.1. Volumetric Properties

To examine whether differences in model formulation lead to systematically different behavior of volumetric properties, we have computed molar volumes of forsterite ( $\text{Mg}_2\text{SiO}_4$ ) and bridgmanite ( $\text{MgSiO}_3$ ) over a wide  $P$ - $T$  range using the thermodynamic models by Stixrude and Lithgow-Bertelloni (2011), Holland et al. (2013), and Fabrichnaya et al. (2004) (Figure 2). Isothermal compression, at 300 K and isobaric thermal expansion show very similar behavior in all three models close to ambient conditions but progressively diverge at higher  $P$  or  $T$ . Both the Birch-Murnaghan–Mie-Grüneisen-Debye model and the Caloric–Modified-Tait model have similar expressions for compression (section S1 in the supporting information), and results for  $V(P, T_0)$  are essentially identical (Figure 2). By contrast, the volume expression for the Caloric-Murnaghan model has a different structure and the calibration leads to a noticeably different  $P$  dependence in volume for both phases; at higher  $P$ , larger volumes are computed by the model and calibration of Fabrichnaya et al. (2004).

The  $T$  dependence of molar volume of forsterite and bridgmanite at 1 bar (Figure 2) reflects the fact that both caloric models (Fabrichnaya et al., 2004; Holland et al., 2013) use the same  $C_p$ -based formulation of thermal energies. Both models exhibit similarly shaped  $V$ - $T$  curves with some offset caused by differences in the parameter sets. The Birch-Murnaghan–Mie-Grüneisen-Debye model differs from the other two models in its treatment of Helmholtz energy between ambient and elevated  $T$ , hence it shows physically different expansion behavior. For bridgmanite, the calibration by Stixrude and Lithgow-Bertelloni (2011) exhibits a stronger volume expansion than the other two models and agrees better with the trend of experimental data at higher  $T$ , especially those of Utsumi et al. (1995).

Overall, the volumetric properties predicted by the different formulations show how fundamental differences in capturing experimental data and fitting strategies affect specific parameterizations rather than the inability of the physical theory and functional form of the equation-of-state to represent material properties.

#### 4.1.2. Caloric Properties

The principally different formulations of heat capacity in the caloric model versus the Debye model lead to a trade-off between the fit to calorimetric data and extrapolation behavior at high  $T$  that we explore in terms of  $C_p$  and entropy (Figure 3) and Gibbs energy (Figure S4). For  $C_p$ , the polynomial formulation by Holland et al. (2013) shows a significantly shallower slope at low  $T$  and a steeper increase at high  $T$  than the Debye model as parameterized by Stixrude and Lithgow-Bertelloni (2011). The experimental data for forsterite and fayalite that extend to 1700 K and 800 K (Robie et al., 1982; Robie & Hemingway, 1995; Watanabe, 1982), respectively, are more closely reproduced by the calibration of Holland et al. (2013) (Figure 4). For the  $\text{Fe}_2\text{SiO}_4$  polymorphs, differences between the models of Holland et al. (2013) and Stixrude and Lithgow-Bertelloni (2011) are even more pronounced, and increase with  $T$ .

Owing to the physically correct limiting behavior of the Debye model for the isochoric heat capacity (section S1.3 in the supporting information), the continued steep increase in  $C_p$  in the polynomial model by Holland et al. (2013) appears unphysical. This is confirmed by realizing that the isochoric heat capacity of fayalite exceeds the Dulong-Petit limit for insulators ( $\sim 25 \text{ J K}^{-1} \text{ mol}^{-1} \text{ atom}^{-1}$ ) by  $\sim 3 \text{ J K}^{-1} \text{ mol}^{-1} \text{ atom}^{-1}$ .

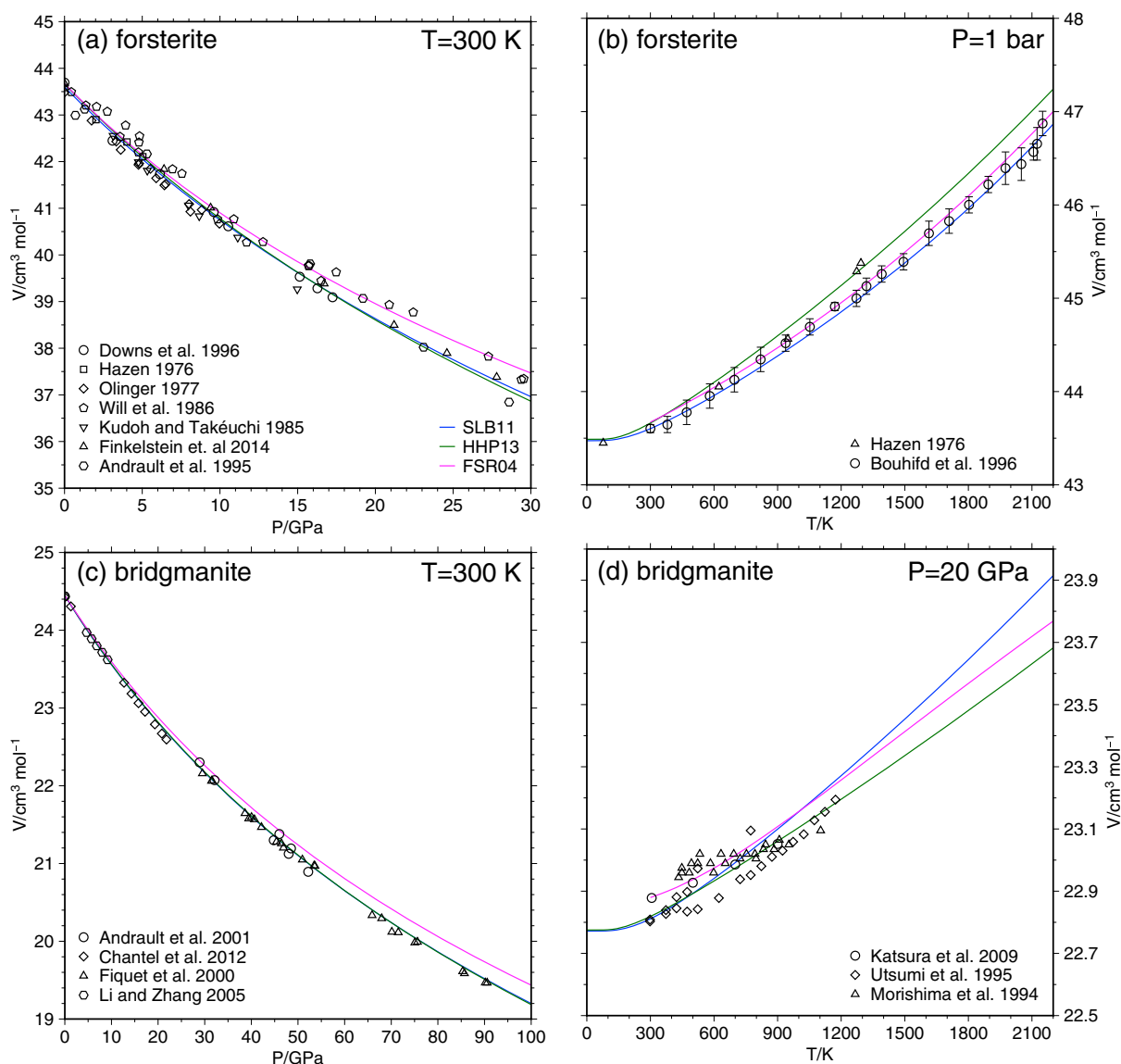


**Figure 2.** Molar volumes for (a and b) forsterite ( $\text{Mg}_2\text{SiO}_4$ ) and (c and d) bridgmanite ( $\text{MgSiO}_3$ ), computed with the MMA-EoS software using the model parameters from Stixrude and Lithgow-Bertelloni (2011) (blue lines), Holland et al. (2013) (green lines), and Fabrichnaya et al. (2004) (magenta lines), as a function of  $P$  (Figures 2a and 2c) and  $T$  (Figures 2b and 2d). In Figure 2a, symbols show experimental data by Hazen (1976) (squares), Olinger (1977) (diamonds), Kudoh and Takeuchi (1985) (inverted triangles), Will et al. (1986) (pentagons), Andraut et al. (1995) (hexagons), Downs et al. (1996) (circles), and Finkelstein et al. (2014) (triangles). In Figure 2b, symbols show experimental values by Hazen (1976) (triangles) and Bouhifd et al. (1996) (circles with error bars). In Figure 2c, symbols show experimental data by Fiquet et al. (2000) (triangles), Andraut et al. (2001) (circles), Li and Zhang (2005) (hexagons), and Chantel et al. (2012) (diamonds). In Figure 2d, symbols show experimental measurements between 19 GPa and 21 GPa by Morishima et al. (1994) (triangles), Utsumi et al. (1995) (diamonds), and Katsura et al. (2009) (circles).

The nature of the Debye approximation used in the model of Stixrude and Lithgow-Bertelloni (2011) prevents a more accurate heat capacity fit for many phases as seen for olivine and fayalite at lower temperatures (Figure 4). The Debye model assumes that heat is stored entirely in the form of acoustic lattice vibrations that have a linear dispersion curve, and this leaves a single parameter, the Debye temperature  $\theta_D$  to capture the phonon spectrum.

The deviations in  $C_p$  for the  $\text{Mg}_2\text{SiO}_4$  polymorphs are less significant when integrated to entropy (Figure 3), and both the Caloric-Modified-Tait and Birch-Murnaghan-Mie-Grüneisen-Debye models describe the entropy of forsterite (Robie & Hemingway, 1995) equally well. For the  $\text{Fe}_2\text{SiO}_4$  polymorphs, heat capacities of fayalite and Fe-wadsleyite are degenerate in the model by Holland et al. (2013) (Figure 3), but the difference in entropy at  $T_0$  results in larger entropy for fayalite, consistent with the model of Stixrude and Lithgow-Bertelloni (2011).

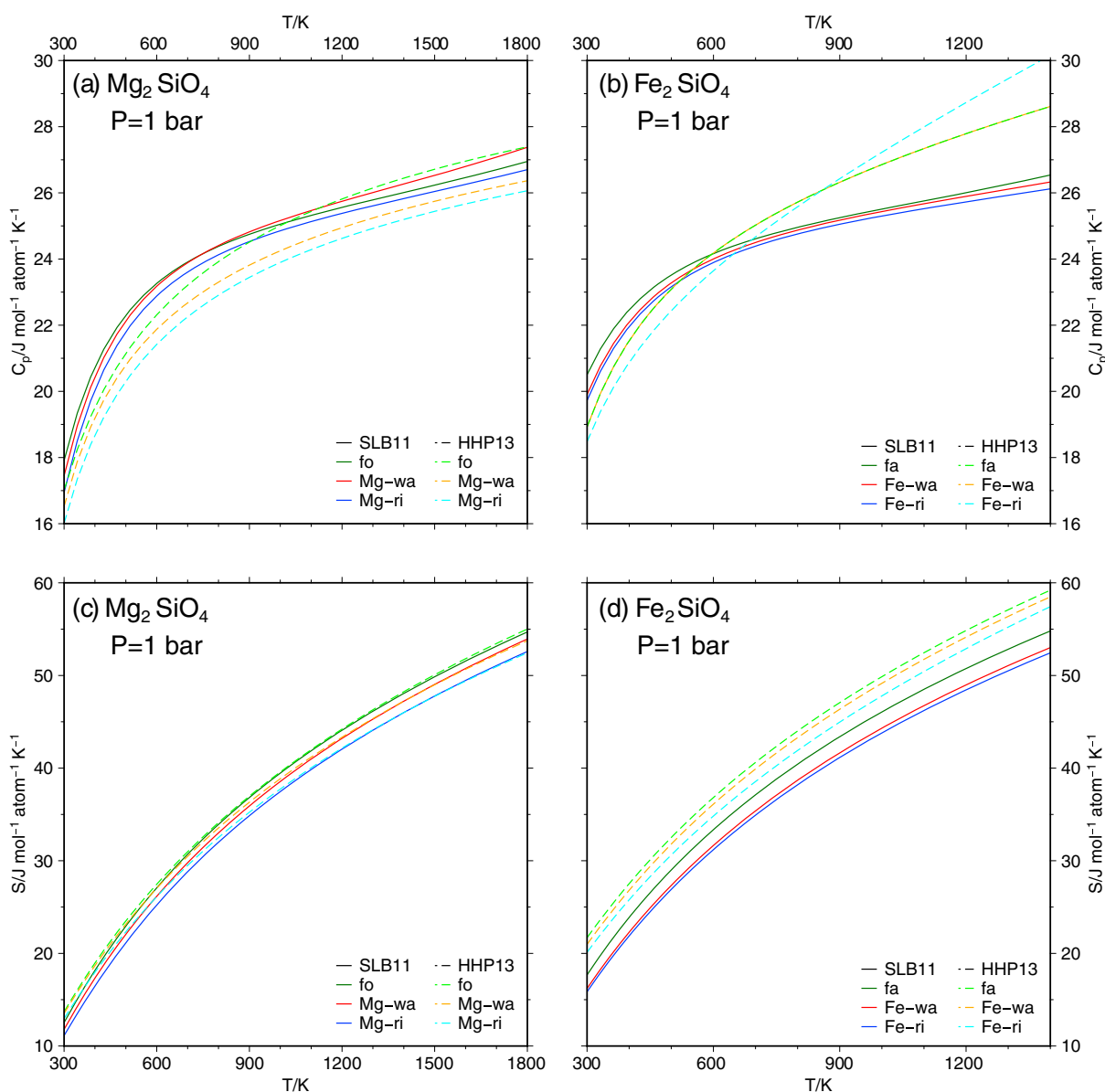


**Figure 3.** Thermal properties of olivine polymorphs at ambient  $P$  computed with MMA-EoS using the model parameters from Stixrude and Lithgow-Bertelloni (2011) (solid lines) and Holland et al. (2013) (dashed lines) as a function of  $T$ . (a and b) Heat capacity per mole of atoms, (c and d) entropy per mole of atoms. Figures 3a and 3c contain the properties of the  $\text{Mg}_2\text{SiO}_4$ -polymorphs forsterite (green), Mg-wadsleyite (red), and Mg-ringwoodite (blue). Figures 3b and 3d show the properties of the  $\text{Fe}_2\text{SiO}_4$ -polymorphs fayalite (green), Fe-wadsleyite (red), and ahrensrite (Fe-ringwoodite, blue). The  $T$  scale differs for the  $\text{Mg}_2\text{SiO}_4$  and  $\text{Fe}_2\text{SiO}_4$ -polymorphs.

However, entropies predicted for both fayalite and Fe-wadsleyite by the model of Holland et al. (2013) remain significantly larger than those of Stixrude and Lithgow-Bertelloni (2011).

Values and uncertainties of volumetric and caloric properties propagate through integration into Gibbs energy of a phase that is essential for an accurate calculation of phase equilibria. We have explored differences in Gibbs energy for the different parameterization and assessments of Stixrude and Lithgow-Bertelloni (2011) and Holland et al. (2013) in the supporting information (section S3.1).

#### 4.2. Configurational and Excess Mixing Properties

As an example for the computation of mixing properties in solid solutions and some of the associated choices, we consider two binaries in the clinopyroxenes phase (Figures 5 and S5) to demonstrate the principles, and compare results of MMA-EoS to those of HeFESTo (Stixrude & Lithgow-Bertelloni, 2011).



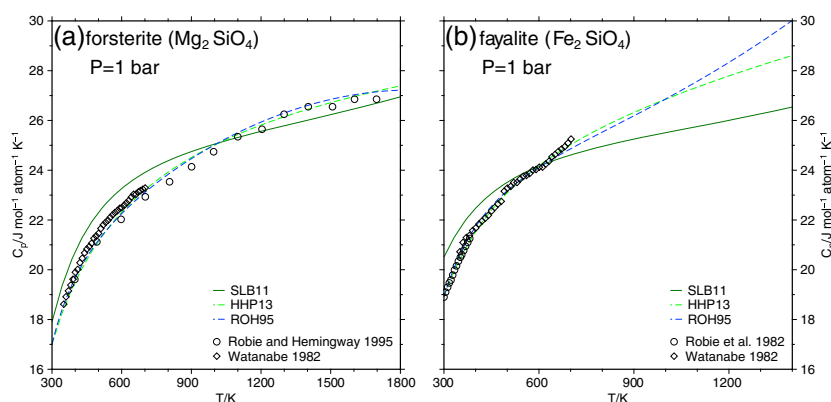


**Figure 4.** Heat capacity per mole of atoms for (a) forsterite and (b) fayalite at ambient  $P$  as functions of  $T$ , computed with MMA-EoS using the model parameters from Stixrude and Lithgow-Bertelloni (2011) (green solid lines) and Holland et al. (2013) (green dashed lines). The polynomial heat capacity approximations by Robie and Hemingway (1995) are included for comparison (blue dashed lines). Experimental data by Robie and Hemingway (1995) (black circles) and Watanabe (1982) (black diamonds) for forsterite and by Robie et al. (1982) (black circles) and Watanabe (1982) (black diamonds) for fayalite are included. The  $T$  scale differs for Figures 4a and 4b.

The pyroxene structure contains three mixing sites (multiplicity per six-oxygen formula unit in parenthesis): an octahedral M2 sites (one), a larger M1 site that can be sixfold or eightfold coordinated (one), and the tetrahedral (T) site (two), respectively (Putnis, 1992). For the clinoenstatite-diopside ( $\text{Mg}_2\text{Si}_2\text{O}_6\text{-CaMgSi}_2\text{O}_6$ ) solid solution, Ca and Mg mix on the M2 site, with ordered end-member structures and a maximum in configurational entropy at  $x = 0.5$  (Figure 5a). The formulation of configurational properties becomes nonunique when partial ordering and mixing on one or more crystallochemical sites are possible, as for the diopside-Ca-tschermak ( $\text{CaAl}_2\text{SiO}_6$ ) binary. Different choices for ordering of Al and Si in the tetrahedra of the Ca-tschermak end-member can lead to a significant contribution to configurational entropy, with complete disorder contributing  $S_{\text{cats}} = 1.15 \text{ J K}^{-1} \text{ mol}^{-1} \text{ atom}^{-1}$ , or its complete absence (for ordered Si and Al on the T site). For random mixing on the M1 site between Mg and Al along the binary, the resulting entropy curve is consistent within error with the calorimetry measurements of Cohen (1986) (Figure 5b). Possible mixing models, their notation and results for the diopside-Ca-tschermak binary are discussed in greater detail in the supporting information (section S3.2).

Excess mixing of solution phases is described by binary interaction terms,  $W_{ij}$  in equation (S74) and can acquire compositional asymmetry through the size parameters for individual end-members  $d_i$  in equation (S75). For the symmetrically formulated clinoenstatite-diopside solution with  $W_{\text{cen,di}} = 2.47 \text{ kJ mol}^{-1} \text{ atom}^{-1}$  in the database of Stixrude and Lithgow-Bertelloni (2011) the experimental data of Newton et al. (1979) are poorly reproduced; however, larger symmetric interaction energy,  $W_{\text{cen,di}} = 5.15 \text{ kJ mol}^{-1} \text{ atom}^{-1}$ , based on an average of asymmetric interaction energies of Fei et al. (1986) provides a significantly improved fit to the experimental data with  $H_{\text{ex}} \approx 1.3 \text{ kJ mol}^{-1} \text{ atom}^{-1}$  (Figure 5c). This excess enthalpy is comparable in magnitude to the configurational Gibbs energy ( $-TS_{\text{cf}}$ ) of  $\sim 1.0 \text{ kJ mol}^{-1} \text{ atom}^{-1}$  (at 1700 K). The experimental data for the diopside-Ca-tschermak solid solution show significantly greater asymmetry (Benisek et al., 2007), and this feature has been fit with different size parameters for the end-members (with a size ratio  $d_{\text{cats}}/d_{\text{di}} = 3.5$ ) in the model by Stixrude and Lithgow-Bertelloni (2011) (Figure 5d). In this case, symmetric models are inadequate to describe the excess mixing properties.

### 4.3. Phase Diagrams

#### 4.3.1. Phase Equilibria Involving Stoichiometric Phases

Thermodynamic models for pure stoichiometric phases can be used directly to compute phase diagrams for a given bulk composition, and the results critically depend on the choice of phases assessed in a database as well as the thermodynamic parameters. The phase diagrams presented here and all further phase diagrams use fixed grid steps for their free variables ( $P$ ,  $T$ , or  $x$ ).

Pressure-temperature phase diagrams for the  $\text{MgSiO}_3$  composition computed with the models of Stixrude and Lithgow-Bertelloni (2011) and Holland et al. (2013) are largely compatible with experimental data (Figure 6) and previous thermodynamic assessments (Gasparik, 2003). Each thermodynamic model and its

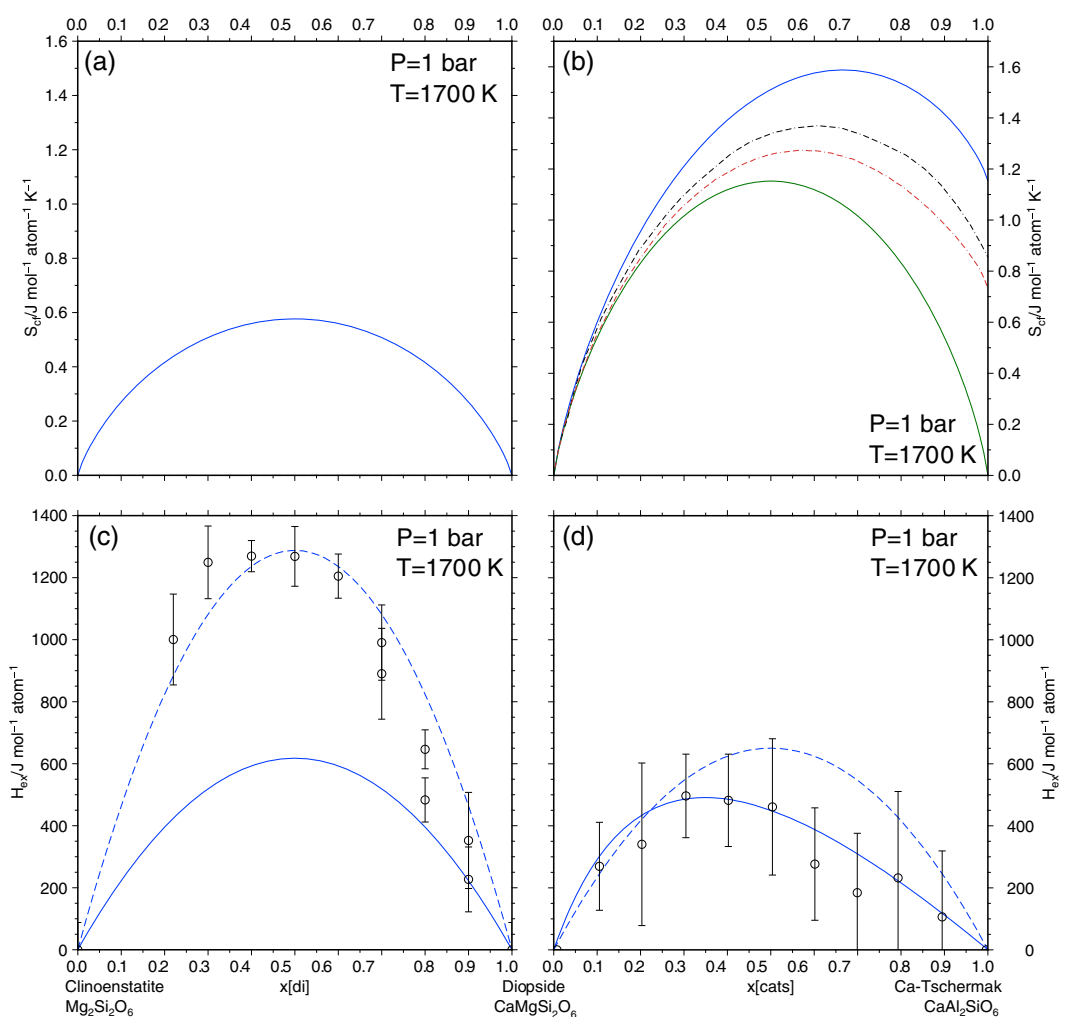


**Figure 5.** (a and b) Entropy of solution and (c and d) excess enthalpy for the clinoenstatite-diopside (Figures 5a and 5c) and diopside-Ca-tschermak (Figures 5b and 5d) solid solutions. In Figure 5a, the solid blue line represents configurational entropy; in Figure 5b the solid lines represent mixing entropies for ionic models with three effective mixing sites, with (blue) and without (green) disorder of Al and Si on the tetrahedral site of Ca-tschermak. These and additional structure models of this diopside-Ca-tschermak binary are discussed in greater detail in section S3.2 and Figure S5. The two dash-dotted curves represent configurational entropy models by Vinograd (2001) (brown) and Cohen (1986) (black). In Figure 5c the solid blue line shows the computed values for excess enthalpy using model parameters from Stixrude and Lithgow-Bertelloni (2011) with an interaction parameter  $W_{\text{en,di}} = 2.47 \text{ kJ mol}^{-1} \text{ atom}^{-1}$ , the dashed blue line represents a modified parameter set with  $W_{\text{en,di}} = 5.15 \text{ kJ mol}^{-1} \text{ atom}^{-1}$ , following Fei et al. (1986). Circles and error bars show experimental data by Newton et al. (1979). In Figure 5d the solid blue line represents computed values using the model parameters from Stixrude and Lithgow-Bertelloni (2011) with size parameters  $d_{\text{di}} = 1$ ,  $d_{\text{cats}} = 3.5$ , which results in the maximum of  $H_{\text{ex}}$  at  $x_{\text{cats}} \approx 0.28$ ; the dashed blue line shows computed values for a symmetric parameter set with  $d_{\text{di}} = d_{\text{cats}} = 1$ , with the maximum  $H_{\text{ex}}$  at  $x_{\text{cats}} = 0.5$ . Circles and error bars show experimental data by Benisek et al. (2007).

parameter set yields discrepancies in a different  $P$ - $T$  range, but no systematic differences or issues in phase diagram topology are apparent. As such, both thermodynamic formulations (Holland et al., 2013; Stixrude & Lithgow-Bertelloni, 2011) seem equally appropriate for computing phase diagrams. Differences stem primarily from the thermodynamic assessment of individual phases.

The model of Stixrude and Lithgow-Bertelloni (2011) fails to produce the clinoenstatite stability field at  $P < 7 \text{ GPa}$  and  $T < 1000 \text{ K}$  (Figure 6), although the phase is present in the database (Table S1); the model of Holland et al. (2013), by contrast, reproduces the clinoenstatite stability field in the assessment by Gasparik (2003) well (Figure 6). At higher pressures, the models differ significantly in the extent of the akimotoite stability field. Akimotoite is virtually absent in the model by Holland et al. (2013), the model by Stixrude and

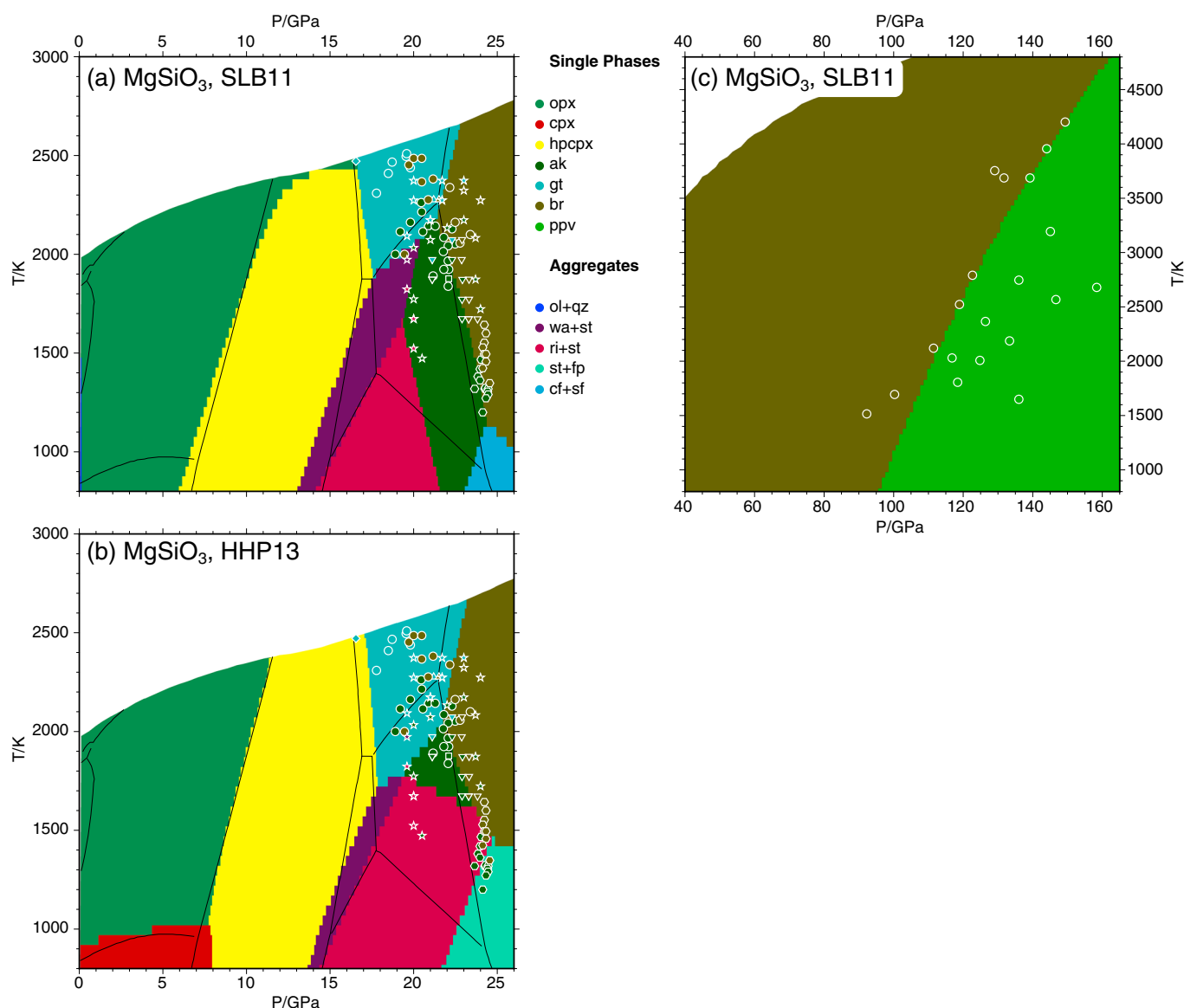


**Figure 6.** Stable phase assemblages with bulk composition  $\text{MgSiO}_3$  at high  $P$  and  $T$ , predicted by MMA-EoS using the Birch-Murnaghan-Mie-Grüneisen-Debye model with (a, c) the database of Stixrude and Lithgow-Bertelloni (2011) and (b) the Caloric-Modified-Tait model with parameters from Holland et al. (2013). Results are computed with 0.1 GPa and 50 K grid spacing. Phase assemblages are color coded according to the legend (for abbreviations, see Table S1). Symbols show experimental data from several sources for stable phases using the corresponding color: in Figures 6a and 6b by Presnall et al. (1998) (diamonds), Chudinovskikh and Boehler (2001) (circles), Hirose et al. (2001) (triangles), Ono et al. (2001) (hexagons), Fei et al. (2004) (squares), Ishii et al. (2011) (inverted triangles), and Sawamoto (1987) (stars); in Figure 6c by Tateno et al. (2009) (circles). Solid lines are phase boundaries reported in Gasparik (2003).

Lithgow-Bertelloni (2011) reproduces experimental data (Ishii et al., 2011; Sawamoto, 1987) reasonably well, and the thermodynamic assessment of Gasparik (2003) appears to overestimate experimental constraints on akimotoite stability (Figure 6).

Prediction of phase equilibria to pressures of Earth's lower mantle is possible with the model of Stixrude and Lithgow-Bertelloni (2011) only, as Holland et al. (2013) have assessed their model for  $P < 34$  GPa. At  $P > 95$  GPa, the model of Stixrude and Lithgow-Bertelloni (2011) predicts the bridgmanite-post-perovskite transition (Figure 6), in good agreement with experimental results (e.g., Tateno et al., 2009).

#### 4.3.2. Phase Equilibria Involving Solid Solutions

As we have shown in section 4.2, thermodynamic properties of solid solutions are defined by independent and additive contributions from end-member (mechanical), ideal (configurational), and nonideal (excess) properties that contribute to Gibbs energy and therefore phase stability. We illustrate this with two binary

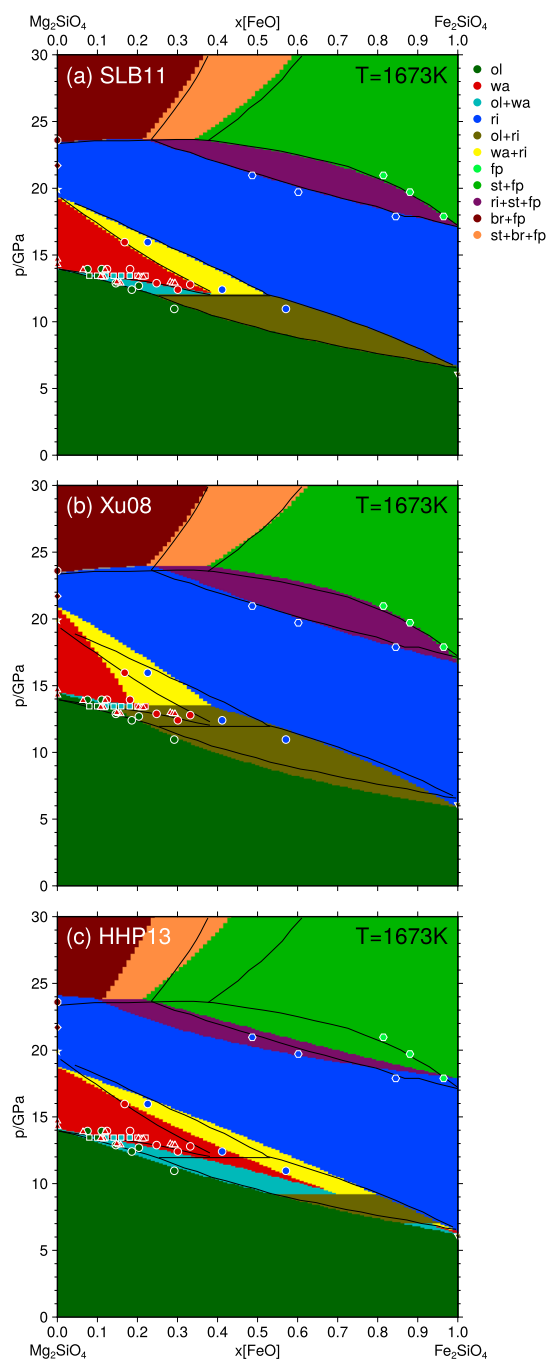


**Figure 7.** Stable phase assemblages along the compositional join  $\text{Mg}_2\text{SiO}_4$ - $\text{Fe}_2\text{SiO}_4$  at  $T = 1673$  K computed using MMA-EoS in comparison to experimental data of stable phases. Results are computed with 0.1 GPa and 1 mol % grid spacing. (a) The thermodynamic model parameters from Stixrude and Lithgow-Bertelloni (2011) are used, (b) computed using parameters from Xu et al. (2008), both with the Birch-Murnaghan-Mie-Grüneisen-Debye model. (c) Computed with the Caloric-Modified-Tait model using parameters from Holland et al. (2013). In all panels, the phase stability fields are color coded according to the legend (for abbreviations, see Table S1), and solid lines show calculated phase boundaries reported in Stixrude and Lithgow-Bertelloni (2011). The symbols show experimental data of stable phases using the same color, taken from Matsuzaka et al. (2000) (hexagons), Frost (2003b) (circles), and Fei and Bertka (1999) (squares). Triangles show experimentally determined points at the boundary of the olivine and wadsleyite coexistence region from Fei and Bertka (1999). Experimental transition pressures for  $\text{Mg}_2\text{SiO}_4$  are from Morishima et al. (1994) (14.3 GPa) and Katsura et al. (2004) (14.6 GPa) (triangles up) for the olivine-wadsleyite transition, from Katsura and Ito (1989), Suzuki et al. (2000) (19.9 GPa, star) for wadsleyite-ringwoodite, and for ringwoodite breakdown from Irifune et al. (1998) (21.7 GPa, diamond) and Ito and Takahashi (1989) (23.6 GPa, octagon). For  $\text{Fe}_2\text{SiO}_4$ , the fayalite-ahrsenite transition is experimentally observed at 6.1 GPa (Yagi et al., 1987) (triangle down).

phase diagrams as a function of  $P$  (at constant  $T$ ) that address different aspects of solutions: (i)  $\text{Mg}_2\text{SiO}_4\text{-Fe}_2\text{SiO}_4$ , where we compare to the results of Stixrude and Lithgow-Bertelloni (2011) and explore differences between various thermodynamic models and parameter sets (Figure 7); (ii)  $\text{Mg}_2\text{Si}_2\text{O}_6\text{-CaMgSi}_2\text{O}_6$  for which (Stixrude & Lithgow-Bertelloni, 2011) also present results (Figure S6). This binary requires the use of complex reciprocal solution models.

For the  $\text{Mg}_2\text{SiO}_4\text{-Fe}_2\text{SiO}_4$  phase diagram we employ end-member thermodynamic properties from the models of Stixrude and Lithgow-Bertelloni (2011), Xu et al. (2008), and Holland et al. (2013), combined with the mixing properties of olivine, wadsleyite, ringwoodite, ferropericlasite, and bridgmanite (Mg- and Fe-bridgmanite). All phase diagrams are qualitatively similar (Figure 7) and reproduce the sequence of olivine, wadsleyite, and ringwoodite solid solutions with increasing  $P$ , followed by a breakdown of  $(\text{Mg,Fe})_2\text{SiO}_4$  to bridgmanite and ferropericlasite at  $x_{\text{Fe}} < 0.6$ .

For the  $\text{Mg}_2\text{SiO}_4$  polymorphic transitions, the experimentally observed transition sequence and pressures are well reproduced by all models (Figure 7), but the ringwoodite breakdown is predicted to occur at significantly larger  $P$  with the model and parameters by Holland et al. (2013) (24.2 GPa) in comparison to 21.7–23.6 GPa from experiments (Fei et al., 2004; Irifune et al., 1998; Ito & Takahashi, 1989; Katsura et al., 2003). Both parameterizations of the Birch-Murnaghan–Mie–Grüneisen–Debye model (Stixrude & Lithgow-Bertelloni, 2011; Xu et al., 2008) yield better results in that respect.

For  $\text{Fe}_2\text{SiO}_4$ , significant differences exist for the high- $P$  transitions between the different models. Experimentally, fayalite transforms to ahrensite (Fe-ringwoodite), followed by a dissociation reaction to stishovite and wüstite (Katsura et al., 2003; Yagi et al., 1987). These transitions are correctly predicted by the models of Xu et al. (2008) and Stixrude and Lithgow-Bertelloni (2011) within 0.5 GPa from experimental values (Figure 7). By contrast, the assessment of Holland et al. (2013) predicts a narrow stability range of Fe-wadsleyite (6.2–6.3 GPa). In contrast to the database by Holland et al. (2013), Fe-wadsleyite is considered too unstable with the parameters of Xu et al. (2008), with the metastable fayalite–Fe-wadsleyite transition predicted at 12.2 GPa, in contrast to 6.6 GPa for the database of Stixrude and Lithgow-Bertelloni (2011) or 8.3 GPa in the assessment by Gasparik (2003).

As the invariant end-member transitions expand into divariant fields of two-phase coexistence, significant differences between model results of the Birch-Murnaghan–Mie–Grüneisen–Debye parameterizations (Stixrude & Lithgow-Bertelloni, 2011; Xu et al., 2008) and Holland et al. (2013) arise due to the assessment of Fe-wadsleyite. Values for Fe-wadsleyite are directly responsible for the prediction of small coexistence regions of olivine and wadsleyite as well as wadsleyite and ringwoodite at the Fe-rich side of the phase diagram in the model of Holland et al. (2013), and a contraction of the olivine and ringwoodite coexistence region at  $x_{\text{Fe}} = 0.55\text{--}0.95$  (Figure 7). Experimentally, this coexistence region is much broader, starting from  $x_{\text{Fe}} > 0.12$  or 0.20 at the expense of wadsleyite-bearing assemblages (e.g., Katsura & Ito, 1989).

At higher  $P$ , the stability field of stishovite appears to be overestimated by all models, but most significantly by the Holland et al. (2013) data set, shifting the bridgmanite stability to lower  $x_{\text{Fe}}$  and substantially decreasing the stability range of the assemblage ringwoodite, stishovite, and ferropericlasite (Figure 7), below the experimentally observed  $x_{\text{Fe}}$  values (Ito & Takahashi, 1989).

Major differences between the two assessments of the Birch-Murnaghan–Mie–Grüneisen–Debye models (Stixrude & Lithgow-Bertelloni, 2011; Xu et al., 2008) are observed in a decrease of the olivine and ringwoodite stability field, with  $x_{\text{Fe}}$  shifting from 0.15 (Xu et al., 2008) to 0.30 (Stixrude & Lithgow-Bertelloni, 2011) between the two databases. Similar to the problems of the database by Holland et al. (2013) to reproduce the olivine and ringwoodite stability field in the phase diagram, the large extent of this coexistence region in the assessment by Xu et al. (2008) can be traced to the Fe-wadsleyite parameterization.

#### 4.4. Elastic Properties

Density and elastic moduli are among the most important physical properties for applications in geodynamics and seismology. For pure phases, including end-members of the solid solutions, analytical expressions are used in MMA-EoS, similar to other studies (Cottaar et al., 2014), and for solid solutions and polyphase aggregates we use volume-weighted mixing rules (sections S1.6 and S1.7 in the supporting information).

We illustrate the utility of MMA-EoS to compute the elastic properties for the stable assemblage with  $\text{MgSiO}_3$  composition as a function of  $P$  at room  $T$  (Figure 8), where we also compare to a large number of experimental data. When the system is predicted to consist of a single phase, that is, enstatite at  $P < 11$  GPa and bridgmanite

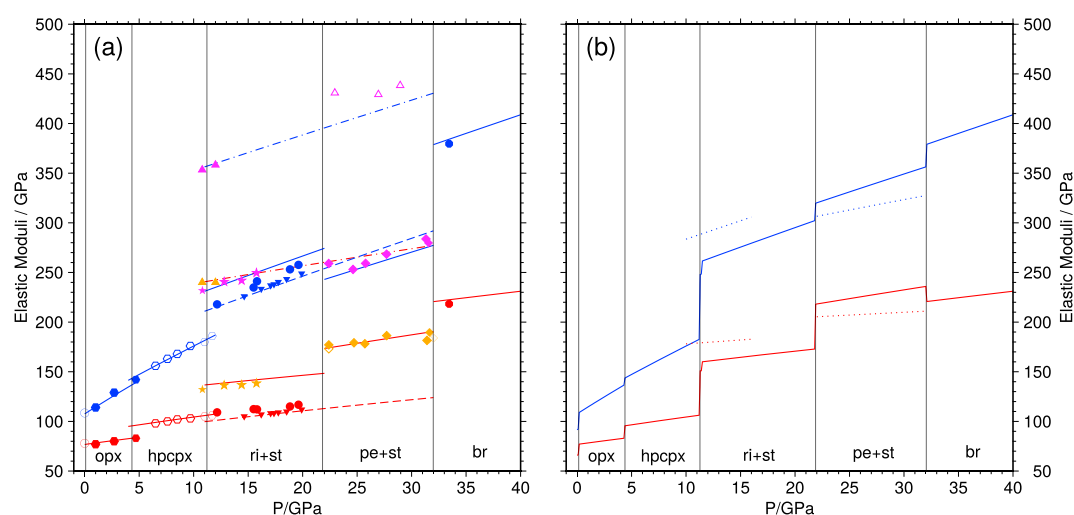


**Figure 8.** (a) Bulk (blue) and shear moduli (red) of single phases and (b) the stable assemblage with  $\text{MgSiO}_3$  bulk composition at room  $T$ , computed with the MMA-EoS software using the model parameters from Stixrude and Lithgow-Bertelloni (2011). Annotations at the bottom indicate the stable phase assemblages in the pressure ranges delimited by vertical lines (Figure 6; for abbreviations see Table S1). In Figure 8a lines show computed single-phase properties. Between 11 GPa and 22 GPa, the solid lines show computed elastic moduli of ringwoodite, between 22 GPa and 32 GPa they show the properties of periclase; between 11 GPa and 22 GPa the dash-dotted lines show the moduli of stishovite and the dashed lines those of Mg majorite. Symbols show experimental data for orthoenstatite by Kung et al. (2004) (filled hexagons) and by Jackson et al. (2007) (empty circles), for high-pressure clinoenstatite by Kung et al. (2004) (empty hexagons), for ringwoodite by Sinogeikin et al. (2003) (filled stars), for periclase by Zha et al. (2000) (filled diamonds) and by Murakami et al. (2009) (empty diamonds), for stishovite by Shieh and Duffy (2002) (empty triangles) and by Jiang et al. (2009) (filled triangles), for bridgmanite by Murakami et al. (2007) (filled octagons), for Mg-majorite by Pamato et al. (2016) (filled circles) and for  $\text{mj}_{80}\text{py}_{20}$  by Liu et al. (2015) (inverted triangles). Data points for single phases that do not represent the entire stable assemblage are colored in magenta (bulk moduli) and orange (shear moduli). In Figure 8b the solid lines show the computed properties of the stable phase assemblages; the dotted lines show Voigt-Reuss-Hill averages of interpolated experimental moduli for the computed stable phase assemblages.

at  $P > 32$  GPa, the model results agree well with experimental data (Jackson et al., 2007; Kung et al., 2004; Murakami et al., 2007). In the intermediate pressure range, two phases are predicted to coexist: stishovite and ringwoodite at  $P = 11$ –22 GPa (cf. Jiang et al., 2009; Shieh & Duffy, 2002; Sinogeikin et al., 2003), and stishovite and periclase at  $P = 22$ –32 GPa (cf. Murakami et al., 2009; Zha et al., 2000). Voigt-Reuss-Hill averages of experimental elastic moduli agree well with predictions from the thermodynamic model by Stixrude and Lithgow-Bertelloni (2011).

The assemblages stable at room temperature do not contain garnet, because the majorite end-member in the system  $\text{MgSiO}_3$  only becomes stable at higher temperatures (Figure 6). Nevertheless, garnets play a critical role in the upper mantle and the transition zone of the mantle, and majorite data and results are included in Figure 8. For majorite, the predictions based on the model of Stixrude and Lithgow-Bertelloni (2011) agree well with experimental data by Liu et al. (2015) and Pamato et al. (2016). In section S3.4 and Figure S7 of the supporting information we further explore density and elastic properties (shear and bulk modulus) in three binary garnet solid solutions (pyrope-almandine, pyrope-grossular, and pyrope-majorite) that play a central role through most of the upper mantle and the transition zone (e.g., Ishii et al., 2011; Ita & Stixrude, 1992). For these systems extensive data sets have been measured after the assessment of the database by Stixrude and Lithgow-Bertelloni (2011), a fact that allows to test the predictions from their model.

## 5. Phase Equilibria in the Mantle

### 5.1. Pyrolite

#### 5.1.1. Mineral Assemblages

As a composition model, pyrolite (McDonough & Sun, 1995; Workman & Hart, 2005) has successfully been used to describe the state, rheology, and dynamics of the upper mantle and transition zone (e.g., Akaogi, 2007; Frost, 2008; Schuberth et al., 2009b; Weidner, 1985), while its applicability to the lower mantle remains



**Table 2**  
Chemical Bulk Compositions Used in the Computation of Phase Assemblages

Component	BOC (mol %)	DM (mol %)	NCMAS (mol %)	CFMAS (mol %)	CFMS (mol %)	FMAS (mol %)	FMS (mol %)	MS (mol %)
MgO	15.11	56.17	49.85	49.91	50.85	52.52	53.52	60.14
FeO	6.59	5.71	6.17	6.18	6.29	6.51	6.62	—
CaO	14.39	0.99	2.94	2.94	3.00	—	—	—
Al <sub>2</sub> O <sub>3</sub>	10.39	0.59	2.22	2.22	—	2.22	—	—
Na <sub>2</sub> O	1.76	0.00	0.11	—	—	—	—	—
SiO <sub>2</sub>	51.76	36.54	38.71	38.75	39.86	38.75	39.86	39.86

*Note.* Different lithologies are for the differentiated slab, dry bulk oceanic crust (BOC), and dry harzburgite for the depleted mantle (DM) (Chemia et al., 2015). For the primitive mantle, pyrolite from Workman and Hart (2005), is reduced to a five-component system (NCMAS). For further reduced compositions, Na<sub>2</sub>O is removed and the composition renormalized (CFMAS). For the FMAS composition, the CaO component is distributed to the other divalent oxides MgO and FeO, maintaining their ratio. For the other four component system CFMS, trivalent Al<sub>2</sub>O<sub>3</sub> is replaced by an equal amount of SiO<sub>2</sub> and the divalent oxides MgO, FeO, and CaO, again maintaining the ratios among the latter. For the FMS system, the CaO component of CFMS is distributed between MgO and FeO such that their ratio remains the same. For the MS system, FeO is completely replaced by MgO.

a subject of debate (e.g., Kurnosov et al., 2017; Murakami et al., 2012; Ricolleau et al., 2009; Wang et al., 2015). For geophysical considerations, pyrolite has typically been reduced to, at most, a six-component system Na<sub>2</sub>O-CaO-FeO-MgO-Al<sub>2</sub>O<sub>3</sub>-SiO<sub>2</sub> (Table 2), comprising ~99 mol % of its chemical composition. While Cr<sub>2</sub>O<sub>3</sub> is more abundant than Na<sub>2</sub>O in the pyrolite models, the inclusion of a monovalent—rather than another trivalent—cation to the composition is important in terms of the resulting mineralogy.

Using the thermodynamic database of Stixrude and Lithgow-Bertelloni (2011), we explore the sensitivity of phase relations to chemical composition by sequentially increasing the number of components in the pyrolite model from the binary MgO-SiO<sub>2</sub> (MS) to the six-component Na<sub>2</sub>O-CaO-FeO-MgO-Al<sub>2</sub>O<sub>3</sub>-SiO<sub>2</sub> (NCMAS) system (Table 2). When adding chemical components, (i) new phases and their stability fields occur, (ii) new end-members are introduced and form mineral solutions whose stability fields generally expand, and/or (iii) the variance of mineral assemblages increases, resulting in binary or higher-order phase loops which allow for the coexistence of phases previously separated by sharp boundaries.

We evaluate phase assemblages, phase proportions (Figure 9), and chemical composition along isentropes with a potential temperature of 1600 K as a proxy for the mantle geotherm and present complete phase diagrams for the MS, FMAS, and NCMAS systems (Figures 10–12, and S9–S11 for the systems FMS, CFMS, and CFMAS). Where isentropes pass through grid cells on either side of a phase boundary, the composition curves can occasionally exhibit oscillations (e.g., Figure 9, around 18 GPa).

For the Mg<sub>2</sub>SiO<sub>4</sub> component in the MS system, the model of Stixrude and Lithgow-Bertelloni (2011) predicts phase transitions from olivine to wadsleyite and from wadsleyite to ringwoodite with positive Clapeyron slopes (Figures 9 and 10). Ringwoodite breaks down to a lower-mantle phase assemblage of bridgmanite and periclase with a negative Clapeyron slope. The predictions for phase transition locations and Clapeyron slopes are in good quantitative agreement with experiments (Akaogi, 2007; Inoue et al., 2006; Ishii et al., 2011; Katsura et al., 2004; Morishima et al., 1994; Suzuki et al., 2000). For the pyroxene-based, MgSiO<sub>3</sub> assemblages, the phase diagram shown in Figure 6 implies that, along the isentrope, orthoenstatite transforms to high-pressure clinoenstatite (Figure 10). After intersecting the majorite stability field (Figure 6), high-pressure clinopyroxene dissociates to wadsleyite and stishovite, and these subsequently recombine to form akimotoite. The transition of akimotoite to bridgmanite is lower by ~1 GPa than the ringwoodite formation (Figure 9). At higher *T*, majorite garnet transforms to bridgmanite directly with a positive Clapeyron slope, as also determined in experiments (e.g., Ishii et al., 2011). At lowermost mantle pressures, bridgmanite is replaced by post-perovskite with a steep positive Clapeyron slope as already shown in Figure 6.

With a molar ratio Fe/(Fe+Mg) = 0.11 in pyrolite and the reduced compositions (Table 2), for the FMS system the binary phase field between olivine and wadsleyite is predicted to be narrow along the isentrope, and the phase transition shifts to slightly lower pressure than in the MS system (Figures 7 and 9). By contrast, the coexistence region between wadsleyite and ringwoodite is in the range of ~1 GPa, with an overall reduction

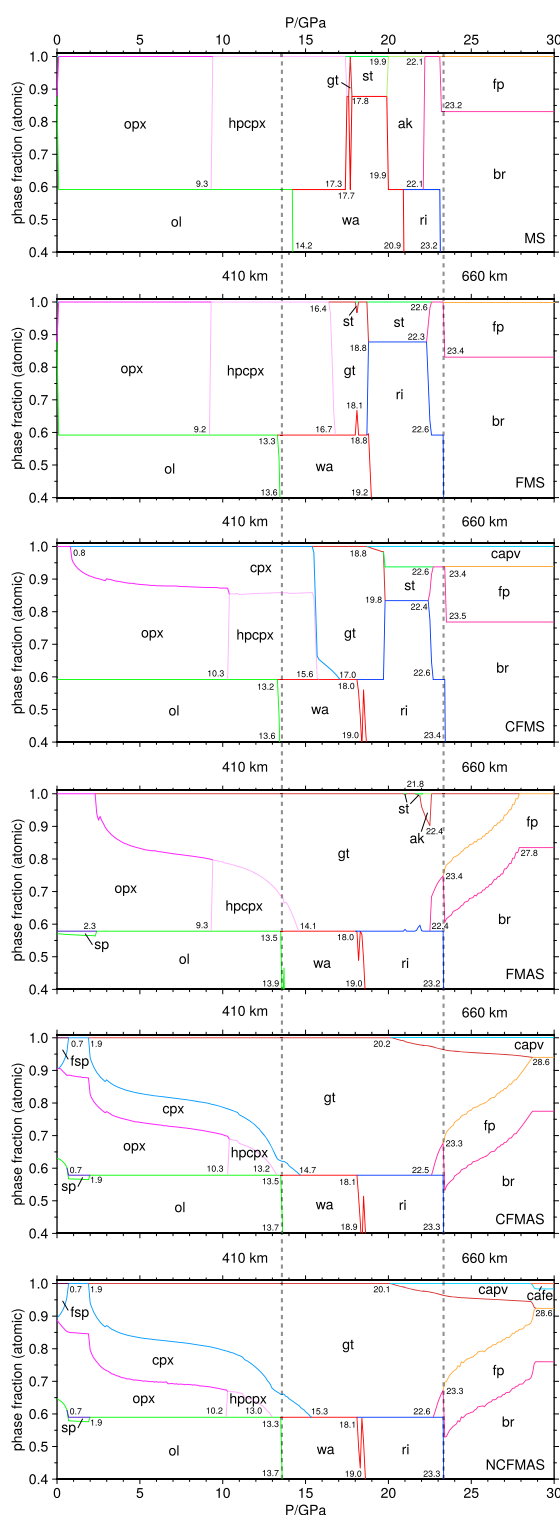


**Figure 9.** Phase fractions for the reduced pyrolite compositions (Table 2) (top to bottom) for MS, FMS, CFMS, FMAS, CFMAS, and NCFMAS systems along 1600 K isentropes, computed with the thermodynamic database of Stixrude and Lithgow-Bertelloni (2011). Stable phases are indicated with the abbreviations of Table S1. The phase fraction fields start at 0.4, with the remaining portion occupied by the phase at the bottom of each panel. Numbers in the panels indicate phase transition pressures (GPa). For divariant and multivariant phase transitions, the onset and completion of a phase transition is indicated. Numbers at the bottom of each panel indicate the completion of the phase transition, representing phase fraction 0.0 (rather than 0.4 as the location suggests). Pressures of the 410 km and 660 km discontinuities are indicated by vertical dashed lines.

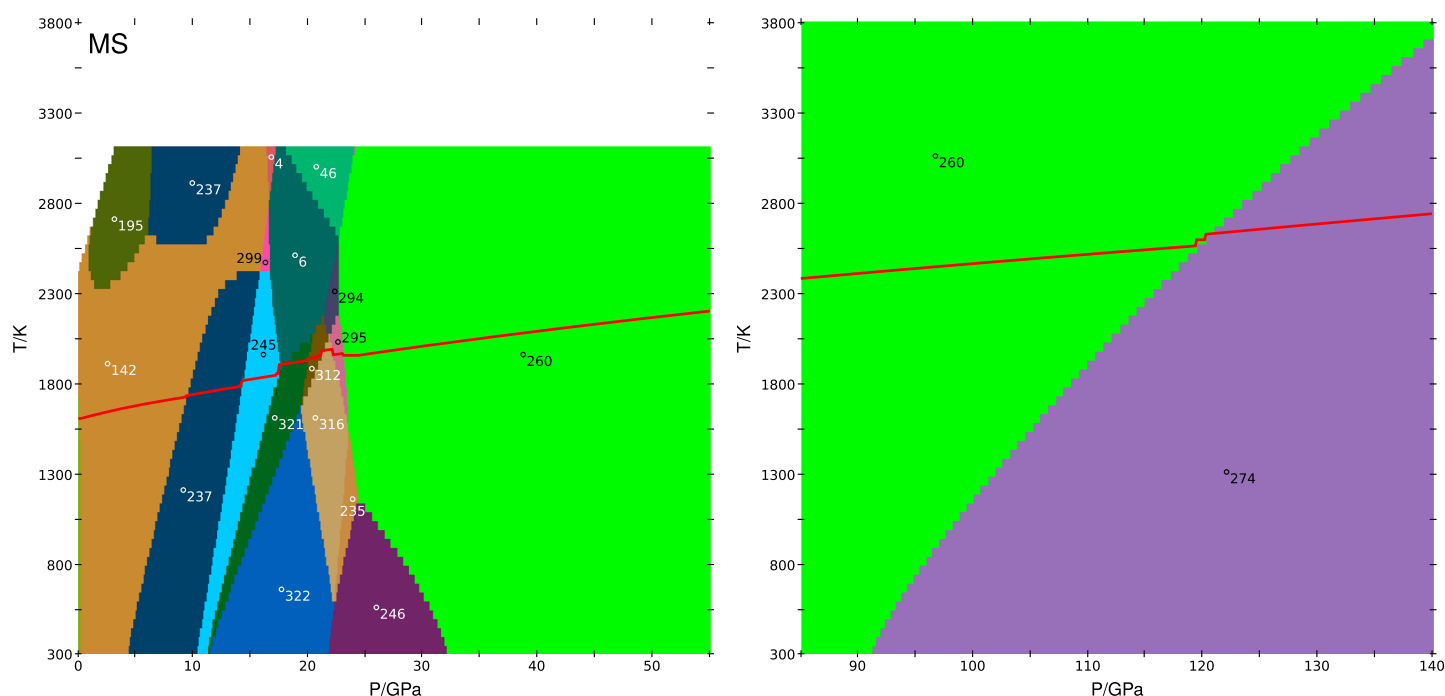


**Figure 10.** Phase diagrams computed with MMA-EoS using the model parameters from Stixrude and Lithgow-Bertelloni (2011) for MS composition (Table 2) as a function of  $P$  and  $T$  with 0.1 GPa and 50 K grid spacing. (left) The  $P$  range 0–55 GPa (surface to lower mantle), (right) the  $P$  range 85–140 GPa (lowermost mantle). An isentrope computed with predicted material properties, starting with 1600 K at 0 GPa, is shown on top of the phase diagrams as a red line. Numbered stability fields (Table S2; for abbreviations, see Table S1) contain the following phase assemblages for the low- $P$  region (Figure 10, left): (142) ol+opx, (237) ol+hpcpx, (245) wa+hpcpx, (321) wa+st, (322) ri+st, (316) ri+ak, (235) ak+fp, (246) st+fp, (260) br+fp, (195) ol+cpx, (4) ol+gt, (299) wa+opx, (6) wa+gt, (46) gt+fp, (312) wa+ak, (294) wa+br, and (295) ri+br. Critical phase transitions for  $\text{Mg}_2\text{SiO}_4$  along the isentrope are ol  $\rightarrow$  wa (237  $\rightarrow$  245 at 14.3 GPa and 1710 K), wa  $\rightarrow$  ri (312  $\rightarrow$  316; 21.2 GPa, 1950 K), and the breakdown ri  $\rightarrow$  br+pc (295  $\rightarrow$  260; 23.2 GPa, 1940 K). In the  $\text{MgSiO}_3$ -based system the following transitions occur along the isentrope: opx  $\rightarrow$  hpcpx (142  $\rightarrow$  237; 9.4 GPa, 1720 K), a dissociation hpcpx  $\rightarrow$  wa+st (245  $\rightarrow$  321; 17.6 GPa, 1860 K), the recombination wa+st  $\rightarrow$  ak (321  $\rightarrow$  312; 20.0 GPa, 1920 K), and ak  $\rightarrow$  br (316  $\rightarrow$  295; 22.3 GPa, 1980 K). In the high- $P$  region (Figure 10, right) the following phase assemblages occur: (260) br+fp, (274) ppv+fp, with the transition along the mantle isentrope occurring at 120.6 GPa and 2630 K.

of the wadsleyite stability field (Figures 9, 10, and S8). Dissociation of ringwoodite occurs through a narrow coexistence region in which ringwoodite and stishovite recombine to form bridgmanite.

For the  $\text{MgSiO}_3$ -dominated minerals, the orthopyroxene-high-pressure clinopyroxene transition is not affected by the addition of FeO (Figures 9 and S8), but high-pressure clinopyroxene transforms to garnet at lower  $P$ , reflecting a slight increase of the garnet stability field at the expense of akimotoite (Figure 13). In the presence of FeO, garnet breaks down to ringwoodite and stishovite, from which bridgmanite forms directly, without intermediate akimotoite stability; this prediction of the model by Stixrude and Lithgow-Bertelloni (2011) is in disagreement with experiments (Ito & Yamada, 1982; Ohtani et al., 1991) that show a transition from akimotoite to bridgmanite. In the lowermost mantle, the post-perovskite transition is shifted to slightly higher  $P$  in the FMS system and occurs nearly univariantly; only for  $T < 2000$  K (Figure S8) a significant phase coexistence region opens between bridgmanite and post-perovskite. In the assessment of Stixrude and Lithgow-Bertelloni (2011), the Clapeyron slope of the transition does not change relative to the MS system, although experiments suggest only half the value (Catalli et al., 2009).

In the four-component system CFMS, with CaO added, clinopyroxene, with end-members diopside and hedenbergite (Table S1), occurs as a new phase in the assemblage (Figures 9 and S9). Clinopyroxene coexists with orthopyroxene, high-pressure clinopyroxene, and garnet up to pressures of the transition zone. The incorporation of the Ca-bearing constituents in clinopyroxene significantly reduces the orthopyroxene and high-pressure clinopyroxene stability at low and high pressures, respectively, relative to the FMS system (Figure 9). In the thermodynamic database of Stixrude and Lithgow-Bertelloni (2011), clinopyroxene has multiple Ca-bearing end-members, while high-pressure clinopyroxene has none (Table S1), favoring stability of the former phase. In the lower part of the transition zone, Ca-perovskite appears and becomes the first lower-mantle phase to exsolve from the garnet solid solution (Figures 9 and S9), as already seen in the

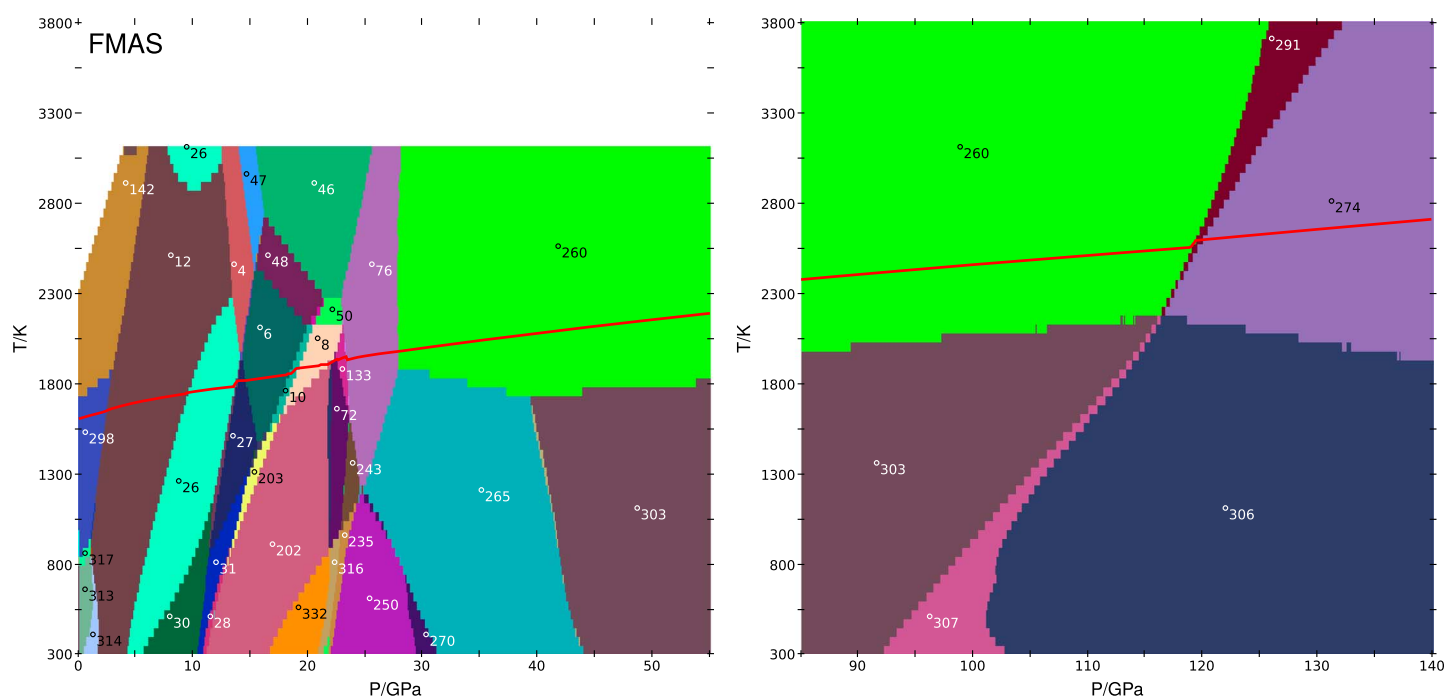


**Figure 11.** Phase diagrams computed with MMA-EoS using the model parameters from Stixrude and Lithgow-Bertelloni (2011) for FMS composition (Table 2) as a function of  $P$  and  $T$  with 0.1 GPa and 50 K grid spacing. (left) The  $P$  range 0–55 GPa (surface to lower mantle), (right) the  $P$  range 85–140 GPa (lowermost mantle). An isentrope computed with predicted material properties, starting with 1,600 K at 0 GPa, is shown on top of the phase diagrams as a red line. Numbered stability fields (Table S2; for abbreviations, see Table S1) contain the following phase assemblages for the low- $P$  region (Figure 11, left): (4) ol+gt, (6) wa+gt, (8) ri+gt, (10) wa+ri+gt, (12) ol+opx+gt, (26) ol+hpcpx+gt, (27) wa+hpcpx+gt, (28) ri+hpcpx+gt, (30) ol+ri+hpcpx+gt, (31) wa+ri+hpcpx+gt, (46) gt+fp, (47) ol+gt+fp, (48) wa+gt+fp, (50) ri+gt+fp, (72) ri+ak+gt, (76) gt+br+fp, (133) ri+gt+br, (142) ol+opx, (202) ri+gt+st, (203) wa+ri+gt+st, (235) ak+fp, (243) ak+gt+fp, (250) ak+st+fp, (260) br+fp, (265) ak+br+fp, (270) ak+st+br+fp, (298) sp+ol+opx, (303) br+fp+cf, (313) ol+opx+ky, (314) ol+opx+gt+ky, (316) ri+ak, (317) ol+opx+ak, and (332) ri+ak+st. Along the isentrope the following transitions occur in the  $\text{Mg}_2\text{SiO}_4$ -based system: ol  $\rightarrow$  wa (26  $\rightarrow$  27 at 13.7 GPa and 1,790 K), wa  $\rightarrow$  ri (6  $\rightarrow$  (10)  $\rightarrow$  8; 18.7 GPa, 1,860 K), ri  $\rightarrow$  br+fp (8  $\rightarrow$  (133)  $\rightarrow$  76 between 21.7 GPa and 23.3 GPa, 1,910 K and 1,940 K). In the  $\text{MgSiO}_3$ -based system the following transitions occur: sp  $\rightarrow$  gt (298  $\rightarrow$  12; 2.6 GPa, 1,640 K), opx  $\rightarrow$  hpcpx (12  $\rightarrow$  26; 9.6 GPa, 1,740 K), hpcpx  $\rightarrow$  gt (27  $\rightarrow$  6; 14.6 GPa, 1,810 K), gt  $\rightarrow$  br+fp (8  $\rightarrow$  (133, 76)  $\rightarrow$  260 between 21.7 GPa and 27.7 GPa, 1,910 K and 1,970 K). In the high- $P$  region (Figure 11, right) the following phase assemblages occur: (260) br+fp, (274) ppv+fp, (291) br+ppv+fp, (303) br+fp+cf, (306) ppv+fp+cf, and (307) br+ppv+fp+cf. The isentrope intersects the br  $\rightarrow$  ppv phase boundary (260  $\rightarrow$  (291)  $\rightarrow$  274) at 119.6 GPa and 2,560 K. Phase fields given in parentheses indicate coexistence regions; in those cases,  $P$  and  $T$  refer to conditions at the boundaries or the center of the intersection between isentrope and coexistence region.

diopside-enstatite phase diagram (Figure S6) and consistent with a decreasing Ca solubility in garnet as a function of  $P$  (Saikia et al., 2008). As there is no Ca-bearing end-member in the bridgmanite and post-perovskite solutions, this transition does not change relative to FMS.

In the other four-component system considered, FMS,  $\text{Al}_2\text{O}_3$  leads to new phases being formed at low  $P$ , but tends to become a substituent in ferromagnesian silicates at higher  $P$ .  $(\text{Mg,Fe})\text{Al}_3\text{O}_4$  spinel occurs as an Al-bearing phase in the mantle assemblage, stable up to 2.5 GPa (Figures 9 and 11), which agrees well with the location of the spinel-lherzolite to garnet-lherzolite transition in the CMAS system (Klemme & O'Neill, 2000; Ziberna et al., 2013). Through the addition of pyrope and almandine end-members (Table S1), the garnet stability range extends dramatically (Figures 9, 11, and 13) at the expense of high-pressure clinopyroxene (low  $P$ ) and ringwoodite and stishovite as well as bridgmanite (high  $P$ ). The fraction of garnet in the phase assemblage increases continuously with  $P$  as the pyroxenes are consumed (Figure 9). Garnet stability extends significantly beyond pressures of the 660 km seismic discontinuity and the ringwoodite breakdown (Figures 9, 11 and 13). In the lowermost mantle, the addition of  $\text{Al}_2\text{O}_3$  stabilizes the postperovskite phase at the expense of bridgmanite (Figure 11), moving the transition to slightly lower pressure. Also, the coexistence region of bridgmanite and post-perovskite widens, both at low and high temperature, but it remains relatively narrow in the  $T$  range of 2,000–2,500 K.

The five-component system CFMS (Figures 9 and S10) shows the combined characteristics of the FMS and CFMS assemblages and their solutions, as well as several new phases. Below 1 GPa, feldspar forms as anorthite (Table S1). With increasing  $P$ , anorthite is predicted to transform to a spinel-bearing assemblage, before

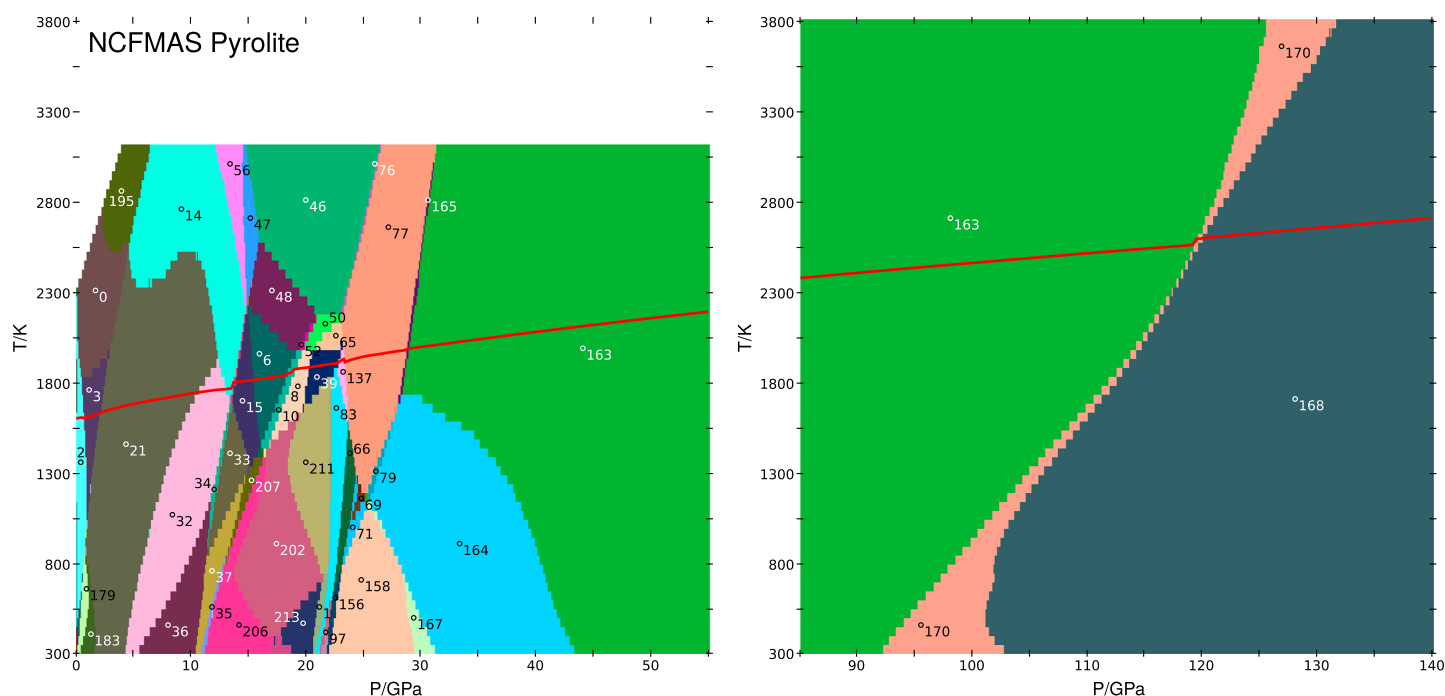


**Figure 12.** Phase diagrams computed with MMA-EoS using the model parameters from Stixrude and Lithgow-Bertelloni (2011) for pyrolite composition (Table 2) as a function of  $P$  and  $T$  with 0.1 GPa and 50 K grid spacing. (left) The  $P$  range 0–55 GPa (surface to lower mantle), (right) the  $P$  range 85–140 GPa (lowermost mantle). An isentrope computed with predicted material properties, starting with 1600 K at 0 GPa, is shown on top of the phase diagrams as a red line. Numbered stability fields (Table S2; for abbreviations, see Table S1) contain the following phase assemblages for the low- $P$  region (Figure 12, left): (0) ol+opx+cpx, (1) ri+capv+ak+gt+st, (2) fsp+ol+opx+cpx, (3) sp+ol+opx+cpx, (6) wa+gt, (8) ri+gt, (10) wa+ri+gt, (14) ol+cpx+gt, (15) wa+cpx+gt, (21) ol+opx+cpx+gt, (32) ol+cpx+hpcpx+gt, (33) wa+cpx+hpcpx+gt, (34) ol+wa+cpx+hpcpx+gt, (35) ri+cpx+hpcpx+gt, (36) ol+ri+cpx+hpcpx+gt, (37) wa+ri+cpx+hpcpx+gt, (39) ri+capv+gt, (46) gt+fp, (47) ol+gt+fp, (48) wa+gt+fp, (50) ri+gt+fp, (52) wa+ri+gt+fp, (56) ol+cpx+gt+fp, (65) ri+capv+gt+fp, (66) capv+ak+gt+fp, (69) capv+gt+st+fp, (71) capv+ak+gt+st+fp, (76) gt+br+fp, (77) capv+gt+br+fp, (79) capv+ak+gt+br+fp, (83) ri+capv+ak+gt, (97) ri+capv+ak+cf, (137) ri+capv+gt+br, (156) capv+ak+fp+cf, (157) ri+capv+ak+fp+cf, (158) capv+ak+st+fp+cf, (163) capv+br+fp+cf, (164) capv+ak+br+fp+cf, (165) capv+gt+br+fp+cf, (167) capv+ak+st+br+fp+cf, (179) ol+opx+cpx+ky, (183) ol+opx+cpx+gt+ky, (195) ol+cpx, (202) ri+gt+st, (203) wa+ri+gt+st, (206) ri+cpx+gt+st, (207) wa+ri+cpx+gt+st, (211) ri+capv+gt+st, (213) ri+ak+gt+st, and (214) ri+cpx+ak+gt+st. Along the isentrope the following transitions occur in the  $\text{Mg}_2\text{SiO}_4$ -based system: ol  $\rightarrow$  wa (14  $\rightarrow$  15 at 13.7 GPa and 1780 K), wa  $\rightarrow$  ri (6  $\rightarrow$  10)  $\rightarrow$  8; 18.7 GPa, 1850 K), ri  $\rightarrow$  br+fp (137  $\rightarrow$  77; 23.3 GPa, 1920 K). In the  $\text{MgSiO}_3$ -based system the following transitions occur: fsp  $\rightarrow$  sp (2  $\rightarrow$  3; 0.9 GPa, 1600 K), sp  $\rightarrow$  gt (3  $\rightarrow$  21; 2.1 GPa, 1630 K), opx+cpx  $\rightarrow$  cpx+hpcpx+gt (3  $\rightarrow$  21)  $\rightarrow$  32 between 2.1 GPa and 10.5 GPa, 1630 K and 1740 K), hpcpx  $\rightarrow$  gt (32  $\rightarrow$  14; 13.0 GPa, 1750 K), cpx  $\rightarrow$  gt (15  $\rightarrow$  6; 15.5 GPa, 1820 K), gt  $\rightarrow$  capv+br+cf (8  $\rightarrow$  (39, 137, 77, 165)  $\rightarrow$  163 between 20.2 GPa and 28.9 GPa, 1880 K and 1990 K) via capv in (8  $\rightarrow$  39; 20.2 GPa, 1880 K), br in (39  $\rightarrow$  137; 22.7 GPa, 1910 K), cafe in (77  $\rightarrow$  165; 28.7 GPa, 1970 K) and gt out (165  $\rightarrow$  163; 28.9 GPa, 1990 K). In the high- $P$  region (Figure 12, right) the following phase assemblages occur: (163) capv+br+fp+cf, (168) capv+ppv+fp+cf, and (170) capv+br+ppv+fp+cf. The isentrope intersects the br  $\rightarrow$  ppv phase boundary (163  $\rightarrow$  (170)  $\rightarrow$  168) at 119.4 GPa and 2570 K. Phase fields given in parentheses indicate coexistence regions; in those cases,  $P$  and  $T$  refer to conditions at the boundaries or the center of the intersection between isentrope and coexistence region.

the transformation to a garnet-bearing assemblage occurs, similar to the CMAS system (Figures 9 and 11). However, the anorthite stability range in CFMAS predicted by the model of Stixrude and Lithgow-Bertelloni (2011) is smaller than that established for pure  $\text{CaAl}_2\text{Si}_2\text{O}_8$  (e.g., Koziol and Newton, 1988) or in tholeiitic basalts (O'Brien & Rötzler, 2003). In addition, in both of these studies, feldspar transforms to a garnet-bearing assemblage directly. The presence of Ca-Al-end-members in both clinopyroxene (Ca-tschermak) and garnet (grossular) (Table S1) does not alter the phase proportions between garnet and any of the pyroxene solid solutions compared to FMAS (Figure 9). Formation of Ca-perovskite in CFMAS initiates at slightly higher pressure than in the CFMS system (Figures 9, S9, and S10), and bridgmanite formation occurs from garnet, in good agreement with experiments on pyrolite (Ishii et al., 2011).

In the full pyrolite composition (NCFMAS, Table 2), the jadeite end-member stabilizes clinopyroxene at the expense of garnet, both in terms of an expansion of the stability field (Figures 9, 12, and 13) and phase proportions (Figure 9). A Ca-ferrite-structured nepheline phase,  $\text{NaAlSi}_4\text{O}_{10}$  (Table S1), hosts  $\text{Na}_2\text{O}$  at lower mantle conditions (Irifune & Ringwood, 1993; Liu, 1977; Miyajima et al., 1999), forming from the jadeitic garnet component (Figures 9 and 12). The lowermost mantle transition between bridgmanite and post-perovskite is largely

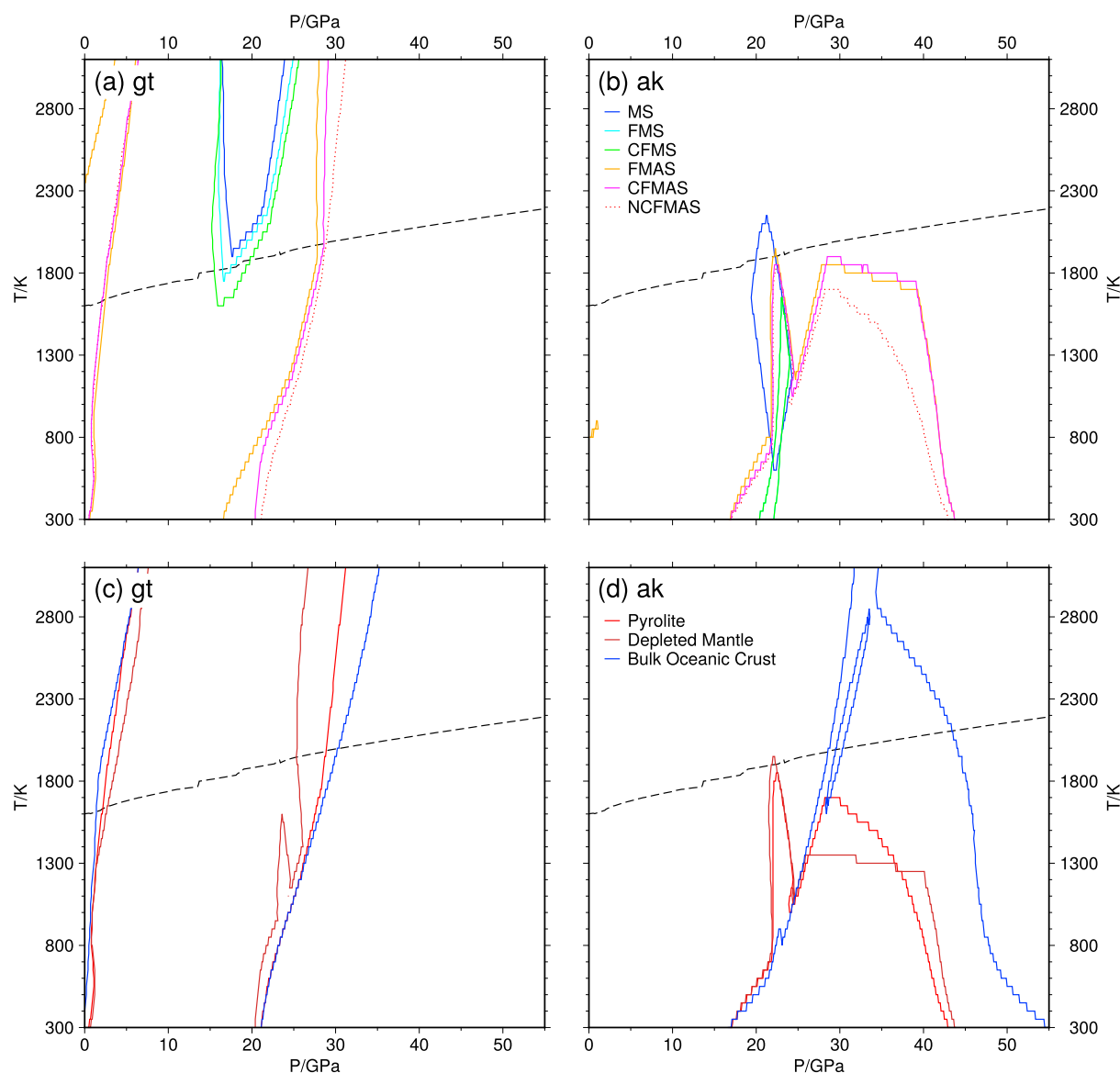


**Figure 13.** Stability fields of (a and c) garnet and (b and d) akimotoite shown by colored contour lines for different compositions: Figures 13a and 13b show results for the reduced pyroilte bulk compositions (Table 2) MS (blue), FMS (cyan), CFMS (green), FMAS (orange), and CFMAS (magenta); results for NCFMAS (pyroilte) are plotted as dotted red lines. Figures 13c and 13d show stability fields for pyroilte (red), depleted mantle (brown), and bulk oceanic crust (blue) (Table 2). The adiabat for NCFMAS (pyroilte) with a potential temperature of 1600 K is displayed as a dashed black line in all panels.

unaffected by the addition of  $\text{Na}_2\text{O}$  when compared to the other  $\text{Al}_2\text{O}_3$ -bearing composition (Figures 11, S10, and 12) and consistent with experiments on KLB-1 peridotite (Murakami & Hirose, 2005; Ono & Oganov, 2005).

### 5.1.2. Element Partitioning

The chemical composition of solution phases is a result of the relative abundance of oxides in the bulk system, the extent of composition space accessible to each species, as well as element partitioning between coexisting phases. These effects are recorded in the variation of mineral compositions as a function of  $x$ ,  $P$ , and  $T$  as a sensitive measure of the accuracy of thermodynamic models and data and can be readily verified against experimental partitioning data. Here we explore element partitioning in pyroilte between the different phases that are stable along the 1600 K isentrope by predicting phase proportions (Figure 9), Mg-Fe budget, and partitioning (Figure 14) as well as  $\text{CaO}$ ,  $\text{Al}_2\text{O}_3$  and  $\text{Na}_2\text{O}$  incorporation into coexisting phases (Figure 15). Element (cation) abundances are reported in number of cations per 100 oxygens ( $N$  cation/100 O) in a phase, in order to facilitate a comparison of the content between different minerals.



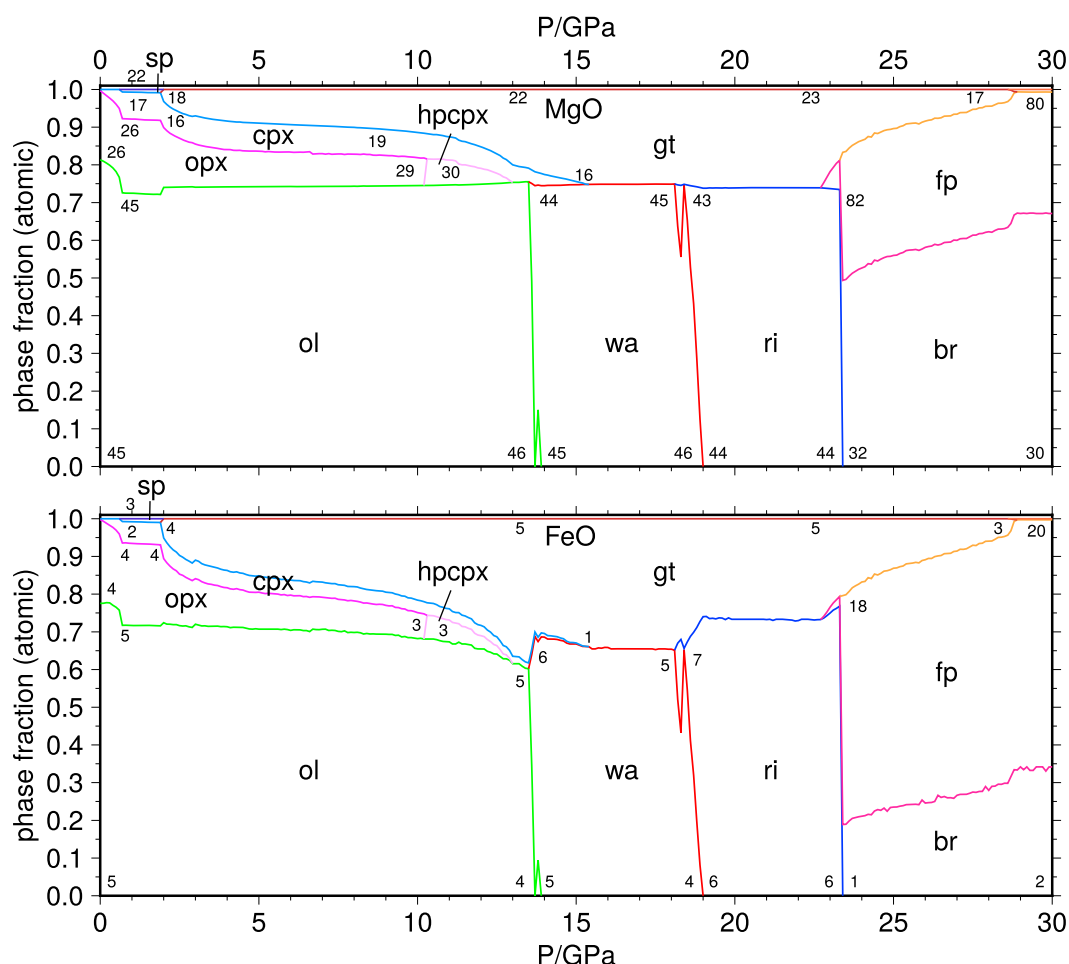


**Figure 14.** Phases hosting magnesium and iron for pyrolite bulk composition (Table 2), computed with the thermodynamic database of Stixrude and Lithgow-Bertelloni (2011). The graphs show the relative atomic amounts of stable phases (for abbreviations, see Table S1) containing (top) magnesium and (bottom) iron along the adiabat with a potential temperature of 1600 K. Labels in the panels indicate the content of  $\text{Mg}^{2+}$  and  $\text{Fe}^{2+}$  (number of cations per 100 oxygen anions) for the different phases, respectively. A changing cation content is indicated by various numbers within a phase stability field.

For the  $\text{Mg}_2\text{SiO}_4$ - $\text{Fe}_2\text{SiO}_4$  phases, the Mg/Fe ratio follows the respective abundance of these elements in pyrolite, and differences in the Mg/Fe values between them are small. General trends that have emerged from experiments (e.g., Frost, 2003a; Kato et al., 2014; Ishii et al., 2011) and formulated in a thermodynamic model (Frost, 2003b) are reproduced. Pyroxene and garnet host smaller amounts of Mg and Fe due to the presence of  $\text{Al}_2\text{O}_3$  but are preferentially enriched in Fe over Mg (Figure 14). In the lower mantle, FeO is predicted to strongly partition into ferropericlase over bridgmanite, with an estimated distribution coefficient  $K_{D,\text{Fe}/\text{Mg}}^{\text{br}/\text{fp}} = 0.25$ . This is consistent with Mg-Fe $^{2+}$  partitioning between bridgmanite and ferropericlase established experimentally for both the FMS system and pyrolite at uppermost lower mantle conditions (e.g., Prescher et al., 2014; Sakai et al., 2009). By contrast, two experimentally determined features are not captured by the current thermodynamic data sets for the mantle (Holland et al., 2013; Stixrude & Lithgow-Bertelloni, 2011): (i) the spin crossover in both Fe-bearing bridgmanite and ferropericlase at pressure at the middle lower mantle (e.g., Kantor et al., 2009; McCammon et al., 2010) appears to strongly affect the Mg-Fe partitioning coefficient of Fe $^{2+}$  between bridgmanite and ferropericlase (Prescher et al., 2014); (ii) the presence of Fe $^{3+}$ , through a coupled substitution  $\text{Fe}^{3+}\text{Al}^{3+}\text{-Mg}^{2+}\text{Si}^{4+}$  in bridgmanite, appears to exert an important influence on the Mg-Fe exchange with other phases (e.g., Frost & Langenhorst, 2002; Prescher et al., 2014). Representation of these features would require a thermodynamic model for high- and low-spin states in the Fe-bearing end-members and calibration and addition of thermodynamic data for Fe $^{3+}\text{Al}^{3+}$ -bearing bridgmanite, following the example of Kurnosov et al. (2017), respectively.

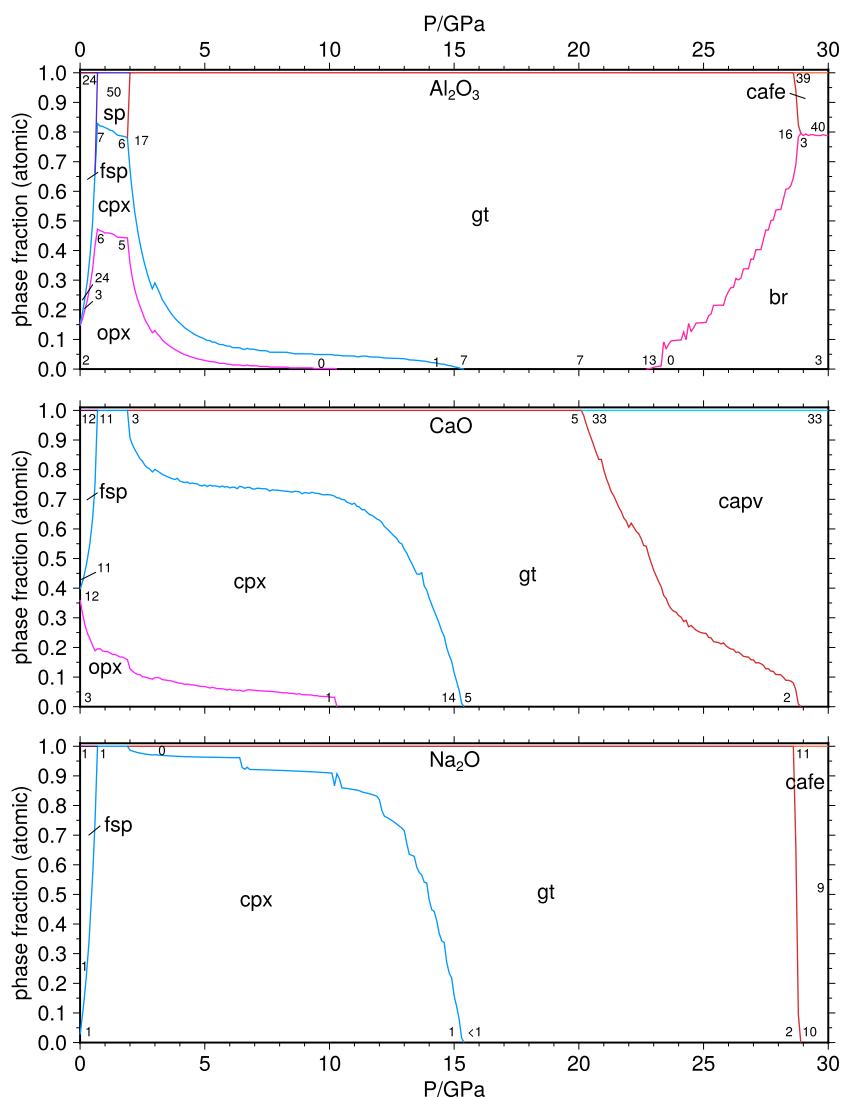


**Figure 15.** Phases hosting aluminum, calcium, and sodium for pyrolite bulk composition (Table 2), computed with the thermodynamic database of Stixrude and Lithgow-Bertelloni (2011). The graphs show the relative atomic amounts of stable phases (for abbreviations, see Table S1) containing (top)  $\text{Al}^{3+}$ , (middle)  $\text{Ca}^{2+}$ , and (bottom)  $\text{Na}^{+}$  along the adiabat with a potential temperature of 1600 K. Labels in the panels indicate the cation content of the different phases (number of cations per 100 oxygen anions). A changing cation content is indicated by various numbers within a phase stability field.

In the lowermost mantle, Mg-Fe partitioning between bridgmanite and ferropericlase, on the one hand, and postperovskite and ferropericlase, on the other hand, does not change appreciably in the model of Stixrude and Lithgow-Bertelloni (2011). By contrast, experimental results (e.g., Fujino et al., 2014; Sinmyo & Hirose, 2013) suggest that Fe is preferentially incorporated in bridgmanite over postperovskite, although early experiments suggested the opposite (e.g., Kobayashi et al., 2005).

Minor constituents in the peridotite mantle ( $\text{Al}_2\text{O}_3$ ,  $\text{CaO}$ , and  $\text{Na}_2\text{O}$ ) require respective end-members in the data set that represent their incorporation into and partitioning between relevant phases. When these components are important constituents of the solution phase, for instance,  $\text{Al}_2\text{O}_3$  in garnet, new phase stability fields will emerge at the expense of more simple assemblages (Figures 13). By contrast, end-members for new components control the exact location of discontinuities, and partitioning of minor constituents is very sensitive to the choice of composition and properties of the end-member (often fictitious, Table S1).

The presence of  $\text{Al}_2\text{O}_3$  produces minor fields of feldspar (with  $\text{Na}_2\text{O}$  and  $\text{CaO}$  in albite and anorthite, respectively, Table S1) and  $(\text{Mg,Fe})\text{Al}_3\text{O}_4$  spinel, as well as an extensive stability field of garnet that is the dominant

Al host over a wide range of  $P$  (Figures 9, 13, and 15). At low  $P$ , when spinel is stable,  $\text{Al}_2\text{O}_3$  is also present in clinopyroxene (jadeite and Ca-tschermak end-members) and orthopyroxene (Mg-tschermak) to a small extent (2 Al/100 O). When spinel transforms to garnet at 1.9 GPa, its pyrope-almandine-grossular solution accommodates a significant portion of  $\text{Al}_2\text{O}_3$  from the pyroxenes (Figure 15). As the pyroxene phases continuously dissolve in majoritic garnet, their  $\text{Al}_2\text{O}_3$  content decreases rapidly. With the formation of bridgmanite at 22.6 GPa (Figure 9), which preferentially consumes majorite and grossular, the Al content of garnet increases significantly, reaching values of 16 Al/100 O at 28.6 GPa, when it breaks down to the Ca-ferrite phase. This prediction is consistent with experimental data by Ishii et al. (2011) that show an increase from 7 to 10 Al/100 O for garnets in the  $P$  range between 20 and 25 GPa. In the lower-mantle phase assemblage, computed with the thermodynamic database of Stixrude and Lithgow-Bertelloni (2011), the Ca-ferrite phase with a high content of Al (40 Al/100 O) remains a minor Al host along with modally abundant bridgmanite (3 Al/100 O), similar to experimentally determined values (e.g., Ishii et al., 2011; Nakajima et al., 2012).

The CaO component is incorporated as anorthite in plagioclase at low  $P$ , coexisting with abundant orthopyroxene (orthodiopside, hedenbergite, and a minor Ca-tschermak component). With increasing  $P$ , calcium is transferred to the clinopyroxene solution (Figure 15). The Ca content of the coexisting orthopyroxene (orthodiopside, Table S1) remains low, quantitatively consistent with data by (Férot & Bolfan-Casanova, 2012). As the clinopyroxene abundance decreases in the mantle assemblage in favor of garnet, the CaO budget is progressively partitioned into the grossular component, with a maximum between 15.3 and 20.1 GPa (Figure 15). Garnet hosts 5 Ca/100 O, in close agreement with the maximum solubility established for a peridotite composition (6 Ca/100 O) (Saikia et al., 2008). With the formation of Ca-perovskite above 20.1 GPa, the garnet contribution to the CaO budget decreases at a rate consistent with experimental data (Ishii et al., 2011; Saikia et al., 2008).

The budget of  $\text{Na}_2\text{O}$  in pyrolite is initially completely accommodated by feldspar, although the albite component is low, consistent with the small ratio of  $\text{Na}_2\text{O}/\text{CaO}$  in bulk pyrolite (Figure 15 and Table 2). With increasing  $P$  along the 1600 K isentrope, feldspar transformation to spinel and clinopyroxene between 0 and 0.7 GPa (Figure 9) causes its  $\text{Na}_2\text{O}$  content to be transferred to clinopyroxene (jadeite). When garnet starts forming at 1.9 GPa with the  $\text{Al}_2\text{O}_3$  from spinel (Figure 13), sodium is incorporated in garnet through its jadeite-majorite component. The Na-content of the garnet solid solution is moderated by the behavior of principal garnet end-members: at 20.1 GPa exsolution of Ca-perovskite from garnet commences, and progressively, the jadeite-majorite component is passively enriched. At 28.6 GPa, jadeite-majorite is the last garnet component to transform to a lower-mantle phase, Ca-ferrite (Figures 9 and 15). The presence of the  $\text{Na}_2\text{O}$ -bearing phases described here strongly depend on the database, with a very restricted set of phases in Stixrude and Lithgow-Bertelloni (2011) (Table S1). By contrast, the solution models of Holland et al. (2013) include, in addition, a jadeite component in bridgmanite and the  $\text{Na}_2\text{O}-\text{Al}_2\text{O}_3$ -rich NAL phase (e.g., Kato et al., 2013).

## 5.2. Petrology of Slab Lithologies

Production of basaltic oceanic crust at mid-ocean ridges (~7 km thick) by partial melting of primitive mantle (pyrolite) leaves behind a complementary depleted mantle (~35 km thick) (Baker & Beckett, 1999). During subduction, these two lithologies play distinctive chemical, mechanical, and dynamical roles (e.g., Arredondo & Billen, 2016; Emmerson & McKenzie, 2007; Maierová et al., 2012). Density differences between the subducting lithosphere and the ambient mantle can lead to acceleration or stagnation of the slab (e.g., Christensen & Hofmann, 1994; Maierová et al., 2012). Similarly, an understanding of seismic velocities in the different lithologic layers can be used to trace subducting slab structure (e.g., Bostock, 2013) or be employed in forward modeling of seismic properties and wave propagation (e.g., Ricard et al., 2005; Shapiro et al., 2000).

On a geologic time scale, the rehomogenization of basalt and depleted mantle by both mechanical stirring (e.g., Kellogg & Turcotte, 1990; Nakagawa et al., 2010; Tirone et al., 2016) and chemical diffusion (e.g., Fei et al., 2012; Holzapfel et al., 2005; Shimojuku et al., 2009) is a slow process, leading to the concept of a marble cake mantle (Allègre & Turcotte, 1986). As a consequence, it has been argued that the bulk mantle may be better described by a mechanical mixture of basalt and depleted mantle deriving from differentiated lithosphere rather than by a single, homogeneous pyrolite composition (Brandenburg & van Keken, 2007; Davies, 1984; Xu et al., 2008; Nakagawa et al., 2010), a premise that we revisit in section 6.2.2. Therefore, we explore the phase relations (Figures 16, S11, and S12) and various physical properties (section 6) in simplified basaltic crust and depleted peridotite. We use a recently developed chemical model for bulk oceanic crust (BOC) and

depleted mantle (DM) (Chemia et al., 2015) (Table 2), in which the BOC composition is determined by analysis of the most primitive mid-ocean ridge basalt glasses. The DM composition is estimated as the complement to BOC using a melt fraction of 0.206, such that together they recombine to primitive mantle (McDonough & Sun, 1995).

### 5.2.1. Phase Relations in Depleted Mantle

With an  $\text{SiO}_2$  content slightly lower than pyrolite (Table 2), the depleted mantle shows phase assemblages similar to pyrolite (Figure S11), but with a larger proportion of  $\text{Mg}_2\text{SiO}_4$ -based minerals (Figure 16). As  $\text{Na}_2\text{O}$  is perfectly incompatible in olivine and orthopyroxene, the depleted mantle does not retain any  $\text{Na}_2\text{O}$  and hence phases containing sodium are absent in the DM phase assemblages. In particular, this leads to the absence of the Ca-ferrite phase in the lower mantle and a reduction in the clinopyroxene stability at upper mantle pressures, similar to the phase relations in the reduced CFMAS pyrolite composition (Figures 9 and S10). At pressures below 1 GPa, CaO and  $\text{Al}_2\text{O}_3$  are incorporated in clinopyroxene and anorthite (Figures 16 and S11), but the transition to spinel that is typical for pyrolite (Figures 9 and 12) is absent due to the low abundance of  $\text{Al}_2\text{O}_3$ , which is entirely accommodated by the pyroxene solid solutions. This is qualitatively consistent with calculations using the database of Holland and Powell (1998) on the same composition (Chemia et al., 2015), where the spinel stability is restricted to  $T < 1050$  K.

While phase transitions of the  $\text{Mg}_2\text{SiO}_4$ -based minerals in the depleted mantle occur at the same pressure and with the same Clapeyron slopes as in pyrolite, the phase relations in the  $\text{MgSiO}_3$ -based minerals change significantly. This is due to the strong depletion of both  $\text{Al}_2\text{O}_3$  and CaO in the DM composition (Table 2). Most importantly, the garnet stability range is significantly reduced when compared to pyrolite (Figure 13). The transformation of garnet to bridgmanite occurs at significantly lower pressure than predicted for pyrolite, but in good agreement with the experiments by Ishii et al. (2011). Along the 1600 K adiabat, with increasing  $P$ , garnet partially decomposes to ringwoodite and stishovite and then forms akimotoite, with a very narrow stability range (Figure 13). This resembles the phase relations in the pyrolite FMAS system (Figures 9 and 11), as the CaO component in DM exsolves Ca-perovskite from garnet at the same  $P$ , creating essentially a Ca-free garnet composition. The occurrence of coexisting garnet, stishovite and ringwoodite or garnet and akimotoite at  $\sim 20$  GPa is consistent with experiments by Irifune and Ringwood (1987) that have been performed at lower  $T$ , and the bridgmanite and ringwoodite coexistence between  $\sim 22.5$  GPa and  $\sim 23.5$  GPa agrees with experiments by Kato et al. (2014). Postperovskite formation occurs at slightly higher pressure than for pyrolite (Figures 12, 16, and S11).

### 5.2.2. Phase Relations in Bulk Oceanic Crust

With a mole fraction of silica,  $x(\text{SiO}_2) > 0.5$  (Table 2), the phase assemblages in the bulk oceanic crust consist, for the largest part, of coexisting  $\text{MgSiO}_3$ -based minerals and a free  $\text{SiO}_2$  phase (Figures 16 and S12). With BOC strongly enriched in CaO,  $\text{Al}_2\text{O}_3$ , and  $\text{Na}_2\text{O}$  relative to pyrolite (Table 2), phase relations between pyroxenes, garnet, akimotoite (Figure 13), and other lower-mantle phases show significant differences to pyrolite.

At 1600 K and ambient pressure, the phase assemblage predicted is olivine, orthopyroxene, and plagioclase (Figures 16 and S12). With increasing pressure along the 1600 K isentrope, olivine and plagioclase are replaced by clinopyroxene and garnet, with minor quantities of  $\beta$ -quartz, a typical phase assemblage for basalt at upper mantle conditions (e.g., Irifune & Ringwood, 1993; Ricolleau et al., 2010). At high  $P$ , the occurrence of pyroxene-based phases along the 1600 K isentrope is similar to pyrolite, with the exception that high-pressure clinopyroxenes—with only  $\text{MgSiO}_3$  and  $\text{FeSiO}_3$  in the solid solution (Table S1)—are not predicted stable (Figures 16 and S13). Similarly, the stability range of orthopyroxene is limited to the same pressure as plagioclase. Garnet and clinopyroxene with their wide range of solid solutions (Table S1) dominate the phase assemblage, with clinopyroxene dissolving into garnet, as already described for the pyrolite lithologies (section 5.1.1). The Ca-perovskite-forming reaction from garnet is predicted at significantly lower  $P$  than experimentally observed (Irifune & Ringwood, 1993; Litasov & Ohtani, 2005). At  $P > 20$  GPa, the phase relations computed here (Figures 16 and S12) and determined in experiments (Hirose et al., 1999; Irifune & Ringwood, 1993; Litasov & Ohtani, 2005; Ricolleau et al., 2010) differ significantly. In the experiments, a  $\text{Na}_2\text{O}$ - $\text{Al}_2\text{O}_3$ -rich (NAL) phase (Imada et al., 2012; Kato et al., 2013) coexists with Ca-ferrite to  $P > 40$  GPa. The NAL phase is not included in the assessment of Stixrude and Lithgow-Bertelloni (2011), which can, in part, account for the following two observations (Figures 13, S12, and 16): (i) garnet—with its end-members jadeite-majorite and pyrope—stays stable over a wide  $P$  range, before  $\text{Al}_2\text{O}_3$ -rich compositions of akimotoite and bridgmanite as well as  $\text{Na}_2\text{O}$ -bearing Ca-ferrite are formed near 30 GPa, consistent with computations by Xu et al. (2008);

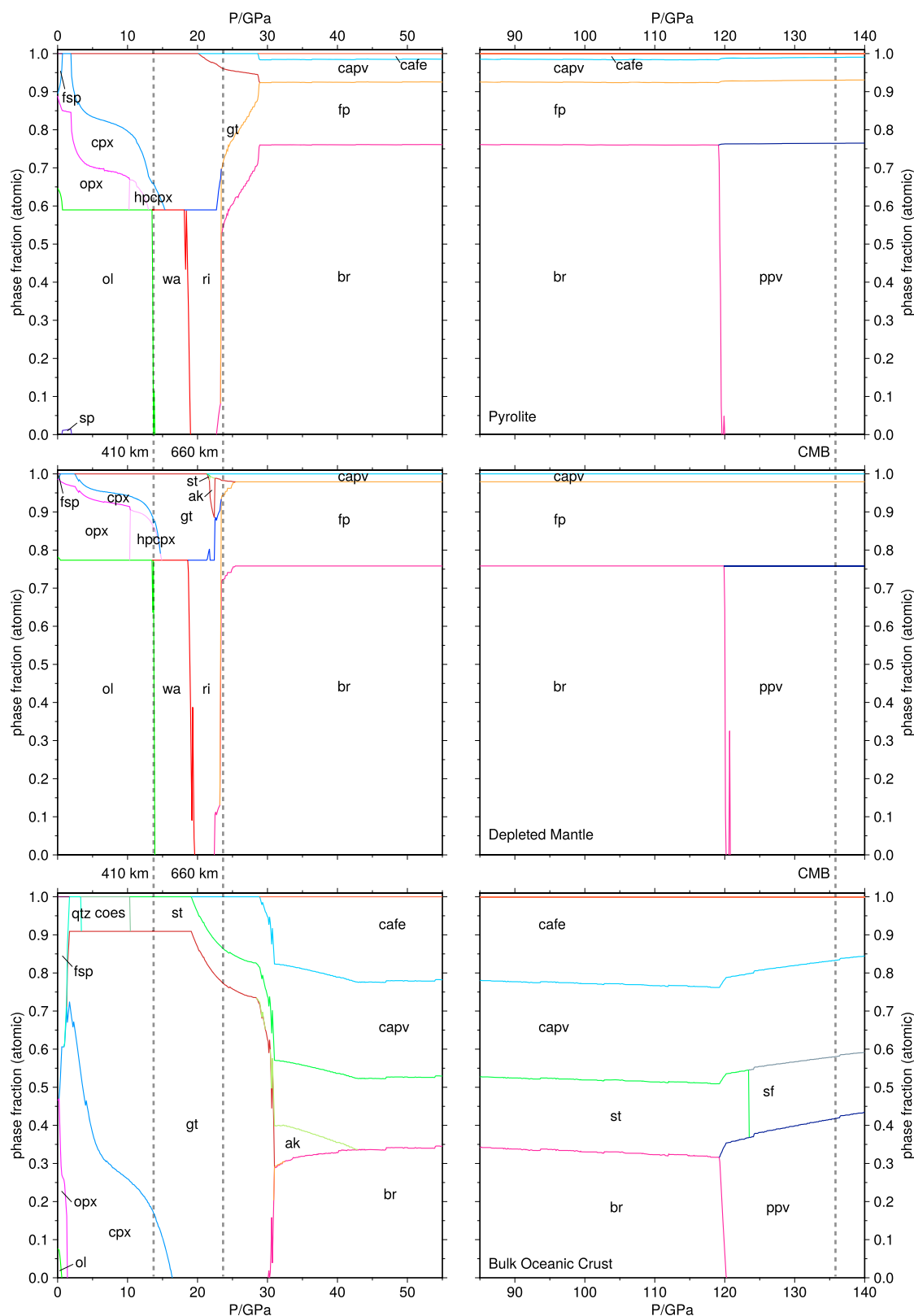


**Figure 16.** Comparison of the stable phase assemblages computed in the  $P$  ranges (left column) 0–55 GPa and (right column) 85–140 GPa with MMA-EoS using model parameters from Stixrude and Lithgow-Bertelloni (2011) for different lithologies: (top) Pyrolite, (middle) depleted mantle, and (bottom) bulk oceanic crust (Table 2). The graphs show the relative atomic amounts of stable phases (for abbreviations, see Table S1) for the different lithologies along the isentropes with a potential temperature of 1600 K. Pressures of the 410 km and 660 km discontinuities as well as the CMB are indicated by vertical dashed lines.

(ii) akimotoite is predicted to remain stable in BOC to more than 40 GPa (Figure 13). This is a significantly larger pressure than determined in Xu et al. (2008). The discrepancy in phase assemblage predictions presented here and the closely related results by Xu et al. (2008) (Figure S13) is caused by two factors: (i) differences in basalt composition used in Xu et al. (2008) (Presnall & Hoover, 1987) and here (Chemia et al., 2015); (ii) differences in the data sets by Xu et al. (2008) and Stixrude and Lithgow-Bertelloni (2011), in particular, those stabilizing bridgmanite (Fe component) and jadeite-majorite (Table S1).

At lowermost mantle pressures, postperovskite in bulk oceanic crust is formed over a narrow coexistence region at conditions very similar to those for pyrolite and depleted mantle (Figures 16 and S12), although experiments (Grocholski et al., 2012; Ohta et al., 2008) suggest a somewhat lower transition pressure.

Along the 1600 K isentrope for bulk oceanic crust,  $\beta$ -quartz transforms to coesite and then to stishovite (Figures 16 and S12), in good agreement with experiments (e.g., Zhang et al., 1993) and prior thermodynamic assessments (e.g., Swamy et al., 1994). At pressures of the lower mantle, stishovite undergoes a displacive phase transition from the rutile to the  $\text{CaCl}_2$  structure that is accounted for by a Landau model (section S1.5), with a transition  $P$  again in good agreement with experiments (Ono et al., 2002). The transformation to seifertite ( $\text{PbO}_2$ -structured  $\text{SiO}_2$ ) is predicted in the model by Stixrude and Lithgow-Bertelloni (2011) at 125 GPa, that is, at higher pressure than the postperovskite transition (Figures 16 and S12), in agreement with experiments by Grocholski et al. (2013).

## 6. Thermochemical Properties of the Mantle

### 6.1. Adiabatic Temperatures

We use the stable-phase assemblages and their thermodynamic properties to determine isentropic  $T$  profiles as a function of pressure to define mantle adiabats and geotherms (Ganguly et al., 2009; Turcotte & Schubert, 2002). In our approach, we calculate the entropy content of a lithology at the potential temperature and 0 GPa and trace this entropy value as a function of  $P$ . This provides an exact solution to an alternative formulation of the adiabat

$$\left(\frac{\partial T}{\partial P}\right)_S = \frac{\alpha}{\rho C_p} \cdot T, \quad (6)$$

often used in geophysics, where values for density  $\rho$  and thermal expansivity  $\alpha$  are usually based on  $P$ - $V$ - $T$  experimental data (e.g., Brown & Shankland, 1981; Katsura et al., 2010; Stacey & Davis, 2008).

Within a specific phase stability field,  $T$  along the isentrope increases smoothly due to self-compression, whereas at phase transitions, temperature can change discontinuously, through volume collapse and latent heat release or consumption due to a positive or negative Clausius-Clapeyron slope, respectively (e.g., Verhoogen, 1965). Examples for latent heat release are the transformations of olivine to wadsleyite and wadsleyite to ringwoodite, for latent heat consumption the ringwoodite breakdown (section 5.1.1). Here we follow isentropes for pyrolite, depleted mantle, and bulk oceanic crust with a potential temperature of 1600 K, assumed to be typical for the mantle (e.g., Herzberg et al., 2007), as well as those with potential temperatures of 1400 and 1800 K. The reference potential temperature chosen here (1600 K) is at the lower end of recent estimates for mid-ocean ridge basalt extraction (Dalton et al., 2014; Sarafian et al., 2017).

#### 6.1.1. Isentrope in Pyrolite Mantle

The 1600 K isentrope for pyrolite is characterized by three discontinuities, representing the olivine to wadsleyite, wadsleyite to ringwoodite transitions, and the ringwoodite breakdown, respectively (Figure 17). Of those, wadsleyite transforms to ringwoodite through a significant coexistence region (section 5.1.1) and the associated temperature increase is distributed between the ringwoodite-in and wadsleyite-out reactions (Figures 9 and 12). By contrast, in the  $\text{MgSiO}_3$ -based system the phase transitions occur through wide coexistence regions, and only the orthopyroxene-out (10.3 GPa), bridgmanite-in (22.5 GPa) and garnet-out (28.6 GPa) reactions are associated with a small  $T$  increase along the 1600 K isentrope (Figures 12 and 17), similar to the predictions by Stixrude and Lithgow-Bertelloni (2011). At the base of the mantle, the occurrence of postperovskite leads to a significant  $T$  increase, consistent with the large positive Clapeyron slope of the transition (section 5.1.1).

The model results show that the  $T$  increase along an isentrope with pressure varies significantly for different potential temperatures. Hotter isentropes reach a larger temperature difference than colder ones across the mantle. For instance, along the 1600 K isentrope the temperature increases by  $\sim 1100$  K, while for isentropes



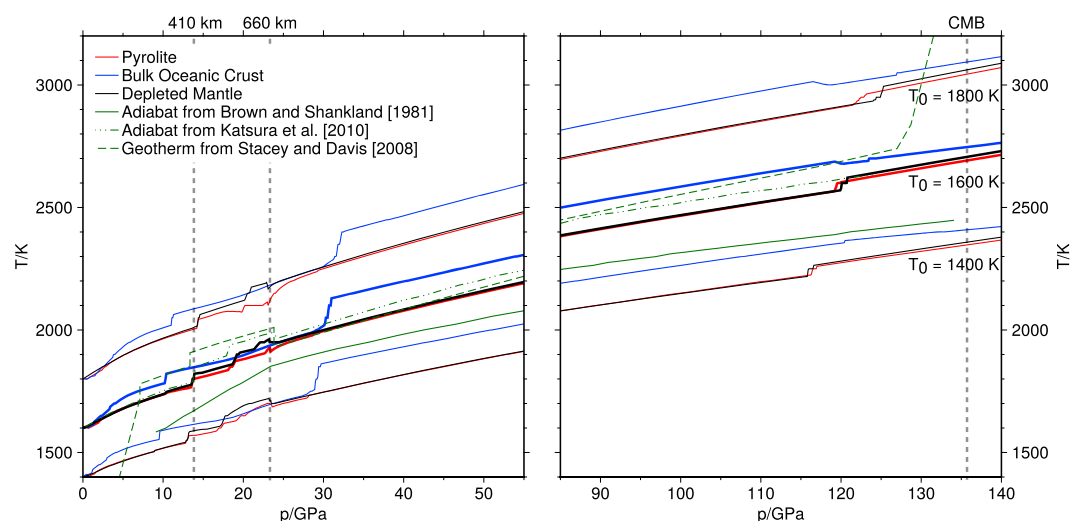


**Figure 17.** Self-consistently computed isentropes using the model parameters from Stixrude and Lithgow-Bertelloni (2011) for three different lithologies, representing the average mantle (pyrolite, red lines) and both the basaltic (bulk oceanic crust, blue lines) and the depleted part (depleted mantle, black lines) of oceanic lithosphere. Adiabats with potential temperatures of 1400 K, 1600 K, and 1800 K are shown for a pressure range of (left) 0–55 GPa and of (right) 85–140 GPa. For comparison, the adiabats by Brown and Shankland (1981) (green solid line) and Katsura et al. (2010) (green dash-dotted line), as well as the geotherm by Stacey and Davis (2008) (green dashed line), are included. Vertical dashed lines indicate the pressure of the 410 km and 660 km discontinuities (Figure 17, left) and the core-mantle boundary (Figure 17, right).

with a potential temperature of 200 K lower and higher, the differences reach ~950 and ~1250 K, respectively. If hot spot volcanism with an excess  $T$  of ~200 K at extraction (Herzberg et al., 2007) is indeed caused by thermal plumes that rise adiabatically from the core-mantle boundary, their excess temperature in the lower mantle is predicted to be ~350 K, consistent with previous estimates (Kennett & Bunge, 2008; Piazzoni et al., 2007). Combined with the consideration that plumes rise quasi-adiabatically, while the surrounding mantle is subadiabatic due to slow overturn (Bunge, 2005; Jeanloz & Morris, 1987), this observation supports the notion of a stronger contribution of plumes to the global heat budget than often thought (e.g., Davies, 1993).

A comparison between the 1600 K adiabat and adiabatic gradients computed here and by Katsura et al. (2010) illustrates the importance of considering the full phase assemblage rather than individual phases (Figures 17 and S15). Temperature discontinuities produced at major phase transitions are less pronounced in a complex and realistic multiphase assemblage, and phase changes in the  $\text{MgSiO}_3$ -based systems as well as redistribution of elements between different phases act as significant temperature buffers.

### 6.1.2. Isentropes in Slab Lithologies

Isentropes for a depleted mantle composition show stronger  $T$  discontinuities (Figure 17) at the phase transitions of the  $\text{Mg}_2\text{SiO}_4$  minerals than in pyrolite, as a higher MgO budget results in larger proportions of olivine, wadsleyite, and ringwoodite in the assemblage (Figure 16). This effect propagates to higher temperatures in the transition zone; an additional slight increase relative to pyrolite stems from the occurrence of akimotoite and its transformation to bridgmanite at 22.5 GPa (Figures 16 and 17). In the lower mantle, adiabatic gradients for harzburgite are shallower (Figure S14) and the isentropes become similar to those of pyrolite near 30 GPa.

For the oceanic crust, isentropes differ significantly from the peridotite assemblages both in terms of discontinuities and slopes (Figures 17 and S14), as phase transitions for  $\text{SiO}_2$  minerals dominate  $T$  discontinuities at upper mantle pressures (Figures 16 and S12). Therefore, and despite an overall lower gradient, bulk oceanic crust heats significantly more rapidly from adiabatic compression than the peridotitic mantle. Near 12 GPa, that is, above the coesite-stishovite transition in the bulk oceanic crust and below the olivine-wadsleyite transition in DM, temperature differences reach 80 K. With the latent heat release at the  $\text{Mg}_2\text{SiO}_4$  phase transformations, the isentropes for peridotitic mantle and bulk oceanic crust become comparable. Above 30 GPa, significant heat is added to the basalt assemblage by the garnet-out reaction (Figure 17), and throughout the lower mantle, the 1600 K isentrope for bulk oceanic crust stays hotter than those for the depleted mantle and pyrolite. The postperovskite transition is reached with a negative Clapeyron slope for bulk oceanic crust (Figure S12), resulting in a temperature decrease. However, the Clapeyron slope of this phase transition

is strongly  $T$  dependent, with a reversal at 2260 K and 121 GPa; in contrast to the 1600 K isentrope, the 1400 K adiabat experiences a slight  $T$  increase at the postperovskite transition.

The significantly steeper temperature increase for isentropes in the oceanic crust than for those in the surrounding pyrolytic or harzburgitic mantle implies that the crustal section of a subducting slab is heated at a faster rate than the underlying depleted mantle, to a degree that should influence thermal equilibration of the subducting slab. However, the latent heat contribution of the quartz-coesite transformation coincides with other, more significant, heat transport processes, such as the onset of full coupling between the slab and the mantle wedge (e.g., Peacock et al., 2005; Syracuse et al., 2010) or latent heat released due to devolatilization reactions (e.g., Chemia et al., 2015). With a significantly reduced volatile budget in the bulk oceanic crust at pressures above 5 GPa (e.g., Chemia et al., 2015; van Keken et al., 2011), the coesite-stishovite transformation should exert an effect on the thermal evolution of the slab worth exploring in subduction zone modeling.

## 6.2. Seismic Properties

### 6.2.1. Density and Elasticity Profiles of Individual Lithologies

Profiles of density, compressional ( $v_p$ ) and shear wave velocity ( $v_s$ ) computed along the 1600 K isentrope for pyrolite (Figure 18) are similar to previous estimates (e.g., Piazzoni et al., 2007; Vacher et al., 1998; Xu et al., 2008). Density, compressional, and shear wave velocity increase with pressure, and discontinuous changes are associated with phase transitions. The phase transformations in the  $\text{Mg}_2\text{SiO}_4$ -based systems have the largest effect and lead to discontinuities in  $\rho$  by 0.08, 0.06, and 0.10  $\text{g/cm}^3$  at the olivine-wadsleyite, wadsleyite-ringwoodite transitions and the ringwoodite breakdown, respectively. The relative magnitude of changes in  $v_p$  and  $v_s$  across these transitions is similar.

Transition pressures are in good agreement with the two major discontinuities in the seismic reference model AK135-f (Kennett et al., 1995; Montagner & Kennett, 1996) at depths of 410 and 660 km. The changes in density and seismic wave velocities at the 410 km discontinuity (13.2–13.8 GPa) are comparable to values of AK135-f, and so are the differences for the divariant wadsleyite-ringwoodite transition at 520 km (18.1–19.0 GPa, Figure 9). This is in contrast to values from experiments for pure olivine that yield significantly higher jumps (e.g., Mao et al., 2015; Sinogeikin et al., 1998), even if one accounts for the relevant phase proportions. At the 660 km discontinuity, the steps in density and seismic wave velocities are not captured quantitatively by the pyrolite system using the database of Stixrude and Lithgow-Bertelloni (2011) (Figure 18). The progressive disappearance of garnet at depths larger than 660 km is reflected to some extent in AK135-f, with a separate parameterization of the model between 660 and 1000 km depth. At higher  $P$ , in the absence of garnet,  $\rho$  and  $v_p$  agree well with the values of AK135-f, but  $v_s$  remains somewhat lower.

The increase of all three properties with pressure in the lower mantle is greater in seismic models than in predictions using the thermodynamic database of Stixrude and Lithgow-Bertelloni (2011) (Figure 18); these differences increase until the  $D''$  layer is reached. At the post-perovskite transition (120 GPa), density and shear wave velocity increase, while the compressional wave velocity decreases. For other phase transitions in the  $\text{MgSiO}_3$ -based system—with the exception of the formation of Ca-perovskite—notable discontinuities in at least the shear wave velocity are predicted, but values and impedances are predicted too low to be detected seismically.

In contrast to pyrolite, the major discontinuities arising from the  $\text{Mg}_2\text{SiO}_4$ -based minerals are more pronounced in the depleted mantle (Figure 18) due to its higher  $\text{Mg}_2\text{SiO}_4$  content (Figure 16). The simultaneous transformation of both pyroxenes into garnet for DM leads to a more pronounced discontinuity at 14.8 GPa in seismic wave velocities than for pyrolite. Similarly, the complex phase relations at pressures of the lower transition zone in DM result in more substantial changes for all parameters before the ringwoodite breakdown is reached. As the garnet disappearance occurs within 2 GPa of the ringwoodite breakdown, this transition is not individually resolvable in the profiles (Figure 18).

For bulk oceanic crust, density and seismic wave velocities at ambient pressure are significantly lower than for the other lithologies (Figure 18), but with eclogitization near 2 GPa (Figure 16) they become comparable. At higher pressure, the properties of the bulk oceanic crust are dominated by phase transitions of the  $\text{SiO}_2$  polymorphs; with the quartz-coesite transition at 3.3 GPa, density and seismic velocities become significantly larger than for the other lithologies at upper mantle conditions, and these differences are further enhanced at the coesite-stishovite transformation at 10.3 GPa. For transition zone pressures, BOC stays denser than pyrolite or depleted mantle due to the presence of stishovite and garnet, but seismic velocities become comparable

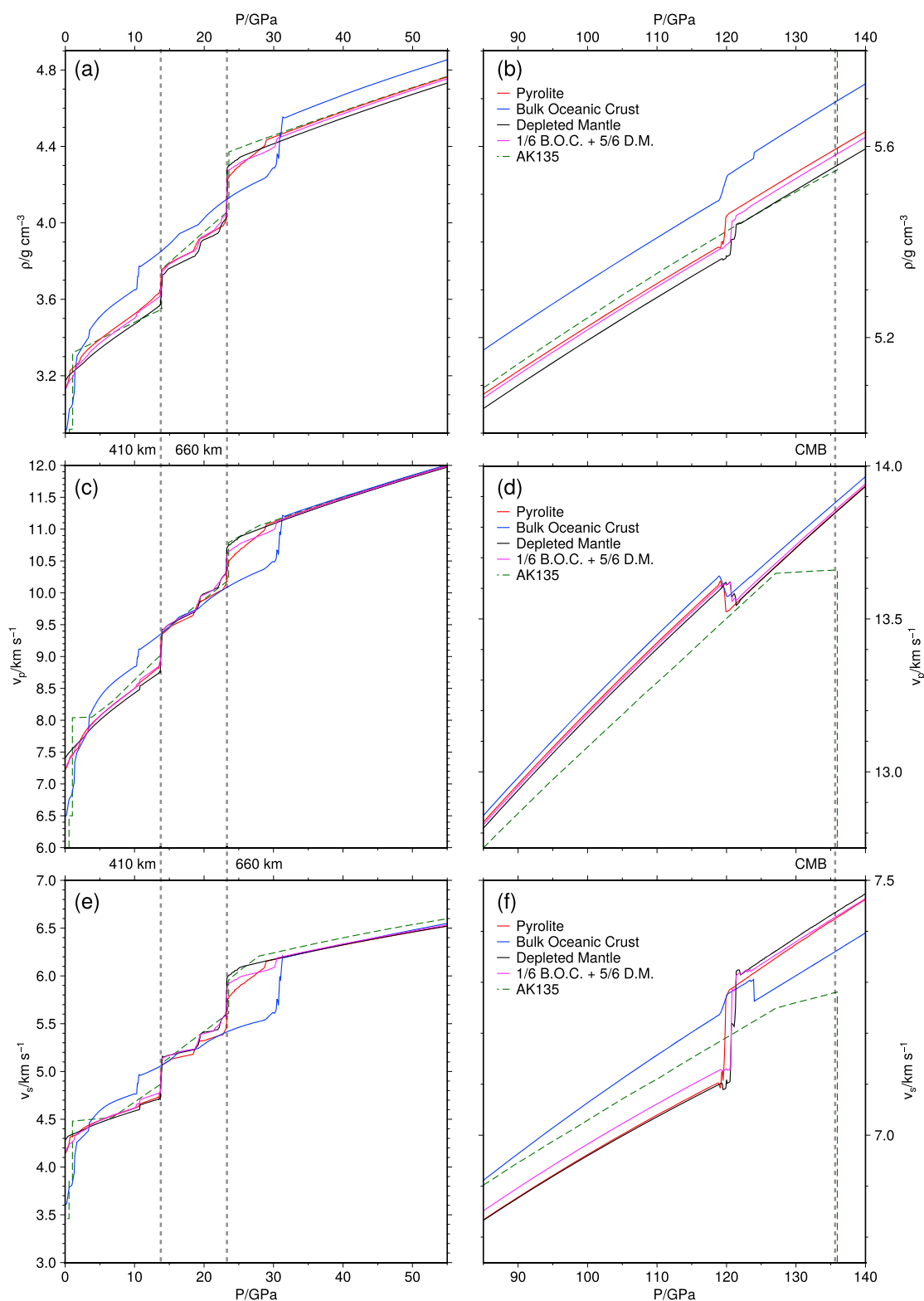


**Figure 18.** (a and b) Density, (c and d)  $P$  wave, and (e and f)  $S$  wave velocities for the three model lithologies pyrolite (red), bulk oceanic crust (blue), and depleted mantle (black) along their respective 1600 K adiabats (Figure 17). Properties of the mechanical mixture of 1/6 bulk oceanic crust with 5/6 depleted mantle (magenta) are shown along the adiabat for pyrolite. Physical parameters are computed with MMA-EoS using the model parameters from Stixrude and Lithgow-Bertelloni (2011). For comparison, profiles from AK135-f (Kennett et al., 1995; Montagner & Kennett, 1996) are included as dashed lines (green). Pressures for the 410 km and 660 km discontinuities and the core-mantle boundary are indicated by vertical dashed lines.

between the different lithologies due to the presence of the high-pressure  $\text{Mg}_2\text{SiO}_4$  phases in the two ultramafic lithologies. At uppermost lower mantle pressures, both density and seismic velocities are lower for BOC, as bridgmanite is formed only at 30 GPa in the basalt. Density trends of the primitive and depleted mantle and the oceanic crust presented here are qualitatively consistent with experiments (e.g., Irifune & Ringwood, 1993; Sinogeikin et al., 1998), but quantitatively, the differences in density between these lithologies are smaller in the thermodynamic model of Stixrude and Lithgow-Bertelloni (2011).

The results of the thermodynamic model discussed above are not applicable to the seismic structure of subduction zones directly, as temperatures are much lower than the adiabats presented here. A comparison between predicted data and seismic observations is further complicated as elastic parameters are affected by the presence of volatiles and crack microstructure (e.g., Adam & Otheim, 2013). Nevertheless, the crustal section of the subducting lithosphere can be traced by low  $v_s$ , in some instances to depths corresponding to the transformation to an eclogite assemblage. At pressures above 2 GPa, seismic velocities become comparable for the different lithologies, and subducted crust cannot be imaged further in most cases (e.g., Bostock, 2013). However, a detailed seismic study of the Cocos slab subducting below central Mexico (Kim et al., 2012) reveals a transition from a negative to a positive perturbation of  $v_s$  in the crustal section of the slab. This conversion coincides with the disappearance of the velocity contrast between the oceanic crust and depleted mantle sections of the slab and can be interpreted as elastic velocities in the different lithologies approaching similar values (Figure 18). The significant increase in seismic velocities of eclogitized BOC across the quartz-coesite transition, however, has not yet been mapped in a subducting slab.

### 6.2.2. Elasticity Profiles of Homogeneous Versus Mechanically Mixed Mantle

Differences in the 1-D profiles for seismic properties exist between a homogeneous pyrolitic mantle and a mechanical mixture of DM and BOC (5:1 by mass) in terms of the location and magnitude of discontinuities (Figure 18). These differences are caused by the larger number of phase transitions in the mechanical mixture that come from both its harzburgite and basalt components (Figure 16). However, compared to differences between the seismic observations and thermodynamic predictions, they are minor, and no significant advantage of using a mechanical mixture over a chemically homogeneous pyrolite is apparent.

This inference is best illustrated for the transition zone (Figure 18). On the one hand, velocity and density discontinuities occurring across all three major phase transitions are slightly larger for pyrolite than for the mechanical mixture and, therefore, in closer agreement with the seismic estimates, as are their gradients across the transition zone—measured as the absolute difference between values at 13.8 and 23.3 GPa. On the other hand, the absolute values for  $v_p$  and  $v_s$  in the transition zone are larger for the mechanical mixture and, therefore, in closer agreement with AK135-f. Gradients of seismic velocities for pyrolite and the mechanical mixture are virtually indistinguishable in both the upper and lower mantle.

Further considerations support the notion that current observations cannot differentiate properties computed for a mechanical mixture and a pyrolite aggregate. We want to illustrate this with three examples:

1. Chemical heterogeneity has been invoked to account for large values of the shear to compressional wave velocity ratio ( $R_{s/p} = d \ln v_s / d \ln v_p$ ) in Earth's lowermost mantle (e.g., Della Mora et al., 2011; Trampert et al., 2004). These large differences favor a mechanically mixed mantle, as the heterogeneity is often assumed to be accumulated basaltic oceanic crust (e.g., Brandenburg & van Keken, 2007; Nakagawa et al., 2009; Tackley, 2011). However, the basalt fractions involved would often have to be unrealistically high (e.g., Cammarano et al., 2009; Nakagawa et al., 2009; Tackley, 2011), and accumulation of oceanic crust in the lowermost mantle appears dynamically challenging (Li & McNamara, 2013). Furthermore, Tesoniero et al. (2016) have recently found that  $R_{s/p}$  values predicted for pyrolite and a mechanically mixed mantle do not differ in a significant way;
2. Ritsema, Xu, et al. (2009) and Ritsema, Cupillard, et al. (2009) have modeled arrival time differences for seismic phases sensitive to the 410 km and 660 km discontinuities (i.e., SS precursors and receiver functions) using synthetic transition zone structure with both a homogeneous pyrolite and a mechanical mixture model. While they find the variation in transition zone thickness to be similar for both pyrolite and mechanical mixture, the temperature models based on travel time differences point to isentropes with potential temperature of 1700–1750 K for pyrolite and 1600–1650 K for the mechanical mixture, respectively. Originally, this inference has been used to support the notion of a mechanically mixed mantle, but with the recent upward revision of the potential temperature for the mantle adiabat (Dalton et al., 2014; Sarafian et al., 2017), this notion no longer holds;

3. Using the same  $v_p$ ,  $v_s$ , and  $\rho$  models as Ritsema, Xu, et al. (2009) and Ritsema, Cupillard, et al. (2009), Cammarano et al. (2011) have shown that a global data set of free oscillations and body wave travel times can, for the mechanical mixture, only be matched with temperatures in the upper 800 km of the mantle that fall below the 1600 K isentrope, that is, significantly below temperatures of Ritsema, Xu, et al. (2009) and Ritsema, Cupillard, et al. (2009).

We would like to end this section by emphasizing that a comparison of seismic reference profiles with computed 1-D profiles for  $\rho$ ,  $v_p$ , and  $v_s$  based on a thermodynamic-elastic model such as that of Stixrude and Lithgow-Bertelloni (2011) in inferring the thermal structure and composition of the Earth's mantle has inherent limitations for several reasons:

1. Attenuation plays a significant role in Earth's mantle for seismic frequencies (e.g., Goes et al., 2004; Karato, 1993; Stixrude & Lithgow-Bertelloni, 2005a), while elastic model properties are derived at experimental frequencies in the laboratory. In principle, an anelastic correction can be incorporated in a thermodynamic model as a postprocessing step, but large uncertainties exist with respect to the parameters entering the correction (Matas & Bukowski, 2007);
2. Temperature in Earth's mantle deviates from an adiabatic profile owing to radiogenic heat production and heat exchange due to slow overturn (e.g., Bunge, 2005; Cobden et al., 2008; Matas et al., 2007). Slightly lower temperatures in the transition zone would, for example, lead to the stability of akimotoite in pyrolite (Figures 12 and 13), with additional consequences for elastic properties;
3. The lateral average of a dependent property is not necessarily the same as the single value predicted along the  $T$  profile averaged a priori. For seismic properties, these two approaches yield close results in the lower mantle, but deviate substantially in the vicinity of phase transitions (e.g., Styles et al., 2011; Tesoniero et al., 2016).

## 7. Discussion and Concluding Remarks

### 7.1. Coverage, Consistency, and Accuracy of Thermodynamic Models

The practical significance of thermodynamic models and data sets is related to a number of criteria ranging from the completeness of the database (for a given problem) to the requirement that it should be formulated in a thermodynamically self-consistent way between individual phases and at the level of individual material properties. While these criteria are interlinked, we attempt to address four aspects separately and point out potential routes to resolve them.

1. A thermodynamic model should obey basic thermodynamic identities, such as Maxwell's relations, and should be physically reasonable, that is, approach correct limits at low or high  $T$  or  $P$ , especially if a model is used for extrapolations beyond the range of the thermodynamic assessment of the phases. As we discuss in the supporting information in detail (section S1) and demonstrate in section 4.1.2, significant differences exist in the formulation of the Birch-Murnaghan–Mie–Grüneisen–Debye (Stixrude & Lithgow-Bertelloni, 2011) and Caloric–Modified-Tait (Holland et al., 2013) models, in particular, for heat capacity. While the caloric model based on a polynomial expansion agrees much better with experimental data for heat capacity (Figure 4), the fact that the Debye model shows the correct asymptotic behavior of the Dulong–Petit limit at high  $T$ , makes this model more suitable for extrapolation. Nevertheless, poor representation of experimental data by the latter (Figure 4) is an issue of concern. Use of the Kieffer model (Kieffer, 1979a, 1979b) could significantly improve the situation, while maintaining thermodynamic self-consistency (e.g., Jacobs & de Jong, 2007; Jacobs et al., 2013), but its calibration for a sufficient number of phases of geological interest has not yet been undertaken.
2. In assessing available data for the end-members, a significant number of parameters need to be fit, with strong correlation between different parameters, for example, the bulk modulus and its pressure derivative from compression experiments (Angel, 2000), or between enthalpy and entropy when using phase equilibrium constraints (Gottschalk, 1997; Powell & Holland, 1985). Fitting of parameters has been performed sequentially (e.g., Stixrude and Lithgow-Bertelloni, 2005b, 2011) or simultaneously (e.g., Holland & Powell, 2011; Kennett & Jackson, 2009) and this choice strongly influences the parameter values, even for relatively well characterized phases. Using periclase as an example, significant differences in the properties that determine the Grüneisen parameter (Figure S1) exist between the assessments by Stixrude and Lithgow-Bertelloni (2011) and Kennett and Jackson (2009), which in turn strongly influence inferred mantle properties, ranging from the adiabatic  $T$  gradient to seismic velocities (Connolly & Khan, 2016). However,



adjusting parameters for specific phases only—with the goal to improve agreement with individual observations (e.g., Kurnosov et al., 2017)—may compromise the integrity of the data set, that is, its internal consistency and applicability (Connolly, 2009).

The comparison of phase assemblages in the bulk oceanic crust with different data sets of the Birch-Murnaghan–Mie–Grüneisen–Debye model (Stixrude & Lithgow-Bertelloni, 2011; Xu et al., 2008) illustrates that small differences in thermodynamic parameters have a large influence on phase stability fields (Figure S13). The occurrence of akimotoite in bulk oceanic crust when using the database of Stixrude and Lithgow-Bertelloni (2011) that is not predicted with the database of Xu et al. (2008) can be traced to small changes in the thermodynamic properties of the bridgmanite end-members and jadeite-majorite. In contrast to bulk oceanic crust, phase relations in pyrolite or depleted mantle remain insensitive to these changes in the data set. Such unexpected behavior illustrates that the thermodynamic model by Stixrude and Lithgow-Bertelloni (2011) is sufficiently constrained for peridotitic bulk composition, dominated by MgO and SiO<sub>2</sub>, but with only minor quantities of FeO, CaO, Al<sub>2</sub>O<sub>3</sub>, and Na<sub>2</sub>O. For higher contents of Al<sub>2</sub>O<sub>3</sub>, CaO, and Na<sub>2</sub>O, the uncertainties and discrepancies in the end-member or mixing properties propagate to the composition of interest and limit the applicability of the database. Phase assemblages computed for other bulk compositions, for example, for other terrestrial planets (e.g., Sohl & Schubert, 2015), therefore, require critical examination of the predictions.

3. In the treatment of solution phases, the parameterization of excess contribution to mixing properties remains among the most influential factors. The model of Stixrude and Lithgow-Bertelloni (2005a, 2011) uses pairwise interactions only (section S1.6 in the supporting information), as proposed by Powell and Holland (1993) and Berman and Aranovich (1996) for robust extrapolation outside the composition and *T* space of experimental constraints. Although some thermodynamic models for mineral solutions use asymmetric or intersite interaction parameters that may be further augmented by *T* or *P* dependence (e.g., Holland and Powell, 2003), available data for mantle phases are limited, and given uncertainties in calorimetric estimates (Figure 5), only in few cases more complex representations of the excess mixing properties are warranted.

For end-members of solutions that are not studied, unstable, or fictitious, that is, introduced as convenient compositional end-member, the assessment relies on extrapolations from the solution model to the end-member composition or on reciprocal systematics (Holland & Powell, 1998, 2011; Stixrude & Lithgow-Bertelloni, 2005a). The latter approach usually provides fictitious results that may be corrected by enthalpic and/or entropic increments when experimental data or natural observations are available (Powell, 1987), whereas the extrapolation from a solution model makes the end-member and solution properties mutually dependent with shared uncertainty (e.g., Holland & Powell, 2011), ultimately affecting phase relations. The significant differences in the experimentally well constrained phase diagram for the forsterite-fayalite join computed with various models and databases (Figure 7) illustrate the sensitivity to end-member parameterization, in this case due to the unstable Fe-wadsleyite. Additional experiments or simulations for compositions along the Mg<sub>2</sub>SiO<sub>4</sub>-Fe<sub>2</sub>SiO<sub>4</sub> binary would be required to better constrain the phase diagram and to stabilize the thermodynamic assessment of unstable end-members.

4. Issues of coverage or completeness of the data set are critical when phases are expected to occur that are not included in the database. A sodium aluminosilicate with nepheline composition (section 5.1.1), for example, is an important sodium host in the bulk oceanic crust to pressures above 40 GPa (e.g., Ricolleau et al., 2010), but—in contrast to Holland et al. (2013)—not assessed in the database of Stixrude and Lithgow-Bertelloni (2011). The chemical component in question is then predicted to be hosted in a different phase (metastably), leading to overestimated phase proportions and erroneous phase composition and physical properties, in this case the stability of Ca-ferrite. Often, integration of new end-members into a solution can significantly change physical properties within the solution. By adding an FeAlO<sub>3</sub> component to bridgmanite, the agreement between computed elastic profiles of the pyrolite model and seismic profiles improves significantly (Kurnosov et al., 2017); however, the influence of this additional component on phase stability has not been investigated and would probably require a revised assessment of all end-members in the bridgmanite solution, or a wider reassessment of phases that confine its stability field (e.g., Connolly, 2009).

## 7.2. Consequences for Geophysical Applications

The development of thermodynamic models of mantle petrology has been largely driven by the desire to interpret seismic observations in terms of chemical composition and temperature of Earth's mantle.



Such efforts started for 1-D profiles (e.g., Ita & Stixrude, 1992; Vacher et al., 1998) (section 6.2) before shifting to lateral heterogeneity imaged by tomography (e.g., Schuberth et al., 2009b; Trampert et al., 2004). Similar to the discussion on the homogeneous versus a mechanically heterogeneous state of the mantle (section 6.2.2), the viability of a chemical boundary within the mantle (e.g., Duffy & Anderson, 1989; Kellogg et al., 1999) remains a matter of debate, with divergent conclusions (e.g., Kurnosov et al., 2017; Murakami et al., 2012; Ricolleau et al., 2009; Wang et al., 2015). Twenty years ago, Vacher et al. (1998) inferred that it is not possible to distinguish between a layered and a uniform mantle based on existing data, and this notion continues to hold to date. It gains new and quantitative support by a recent stochastic study, evaluating the effects of uncertainties in the assessed thermodynamic parameters of mantle phases on the resulting 1-D mantle structure in terms of adiabatic temperature, density, and seismic velocity profiles (Connolly & Khan, 2016).

As an alternative, thermodynamic models can serve as a tool for predictions in geophysics that are testable against observations or indirect inferences such as tomographic images. Using density alone, geodynamic simulations have successfully been used to describe geoid undulations and their time variations (Schaber et al., 2009). Similarly, it is possible to generate synthetic seismic data (e.g., travel time residuals) based on models that combine geodynamic simulations (pressure and temperature fields) and thermoelasticity of mantle petrology (e.g., Nakagawa et al., 2010; Schuberth et al., 2009b). Solving the full 3-D (an)elastic wave equation for this kind of models can lead to a characterization of wave field effects on a global (Schuberth et al., 2015) and regional scale (Maguire et al., 2016) in a self-consistent manner, and allows for a test of geophysical hypotheses directly against seismological observations (Schuberth et al., 2012).

## Acknowledgments

This work was supported by Deutsche Forschungsgemeinschaft (DFG, German Science Foundation) with grants STE1105/6 (Focus Program SPP 1375, SAMPLE) and STE1105/13 (Research Unit 2440, Matter under Planetary Conditions). We greatly appreciate helpful discussion with Zurab Chemia, Lorenzo Colli, Dan Frost, Brian Kennett, and Bob Myhill. Comments by two reviewers and the Associate Editor (Michael Walter) have significantly improved the manuscript. The full source code for the simulation software and all scripts used to prepare the figures in this manuscript and supporting information can be accessed and downloaded from the project website (<https://bitbucket.org/chust/eos>).

## References

- Adam, L., & Otheim, T. (2013). Elastic laboratory measurements and modeling of saturated basalts. *Journal of Geophysical Research: Solid Earth*, 118, 840–851. <https://doi.org/10.1002/jgrb.50090>
- Akaogi, M. (2007). Phase transitions of minerals in the transition zone and upper part of the lower mantle. *GSA Special Papers*, 421, 1–13. [https://doi.org/10.1130/2007.2421\(01\)](https://doi.org/10.1130/2007.2421(01))
- Akaogi, M., Yano, M., Tejima, Y., Iijima, M., & Kojitani, H. (2004). High-pressure transitions of diopside and wollastonite: Phase equilibria and thermochemistry of  $\text{CaMgSi}_2\text{O}_6$ ,  $\text{CaSiO}_3$  and  $\text{CaSi}_2\text{O}_5$  -  $\text{CaTiSiO}_5$  system. *Physics of the Earth and Planetary Interiors*, 143–144, 145–156.
- Allègre, C. J., & Turcotte, D. L. (1986). Implications of a two-component marble-cake mantle. *Nature*, 323, 123–127.
- Andrault, D., Bouhifd, M. A., Itié, J. P., & Richet, P. (1995). Compression and amorphization of  $(\text{Mg}, \text{Fe})_2\text{SiO}_4$  olivines: An X-ray diffraction study up to 10 GPa. *Physics and Chemistry of Minerals*, 22(2), 99–107. <https://doi.org/10.1007/BF00202469>
- Andrault, D., Bolfan-Casanova, N., & Guignot, N. (2001). Equation of state of lower mantle (Al, Fe)- $\text{MgSiO}_3$  perovskite. *Earth and Planetary Science Letters*, 193, 501–508.
- Angel, R. J. (2000). Equations of state. *Reviews in Mineralogy and Geochemistry*, 41(1), 35–59. <https://doi.org/10.2138/rmg.2000.41.2>
- Aranovich, L. Y., & Berman, R. G. (1996). Optimized standard state and solution properties of minerals—II. Comparisons, predictions and applications. *Contributions to Mineralogy and Petrology*, 126(1–2), 25–37. <https://doi.org/10.1007/s004100050233>
- Arredondo, K. M., & Billen, M. I. (2016). The effects of phase transitions and compositional layering in two-dimensional kinematic models of subduction. *Journal of Geodynamics*, 100, 159–174. <https://doi.org/10.1016/j.jog.2016.05.009>
- Ashcroft, N. W., & Mermin, N. D. (1976). *Solid state physics*. Philadelphia: Saunders.
- Asimow, P. D., & Ghiorso, M. S. (1998). Algorithmic modifications extending melts to calculate subsolidus phase relations. *American Mineralogist*, 83, 1127–1132.
- Baker, M. B., & Beckett, J. R. (1999). The origin of abyssal peridotites: A reinterpretation of constraints based on primary bulk compositions. *Earth and Planetary Science Letters*, 171, 49–61.
- Bale, C., Chartrand, P., Degterov, S., Eriksson, G., Hack, K., Mahfoud, R. B., ... Petersen, S. (2002). FactSage thermochemical software and databases. *Calphad*, 26(2), 189–228.
- Bale, C., Bélisle, E., Chartrand, P., Degterov, S., Eriksson, G., Hack, K., ... Petersen, S. (2009). FactSage thermochemical software and databases—Recent developments. *Calphad*, 33(2), 295–311. <https://doi.org/10.1016/j.calphad.2008.09.009>
- Benisek, A., Etzel, K., & Cemic, L. (2007). Thermodynamic mixing behavior of synthetic Ca-Tschermak-diopside pyroxene solid solutions: II. Heat of mixing and activity-composition relationships. *Physics and Chemistry of Minerals*, 34, 747–755. <https://doi.org/10.1007/s00269-007-0192-4>
- Berman, R. G., & Aranovich, L. Y. (1996). Optimized standard state and solution properties of minerals—I. Model calibration for olivine, orthopyroxene, cordierite, garnet, and ilmenite in the system  $\text{FeO-MgO-CaO-Al}_2\text{O}_3\text{-TiO}_2\text{-SiO}_2$ . *Contributions to Mineralogy and Petrology*, 126(1–2), 1–24. <https://doi.org/10.1007/s004100050232>
- Birch, F. (1947). Finite elastic strain of cubic crystals. *Physical Review*, 71(11), 809–824. <https://doi.org/10.1103/PhysRev.71.809>
- Bostock, M. G. (2013). The Moho in subduction zones. *Tectonophysics*, 609, 547–557. <https://doi.org/10.1016/j.tecto.2012.07.007>
- Bouhifd, M. A., Andrault, D., Fiquet, G., & Richet, P. (1996). Thermal expansion of forsterite up to the melting point. *Geophysical Research Letters*, 23(10), 1143–1146.
- Brandenburg, J. P., & van Keken, P. E. (2007). Deep storage of oceanic crust in a vigorously convecting mantle. *Journal of Geophysical Research*, 112, B06403. <https://doi.org/10.1029/2006JB004813>
- Brosh, E., Makov, G., & Shneck, R. Z. (2007). Application of CALPHAD to high pressures. *Calphad*, 31(2), 173–185. <https://doi.org/10.1016/j.calphad.2006.12.008>
- Brown, J. M., & Shankland, T. J. (1981). Thermodynamic parameters in the Earth as determined from seismic profiles. *Geophysical Journal International*, 66(3), 579–596. <https://doi.org/10.1111/j.1365-246X.1981.tb04891.x>
- Bunge, H.-P. (2005). Low plume excess temperature and high core heat flux inferred from non-adiabatic geotherms in internally heated mantle circulation models. *Physics of the Earth and Planetary Interiors*, 153(1–3), 3–10. <https://doi.org/10.1016/j.pepi.2005.03.017>

- Cammarano, F., Romanowicz, B., Stixrude, L., Lithgow-Bertelloni, C., & Xu, W. (2009). Inferring the thermochemical structure of the upper mantle from seismic data. *Geophysical Journal International*, 179, 1169–1185. <https://doi.org/10.1111/j.1365-246X.2009.04338.x>
- Cammarano, F., Tackley, P., & Boschi, L. (2011). Seismic, petrological and geodynamical constraints on thermal and compositional structure of the upper mantle: Global thermochemical models. *Geophysical Journal International*, 187(3), 1301–1318. <https://doi.org/10.1111/j.1365-246X.2011.05223.x>
- Canil, D. (1994). Stability of clinopyroxene at pressure-temperature conditions of the transition region. *Physics of the Earth and Planetary Interiors*, 86, 25–34.
- Carpenter, M. A., Powell, R., & Salje, E. K. (1994). Thermodynamics of nonconvergent cation ordering in minerals: I. An alternative approach. *American Mineralogist*, 79(11–12), 1053–1067.
- Catalli, K., Shim, S.-H., & Prakapenka, V. (2009). Thickness and Clapeyron slope of the post-perovskite boundary. *Nature*, 462(10), 782–785. <https://doi.org/10.1038/nature08598>
- Chantel, J. (2012). *Measurement of elastic properties of silicates at realistic mantle pressures* (PhD thesis). Retrieved from <https://epub.uni-bayreuth.de/83/>. Bayreuth, Germany: Universität Bayreuth.
- Chantel, J., Frost, D. J., McCammon, C. A., Jing, Z., & Wang, Y. (2012). Acoustic velocities of pure and iron-bearing magnesium silicate perovskite measured to 25 GPa and 1200 K. *Geophysical Research Letters*, 39, L19307. <https://doi.org/10.1029/2012GL053075>
- Chemia, Z., Dolejs, G., & Steinle-Neumann (2015). Thermal effects of variable material properties and metamorphic reactions in a three-component subducting slab. *Journal of Geophysical Research*, 120, 6823–6845. <https://doi.org/10.1002/2015JB012080>
- Christensen, U. R., & Hofmann, A. W. (1994). Segregation of subducted oceanic crust in the convecting mantle. *Journal of Geophysical Research*, 99(B10), 19,867–19,884. <https://doi.org/10.1029/93JB03403>
- Chudinovskikh, L., & Boehler, R. (2001). High-pressure polymorphs of olivine and the 660 km seismic discontinuity. *Nature*, 411, 574–577. <https://doi.org/10.1038/35079060>
- Cobden, L., Goes, S., Cammarano, F., & Connolly, J. A. D. (2008). Thermochemical interpretation of one-dimensional seismic reference models for the upper mantle: Evidence for bias due to heterogeneity. *Geophysical Journal International*, 175, 627–648. <https://doi.org/10.1111/j.1365-246X.2008.03903.x>
- Cobden, L., Goes, S., Ravenna, M., Styles, E., Cammarano, F., Gallagher, K., & Connolly, J. A. D. (2009). Thermochemical interpretation of 1-D seismic data for the lower mantle: The significance of nonadiabatic thermal gradients and compositional heterogeneity. *Journal of Geophysical Research*, 114, B11309. <https://doi.org/10.1029/2008JB006262>
- Cohen, R. E. (1986). Thermodynamic solution properties of aluminous clinopyroxenes: Nonlinear least squares refinements. *Geochimica et Cosmochimica Acta*, 50, 563–575. [https://doi.org/10.1016/0016-7037\(86\)90105-5](https://doi.org/10.1016/0016-7037(86)90105-5)
- Connolly, J. A. D. (2005). Computation of phase equilibria by linear programming: A tool for geodynamic modeling and its application to subduction zone decarbonation. *Earth and Planetary Science Letters*, 236, 524–541. <https://doi.org/10.1016/j.epsl.2005-04-033>
- Connolly, J. A. D. (2009). The geodynamic equation of state: What and how. *Geochemistry, Geophysics, Geosystems*, 10, Q10014. <https://doi.org/10.1029/2009GC002540>
- Connolly, J. A. D., & Khan, A. (2016). Uncertainty of mantle geophysical properties computed from phase equilibrium models. *Geophysical Research Letters*, 43, 5026–5034. <https://doi.org/10.1002/2016GL068239>
- Cottaar, S., Heister, T., Rose, I., & Unterborn, C. (2014). BurnMan: A lower mantle mineral physics toolkit. *Geochemistry, Geophysics, Geosystems*, 15, 1164–1179. <https://doi.org/10.1002/2013GC005122>
- Dalton, C. A., Langmuir, C. H., & Gale, A. (2014). Geophysical and geochemical evidence for deep temperature variations beneath mid-ocean ridges. *Science*, 344(6179), 80–83. <https://doi.org/10.1126/science.1249466>
- Dantzig, G. B. (1963). *Linear programming and extensions*. Princeton, NJ: Princeton University Press.
- Davies, D. R., Goes, S., Davies, J., Schuberth, B., Bunge, H.-P., & Ritsema, J. (2012). Reconciling dynamic and seismic models of Earth's lower mantle: The dominant role of thermal heterogeneity. *Earth and Planetary Science Letters*, 353–354, 253–269. <https://doi.org/10.1016/j.epsl.2012.08.016>
- Davies, G. F. (1984). Geophysical and isotopic constraints on mantle convection: An interim synthesis. *Journal of Geophysical Research*, 89, 6017–6040. <https://doi.org/10.1029/JB089iB07p06017>
- Davies, G. F. (1993). Cooling the core and mantle by plume and plate flows. *Geophysical Journal International*, 115(1), 132–146. <https://doi.org/10.1111/j.1365-246X.1993.tb05593.x>
- de Capitani, C., & Brown, T. H. (1987). The computation of chemical equilibrium in complex systems containing non-ideal solutions. *Geochimica et Cosmochimica Acta*, 51, 2639–2652.
- de Capitani, C., & Petrakakis, K. (2010). The computation of equilibrium assemblage diagrams with THERIAK/DOMINO software. *American Mineralogist*, 95, 1006–1016. <https://doi.org/10.2138/am.2010.3354>
- Debye, P. (1912). Zur Theorie der spezifischen Wärmen. *Annalen der Physik*, 344(14), 789–839. <https://doi.org/10.1002/andp.19123441404>
- Della Mora, S., Boschi, L., Tackley, P. J., Nakagawa, T., & Giardini, D. (2011). Low seismic resolution cannot explain S/P decorrelation in the lower mantle. *Geophysical Research Letters*, 38, L12303. <https://doi.org/10.1029/2011GL047559>
- Downs, R. T., Zha, C.-S., Duffy, T. S., & Finger, L. W. (1996). The equation of state of forsterite to 17.2 GPa and effects of pressure media. *American Mineralogist*, 81, 51–55.
- Duffy, T. S., & Anderson, D. L. (1989). Seismic velocities in mantle minerals and the mineralogy of the upper mantle. *Journal of Geophysical Research*, 94(B2), 1895–1912.
- Emmerson, B., & McKenzie, D. (2007). Thermal structure and seismicity of subducting lithosphere. *Physics of the Earth and Planetary Interiors*, 163, 191–208. <https://doi.org/10.1016/j.pepi.2007.05.007>
- Eriksson, G., & Rosen, E. (1973). Thermodynamic studies of high-temperature equilibria. 8. General equations for calculations of equilibria in multiphase systems. *Chemica Scripta*, 4(5), 193–194.
- Fabrichnaya, O., Saxena, S. K., Richet, P., & Westrum, E. F. (2004). *Thermodynamic data, models, and phase diagrams in multicomponent oxide systems*. Berlin: Springer.
- Fan, D. W., Zhou, W. G., Liu, C. Q., Liu, Y. G., Wan, F., Xing, Y. S., ... Xie, H. S. (2009). The thermal equation of state of (Fe<sub>0.86</sub>Mg<sub>0.07</sub>Mn<sub>0.07</sub>)<sub>3</sub>Al<sub>2</sub>Si<sub>3</sub>O<sub>12</sub> almandine. *Mineralogical Magazine*, 73(1), 95–102. <https://doi.org/10.1180/minmag.2009.073.1.95>
- Fei, H., Hegoda, C., Yamazaki, D., Wiedenbeck, M., Yurimoto, H., Shcheka, S., & Katsura, T. (2012). High silicon self-diffusion coefficient in dry forsterite. *Earth and Planetary Science Letters*, 345–348, 95–103. <https://doi.org/10.1016/j.epsl.2012.06.044>
- Fei, Y., & Bertka, C. M. (1999). Phase transitions in the Earth's mantle and mantle petrology. In Y. Fei, C. M. Bertka, & B. O. Mysen (Eds.), *Mantle Petrology: Field observations and high pressure experimentation* (pp. 189–207). Houston, TX: Geochemical Society.
- Fei, Y., Saxena, S., & Eriksson, G. (1986). Some binary and ternary silicate solution models. *Contributions to Mineralogy and Petrology*, 94, 221–229.

- Fei, Y., van Orman, J., Li, J., van Westrenen, W., Sanloup, C., Minarik, W., ... Funakoshi, K. (2004). Experimentally determined postspinel transformation boundary in  $\text{Mg}_2\text{SiO}_4$  using MgO as an internal pressure standard and its geophysical implications. *Journal of Geophysical Research*, 109, B02305. <https://doi.org/10.1029/2003JB002562>
- Finkelstein, G. J., Dera, P. K., Jahn, S., Oganov, A. R., Holl, C. M., Meng, Y., & Duffy, T. S. (2014). Phase transitions and equation of state of forsterite to 90 GPa from single-crystal X-ray diffraction and molecular modeling. *American Mineralogist*, 99, 35–43. <https://doi.org/10.2138/am.2014.4526>
- Fiquet, G., Dewaele, Q., Andrault, D., Kunz, M., & Bihan, T. L. (2000). Thermoelastic properties and crystal structure of  $\text{MgSiO}_3$  perovskite at lower mantle pressure and temperature conditions. *Geophysical Research Letters*, 27(1), 21–24.
- Frost, D. J. (2003a).  $\text{Fe}^{2+}$ -Mg partitioning between garnet, magnesio-wüstite, and (Mg, Fe) $_2\text{SiO}_4$  phases of the transition zone. *American Mineralogist*, 88, 387–397.
- Frost, D. J. (2003b). The structure and sharpness of (Mg, Fe) $_2\text{SiO}_4$  phase transformations in the transition zone. *Earth and Planetary Science Letters*, 216, 313–328.
- Frost, D. J. (2008). The upper mantle and transition zone. *Elements*, 4, 175–180.
- Frost, D. J., & Langenhorst, F. (2002). The effect of  $\text{Al}_2\text{O}_3$  on Fe-Mg partitioning between magnesio-wüstite and magnesium silicate perovskite. *Earth and Planetary Science Letters*, 199, 227–241. [https://doi.org/10.1016/S0012-821X\(02\)00558-7](https://doi.org/10.1016/S0012-821X(02)00558-7)
- Fujino, K., Nishio-Hamane, D., Nagai, T., Seto, Y., Kuwayama, Y., Whitaker, M., ... Irifune, T. (2014). Spin transition, substitution, and partitioning of iron in lower mantle minerals. *Physics of the Earth and Planetary Interiors*, 228, 186–191. <https://doi.org/10.1016/j.pepi.2013.12.008>
- Férot, A., & Bolfan-Casanova, N. (2012). Water storage capacity in olivine and pyroxene to 14 GPa: Implications for the water content of the Earth's upper mantle and nature of seismic discontinuities. *Earth and Planetary Science Letters*, 349–350, 218–230. <https://doi.org/10.1016/j.epsl.2012.06.022>
- Ganguly, J. (2008). *Thermodynamics in earth and planetary sciences*. Berlin: Springer. <https://doi.org/10.1007/978-3-540-77306-1>
- Ganguly, J., Freed, A. M., & Saxena, S. K. (2009). Density profiles of oceanic slabs and surrounding mantle: Integrated thermodynamic and thermal modeling, and implications for the fate of slabs at the 660 km discontinuity. *Physics of the Earth and Planetary Interiors*, 172, 257–267. <https://doi.org/10.1016/j.pepi.2008.10.005>
- Gasparik, T. (1984). Experimentally determined stability of clinopyroxene + garnet + corundum in the system  $\text{CaO-MgO-Al}_2\text{O}_3\text{-SiO}_2$ . *American Mineralogist*, 69, 1025–1035.
- Gasparik, T. (1990a). Phase-relations in the transition zone. *Journal of Geophysical Research*, 95(B10), 15,751–15,769.
- Gasparik, T. (1990b). A thermodynamic model for the enstatite–diopside join. *American Mineralogist*, 75(9–10), 1080–1091.
- Gasparik, T. (2003). *Phase diagrams for geoscientists—An atlas of the earth's interior* (2nd edn.). Berlin: Springer.
- Ghiorso, M. S. (1994). Algorithms for the estimation of phase stability in heterogeneous thermodynamic systems. *Geochimica et Cosmochimica Acta*, 58(24), 5489–5501. [https://doi.org/10.1016/0016-7037\(94\)90245-3](https://doi.org/10.1016/0016-7037(94)90245-3)
- Ghiorso, M. S., & Sack, R. O. (1995). Chemical mass transfer in magmatic processes: IV. A revised and internally consistent thermodynamic model for the interpolation and extrapolation of liquid-solid equilibria in magmatic systems at elevated temperatures and pressures. *Contributions to Mineralogy and Petrology*, 119, 197–212.
- Goes, S., Cammarano, F., & Hansen, U. (2004). Synthetic seismic signature of thermal mantle plumes. *Earth and Planetary Science Letters*, 218, 403–419. [https://doi.org/10.1016/S0012-821X\(03\)00680-0](https://doi.org/10.1016/S0012-821X(03)00680-0)
- Gottschalk, M. (1997). Internally consistent thermodynamic data for rock-forming minerals in the system  $\text{SiO}_2\text{-TiO}_2\text{-Al}_2\text{O}_3\text{-Fe}_2\text{O}_3\text{-CaO-MgO-FeO-K}_2\text{O-Na}_2\text{O-H}_2\text{O-CO}_2$ . *European Journal of Mineralogy*, 9(1), 175–223.
- Grocholski, B., Catali, K., Shim, S.-H., & Prakapenka, V. (2012). Mineralogical effects on the detectability of the postperovskite boundary. *Proceedings of the National Academy of Sciences*, 109(7), 2275–2279.
- Grocholski, B., Shim, S.-H., & Prakapenka, V. B. (2013). Stability, metastability, and elastic properties of a dense silica polymorph, seifertite. *Journal of Geophysical Research*, 118, 4745–4757. <https://doi.org/10.1002/jgrb.50360>
- Gréaux, S., Kono, Y., Nishiyama, N., Kunimoto, T., Wada, K., & Irifune, T. (2011).  $P$ - $V$ - $T$  equation of state of  $\text{Ca}_3\text{Al}_2\text{Si}_3\text{O}_{12}$  grossular garnet. *Physics and Chemistry of Minerals*, 38, 85–94. <https://doi.org/10.1007/s00269-010-0384-1>
- Gwanmesia, G. D., Chen, G., & Liebermann, R. C. (1998). Sound velocities in  $\text{MgSiO}_3$ -garnet to 8 GPa. *Geophysical Research Letters*, 25(24), 4553–4556. <https://doi.org/10.1029/1998GL900189>
- Gwanmesia, G. D., Zhang, J., Darling, K., Kung, J., Li, B., Wang, L., Neuville, D., & Liebermann, R. C. (2006). Elasticity of polycrystalline pyrope  $\text{Mg}_3\text{Al}_2\text{Si}_3\text{O}_{12}$  to 9 GPa and 1000°C. *Physics of the Earth and Planetary Interiors*, 155, 179–190. <https://doi.org/10.1016/j.pepi.2005.10.008>
- Gwanmesia, G. D., Wang, L., Triplett, R., & Liebermann, R. C. (2009). Pressure and temperature dependence of the elasticity of pyrope-majorite [ $\text{py}_{60}\text{mj}_{40}$  and  $\text{py}_{50}\text{mj}_{50}$ ] garnets solid solution measured by ultrasonic interferometry technique. *Physics of the Earth and Planetary Interiors*, 174, 105–112. <https://doi.org/10.1016/j.pepi.2008.07.029>
- Hazen, R. M. (1976). Effects of temperature and pressure on the crystal structure of forsterite. *American Mineralogist*, 61(11–12), 1280–1293.
- Helfrich, G., & Wood, B. J. (1989). Subregular model for multicomponent solutions. *American Mineralogist*, 74(9–10), 1016–1022.
- Herzberg, C., Asimow, P. D., Arndt, N., Niu, Y., Leshner, C. M., Fitton, J. G., ... Saunders, A. D. (2007). Temperatures in ambient mantle and plumes: Constraints from basalts, picrites, and komatiites. *Geochemistry, Geophysics, Geosystems*, 8, Q02006. <https://doi.org/10.1029/2006GC001390>
- Hill, R. (1963). Elastic properties of reinforced solids: Some theoretical principles. *Journal of the Mechanics and Physics of Solids*, 11(5), 357–372. [https://doi.org/10.1016/0022-5096\(63\)90036-X](https://doi.org/10.1016/0022-5096(63)90036-X)
- Hillert, M., & Staffansson, L.-I. (1970). The regular solution model for stoichiometric phases and ionic melts. *Acta Chemica Scandinavica*, 24, 3618–3626. <https://doi.org/10.3891/acta.chem.scand.24-3618>
- Hirose, K., Fei, Y., Ma, Y., & Mao, H. (1999). The fate of subducted basaltic crust in the Earth's lower mantle. *Nature*, 397, 53–56.
- Hirose, K., Komabayashi, T., Murakami, M., & Funakoshi, K. (2001). In situ measurements of the majorite–akimotoite–perovskite phase transition boundaries in  $\text{MgSiO}_3$ . *Geophysical Research Letters*, 28(23), 4351–4354. <https://doi.org/10.1029/2001GL013549>
- Holland, T., & Powell, R. (2003). Activity–composition relations for phases in petrological calculations: An asymmetric multicomponent formulation. *Contributions to Mineralogy and Petrology*, 145(4), 492–501. <https://doi.org/10.1007/s00410-003-0464-z>
- Holland, T. J. B., & Powell, R. (1998). An internally consistent thermodynamic data set for phases of petrological interest. *Journal of Metamorphic Geology*, 16, 309–343.
- Holland, T. J. B., & Powell, R. (2011). An improved and extended internally consistent thermodynamic data set for phases of petrological interest, involving a new equation of state for solids. *Journal of Metamorphic Geology*, 29, 333–383. <https://doi.org/10.1111/j.1525-1314.2010.00923.x>

- Holland, T. J. B., Hudson, N. F. C., Powell, R., & Harte, B. (2013). New thermodynamic models and calculated phase equilibria in NCFMAS for basic and ultrabasic compositions through the transition zone into the uppermost lower mantle. *Journal of Petrology*, 54(9), 1901–1920. <https://doi.org/10.1093/petrology/egt035>
- Holzappel, C., Rubie, D. C., Frost, D. J., & Langenhorst, F. (2005). Fe-Mg interdiffusion in (Mg, Fe)SiO<sub>3</sub> perovskite and lower mantle reequilibration. *Science*, 309(5741), 1707–1710. <https://doi.org/10.1126/science.1111895>
- Huang, S., & Chen, J. (2014). Equation of state of pyrope-almandine solid solution measured using a diamond anvil cell and in situ synchrotron X-ray diffraction. *Physics of the Earth and Planetary Interiors*, 228, 88–91. <https://doi.org/10.1016/j.pepi.2014.01.014>
- Imada, S., Hirose, K., Komabayashi, T., Suzuki, T., & Ohishi, Y. (2012). Compression of Na<sub>0.4</sub>Mg<sub>0.6</sub>Al<sub>1.6</sub>Si<sub>0.4</sub>O<sub>4</sub> NAL and Ca-ferrite-type phases. *Physics and Chemistry of Minerals*, 39, 525–530. <https://doi.org/10.1007/s00269-012-0508-x>
- Inoue, T., Irifune, T., Higo, Y., Sanehira, T., Sueda, Y., Yamada, A., ... Utsumi, W. (2006). The phase boundary between wadsleyite and ringwoodite in Mg<sub>2</sub>SiO<sub>4</sub> determined by in situ X-ray diffraction. *Physics and Chemistry of Minerals*, 33, 106–114. <https://doi.org/10.1007/s00269-005-0053-y>
- Irifune, T., & Ringwood, A. E. (1987). Phase transformations in a harzburgite composition to 26 GPa: Implications for dynamical behaviour of the subducting slab. *Earth and Planetary Science Letters*, 86, 365–376.
- Irifune, T., & Ringwood, A. E. (1993). Phase transformations in subducted oceanic crust and buoyancy relationships at depths of 600–800 km in the mantle. *Earth and Planetary Science Letters*, 117, 101–110.
- Irifune, T., Nishiyama, N., Kuroda, K., Inoue, T., Isshiki, M., Utsumi, W., ... Ohtaka, O. (1998). The postspinel phase boundary in Mg<sub>2</sub>SiO<sub>4</sub> determined by in situ X-ray diffraction. *Science*, 279, 1698–1700. <https://doi.org/10.1126/science.279.5357.1698>
- Ishii, T., Kojitani, H., & Akaogi, M. (2011). Post-spinel transitions in pyrolyte and Mg<sub>2</sub>SiO<sub>4</sub> and akimotoite-perovskite transition in MgSiO<sub>3</sub>: Precise comparison by high-pressure high-temperature experiments with multi-sample cell technique. *Earth and Planetary Science Letters*, 309, 185–197. <https://doi.org/10.1016/j.epsl.2011.06.023>
- Ita, J., & King, S. D. (1994). Sensitivity of convection with an endothermic phase change to the form of governing equations, initial conditions, boundary conditions, and equation of state. *Journal of Geophysical Research*, 99(B8), 15,919–15,938.
- Ita, J., & King, S. D. (1998). The influence of thermodynamic formulation on simulations of subduction zone geometry and history. *Geophysical Research Letters*, 25(9), 1463–1466.
- Ita, J., & Stixrude, L. (1992). Petrology, elasticity and composition of the mantle transition zone. *Journal of Geophysical Research*, 97(B5), 6849–6866.
- Ito, E., & Takahashi, E. (1989). Post-spinel transformations in the system Mg<sub>2</sub>SiO<sub>4</sub>–Fe<sub>2</sub>SiO<sub>4</sub> and some geophysical implications. *Journal of Geophysical Research*, 94, 10,637–10,646.
- Ito, E., & Yamada, H. (1982). Stability relations of silicate spinels, ilmenites, and perovskites, *High pressure research in geophysics* (pp. 405–419). Tokyo, Japan: Center for Academic Publishing.
- Jackson, J. M., Sinogeikin, S. V., & Bass, J. D. (2007). Sound velocities and single-crystal elasticity of orthoenstatite to 1073 K at ambient pressure. *Physics of the Earth and Planetary Interiors*, 161, 1–12. <https://doi.org/10.1016/j.pepi.2006.11.002>
- Jacobs, M. H., & de Jong, B. H. (2007). Placing constraints on phase equilibria and thermophysical properties in the system MgO–SiO<sub>2</sub> by a thermodynamically consistent vibrational method. *Geochimica et Cosmochimica Acta*, 71, 3630–3655. <https://doi.org/10.1016/j.gca.2007.05.010>
- Jacobs, M. H. G., Schmid-Fetzer, R., & van den Berg, A. P. (2013). An alternative use of Kieffer's lattice dynamics model using vibrational density of states for constructing thermodynamic databases. *Physics and Chemistry of Minerals*, 40, 207–227. <https://doi.org/10.1007/s00269-012-0562-4>
- Jeanloz, R., & Morris, S. (1987). Is the mantle geotherm subadiabatic? *Geophysical Research Letters*, 14(4), 335–338. <https://doi.org/10.1029/GL014i004p00335>
- Jiang, F., Gwanmesia, G. D., Dyuzheva, T. I., & Duffy, T. S. (2009). Elasticity of stishovite and acoustic mode softening under high pressure by Brillouin scattering. *Physics of the Earth and Planetary Interiors*, 172, 235–240. <https://doi.org/10.1016/j.pepi.2008.09.017>
- Kantor, I., Dubrovinsky, L., McCammon, C., Steinle-Neumann, G., Kantor, A., Skorodumova, N., ... Aquilanti, G. (2009). Short-range order and Fe clustering in Mg<sub>1-x</sub>Fe<sub>x</sub>O under high pressure. *Physical Review B: Covering Condensed Matter and Materials Physics*, 80, 014204. <https://doi.org/10.1103/PhysRevB.80.014204>
- Karato, S. (1993). Importance of anelasticity in the interpretation of seismic tomography. *Geophysical Research Letters*, 20(15), 1623–1626.
- Kato, C., Hirose, K., Komabayashi, T., Ozawa, H., & Ohishi, Y. (2013). NAL phase in K-rich portions of the lower mantle. *Geophysical Research Letters*, 40, 5085–5088. <https://doi.org/10.1002/grl.50966>
- Kato, T., Kinoshita, Y., Nishiyama, N., Wada, K., Zhou, C., & Irifune, T. (2014). Magnesium silicate perovskite coexisting with ringwoodite in harzburgite stagnated at the lowermost mantle transition zone. *Physics of the Earth and Planetary Interiors*, 232, 26–29. <https://doi.org/10.1016/j.pepi.2014.03.009>
- Katsura, T., & Ito, E. (1989). The system Mg<sub>2</sub>SiO<sub>4</sub>–Fe<sub>2</sub>SiO<sub>4</sub> at high pressure and temperatures: Precise determination of stability of olivine, modified spinel. *Journal of Geophysical Research*, 94, 15,663–15,670.
- Katsura, T., Yamada, H., Shinmei, T., Kubo, A., Ono, S., Kanzaki, M., ... Utsumi, W. (2003). Post-spinel transition in Mg<sub>2</sub>SiO<sub>4</sub> determined by high P–T in situ X-ray diffractometry. *Physics of the Earth and Planetary Interiors*, 136, 11–24.
- Katsura, T., Yamada, H., Nishikawa, O., Song, M., Kubo, A., Shinmei, T., ... Funakoshi, K. (2004). Olivine-wadsleyite transition in the system (Mg, Fe)<sub>2</sub>SiO<sub>4</sub>. *Journal of Geophysical Research*, 109, B02209. <https://doi.org/10.1029/2003JB002438>
- Katsura, T., Yokoshi, S., Kawabe, K., Shatskiy, A., Manthilake, M. A. G. M., Zhai, S., ... Funakoshi, K. (2009). P–V–T relations of MgSiO<sub>3</sub> perovskite determined by in situ X-ray diffraction using a large-volume high-pressure apparatus. *Geophysical Research Letters*, 36, L01305. <https://doi.org/10.1029/2008GL035658>
- Katsura, T., Yoneda, A., Yamazaki, D., Yoshino, T., & Ito, E. (2010). Adiabatic temperature profile in the mantle. *Physics of the Earth and Planetary Interiors*, 183, 212–218. <https://doi.org/10.1016/j.pepi.2010.07.001>
- Kellogg, L. H., & Turcotte, D. L. (1990). Mixing and the distribution of heterogeneities in a chaotically convecting mantle. *Journal of Geophysical Research*, 95(B1), 421–432. <https://doi.org/10.1029/JB095iB01p00421>
- Kellogg, L. H., Hager, B. H., & van der Hilst, R. D. (1999). Compositional stratification in the deep mantle. *Science*, 283(5409), 1881–1884. <https://doi.org/10.1126/science.283.5409.1881>
- Kennett, B. L. N., & Bunge, H.-P. (2008). *Geophysical continua: Deformation in the Earth's interior*. Cambridge, UK: Cambridge University Press.
- Kennett, B. L. N., & Jackson, I. (2009). Optimal equations of state for mantle minerals from simultaneous non-linear inversion of multiple datasets. *Physics of the Earth and Planetary Interiors*, 176, 98–108. <https://doi.org/10.1016/j.pepi.2009.04.005>
- Kennett, B. L. N., Engdahl, E. R., & Buland, R. (1995). Constraints on seismic velocities in the Earth from traveltimes. *Geophysical Journal International*, 122, 108–124.



- Kieffer, S. W. (1979a). Thermodynamics and lattice vibrations of minerals: 1. Mineral heat capacities and their relationships to simple lattice vibrational models. *Reviews of Geophysics and Space Physics*, 17(1), 1–19.
- Kieffer, S. W. (1979b). Thermodynamics and lattice vibrations of minerals: 2. Vibrational characteristics of silicates. *Reviews of Geophysics and Space Physics*, 17(1), 20–34.
- Kim, Y., Miller, M. S., Pearce, F., & Clayton, R. W. (2012). Seismic imaging of the Cocos plate subduction zone system in central Mexico. *Geochemistry, Geophysics, Geosystems*, 13, Q07001. <https://doi.org/10.1029/2012GC004033>
- Klemme, S., & O'Neill, H. S. (2000). The near-solidus transition from garnet lherzolite to spinel lherzolite. *Contributions to Mineralogy and Petrology*, 138(3), 237–248. <https://doi.org/10.1007/s004100050560>
- Kobayashi, Y., Kondo, T., Ohtani, E., Hirao, N., Miyajima, N., Yagi, T., ... Kikegawa, T. (2005). Fe-Mg partitioning between (Mg, Fe)SiO<sub>3</sub> post-perovskite, perovskite, and magnesio-wüstite in the Earth's lower mantle. *Geophysical Research Letters*, 32, L19301. <https://doi.org/10.1029/2005GL023257>
- Kono, Y., Gréaux, S., Higo, Y., Ohfuji, H., & Irifune, T. (2010). Pressure and temperature dependences of elastic properties of grossular garnet up to 17 GPa and 1650 K. *Journal of Earth Science*, 21(5), 782–791. <https://doi.org/10.1007/s12583-010-0112-2>
- Kozioł, A. M., & Newton, R. C. (1988). Redetermination of the anorthite breakdown reaction and improvement of the plagioclase-garnet-Al<sub>2</sub>SiO<sub>5</sub>-quartz geobarometer. *American Mineralogist*, 73, 216–223.
- Kudoh, Y., & Takeuchi, Y. (1985). The crystal structure of forsterite Mg<sub>2</sub>SiO<sub>4</sub> under high pressure up to 149 kbar. *Zeitschrift für Kristallographie*, 171, 291–302.
- Kung, J., Li, B., Uchida, T., Wang, Y., Neuville, D., & Liebermann, R. C. (2004). In situ measurements of sound velocities and densities across the orthopyroxene to high-pressure clinopyroxene transition in MgSiO<sub>3</sub> at high pressure. *Physics of the Earth and Planetary Interiors*, 147, 27–44. <https://doi.org/10.1016/j.pepi.2004.05.008>
- Kurnosov, A., Marquardt, H., Frost, D., Ballaran, T. B., & Ziberna, L. (2017). Evidence for a Fe<sup>3+</sup>-rich pyrolytic lower mantle from Al-Fe-bridgmanite elasticity data. *Nature*, 543, 543–546. <https://doi.org/10.1038/nature21390>
- Lacivita, V., Erba, A., Dovesi, R., & D'Arco, P. (2014). Elasticity of grossular-andradite solid solution: An ab initio investigation. *Physical Chemistry, Chemical Physics*, 16(29), 15,331–15,338.
- Li, B., & Zhang, J. (2005). Pressure and temperature dependence of elastic wave velocity of MgSiO<sub>3</sub> perovskite and the composition of the lower mantle. *Physics of the Earth and Planetary Interiors*, 151, 143–154. <https://doi.org/10.1016/j.pepi.2005-02-004>
- Li, M., & McNamara, A. K. (2013). The difficulty for subducted oceanic crust to accumulate at the Earth's core-mantle boundary. *Journal of Geophysical Research: Solid Earth*, 118, 1807–1816. <https://doi.org/10.1002/jgrb.50156>
- Litasov, K. D., & Ohtani, E. (2005). Phase relations in hydrous MORB at 18–28 GPa: Implications for heterogeneity of the lower mantle. *Physics of the Earth and Planetary Interiors*, 150, 239–263.
- Liu, L.-G. (1977). High pressure NaAlSiO<sub>4</sub>: The first silicate calcium ferrite isotype. *Geophysical Research Letters*, 4(5), 183–186. <https://doi.org/10.1029/GL004i005p00183>
- Liu, Z., Irifune, T., Gréaux, S., Arimoto, T., Shinmei, T., & Higo, Y. (2015). Elastic wave velocity of polycrystalline Mg<sub>80</sub>Py<sub>20</sub> garnet to 21 GPa and 2000 K. *Physics and Chemistry of Minerals*, 42, 213–222. <https://doi.org/10.1007/s00269-014-0712-y>
- Loewenstein, W. (1954). Configurational entropy of binary silicate solid solutions. *American Mineralogist*, 39, 92–96.
- Maguire, R., Ritsema, J., van Keken, P. E., Fichtner, A., & Goes, S. (2016). P- and S-wave delays caused by thermal plumes. *Geophysical Journal International*, 206(2), 1169–1178. <https://doi.org/10.1093/gji/ggw187>
- Maierová, P., Chust, T., Steinle-Neumann, G., Čadež, O., & Čížková, H. (2012). The effect of variable thermal diffusivity on kinematic models of subduction. *Journal of Geophysical Research*, 117, B07202. <https://doi.org/10.1029/2011JB009119>
- Mao, Z., Fan, D., Lin, J.-F., Yang, J., Tkachev, S. N., Zhuravlev, K., & Prakapenka, V. B. (2015). Elasticity of single-crystal olivine at high pressures and temperatures. *Earth and Planetary Science Letters*, 426, 204–215. <https://doi.org/10.1016/j.epsl.2015.06.045>
- Matas, J. (1999). Modélisation thermochimique des propriétés de solides à hautes températures et hautes pressions (PhD. Thesis). Lyon, France: Charles University Prague and École Normale Supérieure Lyon.
- Matas, J., & Bukowinski, M. S. T. (2007). On the anelastic contribution to the temperature dependence of lower mantle seismic velocities. *Earth and Planetary Science Letter*, 259, 51–65. <https://doi.org/10.1016/j.epsl.2007.04.028>
- Matas, J., Bass, J., Ricard, Y., Mattern, E., & Bukowinski, M. S. T. (2007). On the bulk composition of the lower mantle: Predictions and limitations from generalized inversion of radial seismic profiles. *Geophysical Journal International*, 170, 764–780.
- Matsuzaka, K., Akaogi, M., Suzuki, T., & Suda, T. (2000). Mg-Fe partitioning between silicate spinel and magnesio-wüstite at high pressure: experimental determination and calculation of phase relations in the system Mg<sub>2</sub>SiO<sub>4</sub>-Fe<sub>2</sub>SiO<sub>4</sub>. *Physics Chemistry Mineralogy*, 27(5), 310–319.
- McBride, B. J., Zehe, M. J., & Gordon, S. (2002). NASA Glenn coefficients for calculating thermodynamic properties of individual species (NASA/TP 2002-211556). Cleveland, Ohio: NASA Glenn Research Center.
- McCammon, C., Dubrovinsky, L., Narygina, O., Kantor, I., Wu, X., Glazyrin, K., ... Chumakov, A. (2010). Low-spin Fe<sup>2+</sup> in silicate perovskite and a possible layer at the base of the lower mantle. *Physics of the Earth and Planetary Interiors*, 180, 215–221. <https://doi.org/10.1016/j.pepi.2009.10.012>
- McDonough, W. F., & Sun, S. S. (1995). The composition of the Earth. *Chemical Geology*, 120, 223–253.
- Miyajima, N., Fujino, K., Funamori, N., Kondo, T., & Yagi, T. (1999). Garnet-perovskite transformation under conditions of the Earth's lower mantle: An analytical transmission electron microscopy study. *Physics of the Earth and Planetary Interiors*, 116, 117–131.
- Montagner, J., & Kennett, B. (1996). How to reconcile body-wave and normal-mode reference Earth models. *Geophysical Journal International*, 125(1), 229–248. <https://doi.org/10.1111/j.1365-246X.1996.tb06548.x>
- Morishima, H., Ohtani, E., Kato, T., Shimomura, O., & Kikegawa, T. (1994). Thermal expansion of MgSiO<sub>3</sub> perovskite at 20.5 GPa. *Geophysical Research Letters*, 21(10), 899–902.
- Morishima, H., Ohtani, E., Kato, T., Kubo, T., Suzuki, A., Kikegawa, T., & Shimomura, O. (1999). The high-pressure and temperature equation of state of a majorite solid solution in the system of Mg<sub>4</sub>Si<sub>4</sub>O<sub>12</sub>-Mg<sub>3</sub>Al<sub>2</sub>Si<sub>3</sub>O<sub>12</sub>. *Physics and Chemistry of Minerals*, 27, 3–10.
- Muggianu, Y.-M., Gambino, M., & Bros, J.-P. (1975). Enthalpies de formation des alliages liquides Bismuth-Étain-Gallium à 723 K. choix d'une représentation analytique des grandeurs d'excès intégrales et partielles de mélange. *Journal de Chimie Physique et de Physico-Chimie Biologique*, 72(1), 83–88.
- Mukhopadhyay, B., Basu, S., & Holdaway, M. J. (1993). A discussion of Margules-type formulations for multicomponent solutions with a generalized approach. *Geochimica et Cosmochimica Acta*, 57(2), 277–283. [https://doi.org/10.1016/0016-7037\(93\)90430-5](https://doi.org/10.1016/0016-7037(93)90430-5)
- Murakami, M., & Hirose, K. (2005). Post-perovskite phase transition and mineral chemistry in the pyrolytic lowermost mantle. *Geophysical Research Letters*, 32, L03304. <https://doi.org/10.1029/2004GL021956>
- Murakami, M., Sinogeikin, S. V., Hellwig, H., Bass, J. D., & Li, J. (2007). Sound velocity of MgSiO<sub>3</sub> perovskite to Mbar pressure. *Earth and Planetary Science Letters*, 256, 47–54. <https://doi.org/10.1016/j.epsl.2007-01-011>

- Murakami, M., Ohishi, Y., Hirao, N., & Hirose, K. (2009). Elasticity of MgO to 130 GPa: Implications for lower mantle mineralogy. *Earth and Planetary Science Letters*, 277, 123–129. <https://doi.org/10.1016/j.epsl.2008.10.010>
- Murakami, M., Ohishi, Y., Hirao, N., & Hirose, K. (2012). A perovskitic lower mantle inferred from high-pressure, high-temperature sound velocity data. *Nature*, 485, 90–95. <https://doi.org/10.1038/nature11004>
- Murnaghan, F. D. (1944). The compressibility of media under extreme pressures. *Proceedings of the National Academy of Sciences of the United States of America*, 30, 244–247.
- Nakagawa, T., Tackley, P. J., Deschamps, F., & Connolly, J. A. D. (2009). Incorporating self-consistently calculated mineral physics into thermochemical mantle convection simulations in a 3-D spherical shell and its influence on seismic anomalies in Earth's mantle. *Geochemistry, Geophysics, Geosystems*, 10, Q03004. <https://doi.org/10.1029/2008GC002280>
- Nakagawa, T., Tackley, P. J., Deschamps, F., & Connolly, J. A. (2010). The influence of MORB and harzburgite composition on thermo-chemical mantle convection in a 3-D spherical shell with self-consistently calculated mineral physics. *Earth and Planetary Science Letters*, 296, 403–412. <https://doi.org/10.1016/j.epsl.2010.05.026>
- Nakajima, Y., Frost, D. J., & Rubie, D. C. (2012). Ferrous iron partitioning between magnesium silicate perovskite and ferropericlase and the composition of perovskite in the Earth's lower mantle. *Journal of Geophysical Research*, 117, B08201. <https://doi.org/10.1029/2012JB009151>
- Newton, R., Charlu, T., Anderson, P., & Kleppa, O. (1979). Thermochemistry of synthetic clinopyroxenes on the join  $\text{CaMgSi}_2\text{O}_6\text{--Mg}_2\text{Si}_2\text{O}_6$ . *Geochimica et Cosmochimica Acta*, 43, 55–60.
- O'Brien, P. J., & Rötzler, J. (2003). High-pressure granulites: Formation, recovery of peak conditions and implications for tectonics. *Journal of Metamorphic Geology*, 21(1), 3–20.
- Ohta, K., Hirose, K., Lay, T., Sata, N., & Ohishi, Y. (2008). Phase transitions in pyrolite and MORB at lowermost mantle conditions: Implications for a MORB-rich pile above the core-mantle boundary. *Earth and Planetary Science Letters*, 267, 107–117. <https://doi.org/10.1016/j.epsl.2007.11.037>
- Ohtani, E., Kagawa, N., & Fujino, K. (1991). Stability of majorite ( $\text{Mg, FeSiO}_3$ ) at high pressures and 1800°C. *Earth and Planetary Science Letters*, 102, 158–166.
- Ohtani, H. (2006). The CALPHAD method, *Springer handbook of materials measurement methods, chap. E* pp. 1001–1030. Berlin: Springer. [https://doi.org/10.1007/978-3-540-30300-8\\_20](https://doi.org/10.1007/978-3-540-30300-8_20)
- Olinger, B. (1977). Compression studies of forsterite ( $\text{Mg}_2\text{SiO}_4$ ) and enstatite ( $\text{MgSiO}_3$ ). *High-pressure research: Applications in geophysics* (pp. 325–334). New York: Academic.
- O'Neill, B., Bass, J., Smyth, J., & Vaughan, M. (1989). Elasticity of a grossular-pyrope-almandine garnet. *Journal of Geophysical Research*, 94(17), 819. <https://doi.org/10.1029/JB094iB12p17819>
- Ono, S., & Oganov, A. R. (2005). In situ observations of phase transition between perovskite and  $\text{CaIrO}_3$ -type phase in  $\text{MgSiO}_3$  and pyrolitic mantle composition. *Earth and Planetary Science Letters*, 236, 914–932. <https://doi.org/10.1016/j.epsl.2005.06.001>
- Ono, S., Katsura, T., Ito, E., Kanzaki, M., Yoneda, A., Walter, M. J., ... Funakoshi, K. (2001). In situ observation of ilmenite-perovskite phase transition in  $\text{MgSiO}_3$  using synchrotron radiation. *Geophysical Research Letters*, 28(5), 835–838. <https://doi.org/10.1029/1999GL008446>
- Ono, S., Hirose, K., Murakami, M., & Isshiki, M. (2002). Post-stishovite phase boundary in  $\text{SiO}_2$  determined by in situ X-ray observations. *Earth and Planetary Science Letters*, 197, 187–192.
- Pamato, M. G., Kurnosov, A., Ballaran, T. B., Frost, D. J., Ziberna, L., Giannini, M., ... Prakapenka, V. B. (2016). Single crystal elasticity of majoritic garnets: Stagnant slabs and thermal anomalies at the base of the transition zone. *Earth and Planetary Science Letters*, 451, 114–124. <https://doi.org/10.1016/j.epsl.2016.07.019>
- Pavese, A., Diella, V., Pischedda, V., Merli, M., Bocchio, R., & Mezouar, M. (2001). Pressure-volume-temperature equation of state of andradite and grossular, by high-pressure and -temperature powder diffraction. *Physics and Chemistry of Minerals*, 28, 242–248.
- Peacock, S. M., van Keken, P. E., Holloway, S. D., Hacker, B. R., Abers, G. A., & Fergason, R. L. (2005). Thermal structure of the Costa Rica–Nicaragua subduction zone. *Physics of the Earth and Planetary Interiors*, 149, 187–200. <https://doi.org/10.1016/j.pepi.2004.08.030>
- Pelton, A. D. (2001). A general “geometric” thermodynamic model for multicomponent solutions. *Calphad*, 25(2), 319–328. [https://doi.org/10.1016/S0364-5916\(01\)00052-9](https://doi.org/10.1016/S0364-5916(01)00052-9)
- Piazzoni, A. S., Steinle-Neumann, G., Bunge, H.-P., & Dolejš, D. (2007). A mineralogical model for density and elasticity of the Earth's mantle. *Geochemistry, Geophysics, Geosystems*, 8(11), Q11010. <https://doi.org/10.1029/2007GC001697>
- Poirier, J.-P. (2000). *Introduction to the physics of the earth's interior* (2edn.). New York: Cambridge University Press.
- Powell, R. (1974). A comparison of some mixing models for crystalline silicate solid solutions. *Contributions to Mineralogy and Petrology*, 46(4), 265–274. <https://doi.org/10.1007/BF00370967>
- Powell, R. (1987). Darken quadratic formalism and the thermodynamics of minerals. *American Mineralogist*, 72(1–2), 1–11.
- Powell, R., & Holland, T. (1993). On the formulation of simple mixing models for complex phases. *American Mineralogist*, 78(11–12), 1174–1180.
- Powell, R., & Holland, T. J. B. (1985). An internally consistent thermodynamic dataset with uncertainties and correlations: 1. Methods and worked example. *Journal of Metamorphic Geology*, 3(4), 327–342. <https://doi.org/10.1111/j.1525-1314.1985.tb00324.x>
- Powell, R., Holland, T. J. B., & Worley, B. (1998). Calculating phase diagrams involving solid solutions via non-linear equations, with examples using THERMOCALC. *Journal of Metamorphic Geology*, 16, 577–588.
- Prescher, C., Langenhorst, F., Dubrovinsky, L. S., Prakapenka, V. B., & Miyajima, N. (2014). The effect of Fe spin crossovers on its partitioning behavior and oxidation state in a pyrolitic Earth's lower mantle system. *Earth and Planetary Science Letters*, 399, 86–91. <https://doi.org/10.1016/j.epsl.2014.05.011>
- Presnall, D. C., & Hoover, J. D. (1987). High pressure phase equilibria constraints on the origin of mid-ocean ridge basalts. In B. O. Mysen (Ed.), *Magmatic processes: Physicochemical principles* (pp. 75–89). University Park, PA: Geochemical Society.
- Presnall, D. C., Weng, Y.-H., Millholland, C. S., & Walter, M. J. (1998). Liquidus phase relations in the system  $\text{MgO--MgSiO}_3$  at pressures up to 25 GPa—Constraints on crystallization of a molten haden mantle. *Physics of the Earth and Planetary Interiors*, 107, 83–95. [https://doi.org/10.1016/S0031-9201\(97\)00126-X](https://doi.org/10.1016/S0031-9201(97)00126-X)
- Putnis, A. (1992). *An introduction to mineral sciences*. New York: Cambridge University Press.
- Ricard, Y., Mattern, E., & Matas, J. (2005). Synthetic tomographic images of slabs from mineral physics. In R. D. Van Der Hilst, J. D. Bass, J. Matas, & J. Trampert (Eds.), *Earth's deep mantle: structure, composition, and evolution* (pp. 283–300). Washington, DC: American Geophysical Union. <https://doi.org/10.1029/160GM17>
- Ricolléau, A., Fei, Y., Cottrell, E., Watson, H., Deng, L., Fiquet, L. Z. G., ... Prakapenka, V. (2009). Density profile of pyrolite under the lower mantle conditions. *Geophysical Research Letters*, 36, L06302. <https://doi.org/10.1029/2008GL036759>



- Riccolleau, A., Perrillat, J.-P., Fiquet, G., Daniel, I., Matas, J., Addad, A., ... Guignot, N. (2010). Phase relations and equation of state of a natural MORB: Implications for the density profile of subducted oceanic crust in the Earth's lower mantle. *Journal of Geophysical Research*, 115, B08202. <https://doi.org/10.1029/2009JB006709>
- Ritsema, J., Xu, W., Stixrude, L., & Lithgow-Bertelloni, C. (2009). Estimates of the transition zone temperature in a mechanically mixed upper mantle. *Earth and Planetary Science Letters*, 277(1–2), 244–252. <https://doi.org/10.1016/j.epsl.2008.10.024>
- Ritsema, J., Cupillard, P., Tauzin, B., Xu, W., Stixrude, L., & Lithgow-Bertelloni, C. (2009). Joint mineral physics and seismic wave traveltime analysis of upper mantle temperature. *Geology*, 37(4), 363–366. <https://doi.org/10.1130/G25428A.1>
- Robie, R. A., & Hemingway, B. S. (1995). Thermodynamic properties of minerals and related substances at 298.15 K and 1 kbar pressure and at higher temperatures. *U.S. Geological Survey Bulletin*, 2131, 461–461.
- Robie, R. A., Finch, C. B., & Hemingway, B. S. (1982). Heat capacity and entropy of fayalite ( $\text{Fe}_2\text{SiO}_4$ ) between 5.1 and 383 K: Comparison of calorimetric and equilibrium values for the QFM buffer reaction. *American Mineralogist*, 67, 463–469.
- Saikia, A., Frost, D. J., & Rubie, D. C. (2008). Splitting of the 520-kilometer seismic discontinuity and chemical heterogeneity in the mantle. *Science*, 319(5869), 1515–1518. <https://doi.org/10.1126/science.1152818>
- Sakai, T., Ohtani, E., Terasaki, H., Sawada, N., Kobayashi, Y., Miyahara, M., ... Kikegawa, T. (2009). Fe-Mg partitioning between perovskite and ferropericlase in the lower mantle. *American Mineralogist*, 94, 921–925. <https://doi.org/10.2138/am.2009.3123>
- Sarafian, E., Gaetani, E. G. A., Hauri, H., & Sarafian, A. R. (2017). Experimental constraints on the damp peridotite solidus and oceanic mantle potential temperature. *Science*, 355(6328), 942–944. <https://doi.org/10.1126/science.aaj2165>
- Sawamoto, H. (1987). *Phase diagram of  $\text{MgSiO}_3$  at pressures up to 24 GPa and temperatures up to 2200°C: Phase stability and properties of tetragonal garnet*, *Geophysical Monograph* (Vol. 39). Tokyo, Japan: Terra Scientific Publishing Company.
- Schaber, K., Bunge, H.-P., Schubert, B. S. A., Malservisi, R., & Horbach, A. (2009). Stability of the rotation axis in high-resolution mantle circulation models: Weak polar wander despite strong core heating. *Geochemistry, Geophysics, Geosystems*, 10(11), Q11W04. <https://doi.org/10.1029/2009GC002541>
- Schubert, B. S. A., Bunge, H.-P., & Ritsema, J. (2009a). Tomographic filtering of high-resolution mantle circulation models: Can seismic heterogeneity be explained by temperature alone? *Geochemistry, Geophysics, Geosystems*, 10, Q05W03. <https://doi.org/10.1029/2009GC002401>
- Schubert, B. S. A., Bunge, H.-P., Steinle-Neumann, G., Moder, C., & Oeser, J. (2009b). Thermal versus elastic heterogeneity in high-resolution mantle circulation models with pyrolite composition: High plume excess temperatures in the lowermost mantle. *Geochemistry, Geophysics, Geosystems*, 10(1), Q01W01. <https://doi.org/10.1029/2008GC002235>
- Schubert, B. S. A., Zanolli, C., & Nolet, G. (2012). Synthetic seismograms for a synthetic Earth: Long-period P- and S-wave traveltime variations can be explained by temperature alone. *Geophysical Journal International*, 188, 1393–1412. <https://doi.org/10.1111/j.1365-246X.2011.05333.x>
- Schubert, B. S. A., Zanolli, C., & Nolet, G. (2015). Traveltime dispersion in an isotropic elastic mantle: Strong lower-mantle signal in differential-frequency residuals. *Geophysical Journal International*, 203, 2099–2118. <https://doi.org/10.1093/gji/ggv389>
- Shapiro, N., Olsen, K. B., & Singh, S. (2000). Wave-guide effects in subduction zones: Evidence from three-dimensional modeling. *Geophysical Research Letters*, 27(3), 433–436.
- Shieh, S. R., & Duffy, T. S. (2002). Strength and elasticity of  $\text{SiO}_2$  across the stishovite— $\text{CaCl}_2$ -type structural phase boundary. *Physical Review Letters*, 89(25), 255507. <https://doi.org/10.1103/PhysRevLett.89.255507>
- Shimozuku, A., Kubo, T., Ohtani, E., Nakamura, T., Okazaki, R., Dohmen, R., & Chakraborty, S. (2009). Si and O diffusion in  $(\text{Mg}, \text{Fe})_2\text{SiO}_4$  wadsleyite and ringwoodite and its implications for the rheology of the mantle transition zone. *Earth and Planetary Science Letters*, 284, 103–112. <https://doi.org/10.1016/j.epsl.2009.04.014>
- Simmons, N. A., Forte, A. M., & Grand, S. P. (2009). Joint seismic, geodynamic and mineral physical constraints on three-dimensional mantle heterogeneity: Implications for the relative importance of thermal versus compositional heterogeneity. *Geophysical Journal International*, 177, 1284–1304. <https://doi.org/10.1111/j.1365-246X.2009.04133.x>
- Sinmyo, R., & Hirose, K. (2013). Iron partitioning in pyrolytic lower mantle. *Physics and Chemistry of Minerals*, 40, 107–113. <https://doi.org/10.1007/s00269-012-0551-7>
- Sinogeikin, S., Katsura, T., & Bass, J. (1998). Sound velocities and elastic properties of Fe-bearing wadsleyite and ringwoodite. *Journal of Geophysical Research*, 103(B9), 20,819–20,825. <https://doi.org/10.1029/98JB01819>
- Sinogeikin, S. V., & Bass, J. D. (2002a). Elasticity of pyrope and majorite-pyrope solid solutions to high temperatures. *Earth and Planetary Science Letters*, 203, 549–555. [https://doi.org/10.1016/S0012-821X\(02\)00851-8](https://doi.org/10.1016/S0012-821X(02)00851-8)
- Sinogeikin, S. V., & Bass, J. D. (2002b). Elasticity of majorite and a majorite-pyrope solid solution to high pressure: Implications for the transition zone. *Geophysical Research Letters*, 29(2), 1017. <https://doi.org/10.1029/2001GL013937>
- Sinogeikin, S. V., Bass, J. D., & Katsura, T. (2003). Single-crystal elasticity of ringwoodite to high pressures and high temperatures: Implications for 520 km seismic discontinuity. *Physics of the Earth and Planetary Interiors*, 136, 41–66. [https://doi.org/10.1016/S0031-9201\(03\)00022-0](https://doi.org/10.1016/S0031-9201(03)00022-0)
- Sohl, F., & Schubert, G. (2015). Interior structure, composition, and mineralogy of the terrestrial planets, *Treatise on Geophysics* (Vol. 10, chap. 10.02, pp. 23–64). Amsterdam, Netherlands: Elsevier.
- Spielman, D., & Teng, S.-H. (2001). Smoothed analysis of algorithms: Why the simplex algorithm usually takes polynomial time, *Proceedings of the 33rd Annual ACM Symposium on Theory of Computing, STOC '01* (pp. 296–305). New York: ACM. <https://doi.org/10.1145/380752.380813>
- Stacey, F. D., & Davis, P. M. (2008). *Physics of the Earth* (4th ed.). New York: Cambridge University Press.
- Stixrude, L., & Lithgow-Bertelloni, C. (2005a). Thermodynamics of mantle minerals: I. Physical properties. *Geophysical Journal International*, 162(2), 610–632. <https://doi.org/10.1111/j.1365-246X.2005.02642.x>
- Stixrude, L., & Lithgow-Bertelloni, C. (2005b). Mineralogy and elasticity of the oceanic upper mantle: Origin of the low-velocity zone. *Journal of Geophysical Research*, 110, B03204. <https://doi.org/10.1029/2004JB002965>
- Stixrude, L., & Lithgow-Bertelloni, C. (2011). Thermodynamics of mantle minerals: II. Phase equilibria. *Geophysical Journal International*, 184, 1180–1213. <https://doi.org/10.1111/j.1365-246X.2010.04890.x>
- Stowe, K. (2007). *An introduction to thermodynamics and statistical mechanics* (2 edn.). Cambridge, UK: Cambridge University Press.
- Styles, E., Davies, D. R., & Goes, S. (2011). Mapping spherical seismic into physical structure: Biases from 3-D phase-transition and thermal boundary-layer heterogeneity. *Geophysical Journal International*, 184(3), 1371–1378. <https://doi.org/10.1111/j.1365-246X.2010.04914.x>
- Suzuki, A., Ohtani, E., Morishima, H., Kubo, T., Kanbe, Y., Kondo, T., ... Kikegawa, T. (2000). In situ determination of the phase boundary between wadsleyite and ringwoodite in  $\text{Mg}_2\text{SiO}_4$ . *Geophysical Research Letters*, 27(6), 803–806. <https://doi.org/10.1029/1999GL008425>
- Swamy, V., Saxena, S. K., Sundman, B., & Zhang, J. (1994). A thermodynamic assessment of silica phase diagram. *Journal of Geophysical Research*, 99(B6), 11,787–11,794.

- Syracuse, E. M., van Keken, P. E., & Abers, G. A. (2010). The global range of subduction zone thermal models. *Physics of the Earth and Planetary Interiors*, 183, 73–90. <https://doi.org/10.1016/j.pepi.2010.02.004>
- Tackley, P. J. (2011). Living dead slabs in 3-D: The dynamics of compositionally-stratified slabs entering a “slab graveyard” above the core-mantle boundary. *Physics of the Earth and Planetary Interiors*, 188(3–4S1), 150–162. <https://doi.org/10.1016/j.pepi.2011.04.013>
- Tateno, S., Hirose, K., Sata, N., & Ohishi, Y. (2009). Determination of post-perovskite phase transition boundary up to 4400 K and implications for thermal structure in D” layer. *Earth and Planetary Science Letters*, 277, 130–136. <https://doi.org/10.1016/j.epsl.2008.10.004>
- Tesoniero, A., Cammarano, F., & Boschi, L. (2016). S-to-P heterogeneity ratio in the lower mantle and thermo-chemical implications. *Geochemistry, Geophysics, Geosystems*, 17(7), 2522–2538. <https://doi.org/10.1002/2016GC006293>
- Tirone, M., Buhre, S., Schmück, H., & Faak, K. (2016). Chemical heterogeneities in the mantle: The equilibrium thermodynamic approach. *Lithos*, 244, 140–150. <https://doi.org/10.1016/j.lithos.2015.11.032>
- Toop, G. W. (1965). Predicting ternary activities using binary data. *Transactions of the Metallurgical Society of AIME*, 233, 850–855.
- Trampert, J., Deschamps, F., Resovsky, J., & Yuen, D. (2004). Probabilistic tomography maps chemical heterogeneities throughout the lower mantle. *Science*, 306, 853–856. <https://doi.org/10.1126/science.1101996>
- Turcotte, D. L., & Schubert, G. (2002). *Geodynamics*. New York: Cambridge University Press.
- Utsumi, W., Funamori, N., Yagi, T., Ito, E., Kikegawa, T., & Shimomura, O. (1995). Thermal expansivity of  $\text{MgSiO}_3$  perovskite under high pressures up to 20 GPa. *Geophysical Research Letters*, 22(9), 1005–1008.
- Vacher, P., Mocquet, A., & Sotin, C. (1998). Computation of seismic profiles from mineral physics: The importance of the non-olivine components for explaining the 660 km depth discontinuity. *Physics of the Earth and Planetary Interiors*, 106, 275–298.
- van Keken, P. E., Hacker, B. R., Syracuse, E. M., & Abers, G. A. (2011). Subduction factory: 4. Depth-dependent flux of  $\text{H}_2\text{O}$  from subducting slabs worldwide. *Journal of Geophysical Research*, 116, B01401. <https://doi.org/10.1029/2010JB007922>
- Verhoogen, J. (1965). Phase changes and convection in the Earth’s mantle. *Philosophical Transactions of the Royal Society of London*, 258(1088), 276–283.
- Vinograd, V. L. (2001). Configurational entropy of binary solid solutions, *EMU notes in mineralogy: Solid solutions in silicate and oxide systems* (Vol. 3, chap. 12, pp. 303–346). Budapest: Eötvös University Press.
- Wang, X., Tsuchiya, T., & Hase, A. (2015). Computational support for a pyrolytic lower mantle containing ferric iron. *Nature Geoscience*, 8, 556–560. <https://doi.org/10.1038/NGEO2458>
- Watanabe, H. (1982). Thermochemical properties of synthetic high-pressure compounds relevant to the Earth’s mantle. In Akimoto, S., & Manghnani, M. H. (Eds.), *High-pressure research in geophysics, advances in earth and planetary sciences* (Vol. 12, pp. 441–464). Tokyo, Japan: Center for Academic Publications.
- Weidner, D. J. (1985). A mineral physics test of a pyrolytic mantle. *Geophysical Research Letters*, 12(7), 417–420.
- Wen, S., & Nekvasil, H. (1994). SOLVCALC: An interactive graphics program package for calculating the ternary feldspar solvus and for two-feldspar geothermometry. *Computers and Geosciences*, 9, 1025–1040.
- Wessel, P., Smith, W. H. F., Scharroo, R., Luis, J., & Wobbe, F. (2013). Generic mapping tools: Improved version released. *Eos Transactions, American Geophysical Union*, 94(45), 409–410.
- White, W. B., Johnson, S. M., & Dantzig, G. B. (1958). Chemical equilibrium in complex mixtures. *Journal of Chemical Physics*, 28(5), 751–755. <https://doi.org/10.1063/1.1744264>
- Will, G., Hoffbauer, W., Hinze, E., & Lauterjung, J. (1986). The compressibility of forsterite up to 300 kbar measured with synchrotron radiation. *Physica B*, 139–140, 193–197.
- Workman, R. K., & Hart, S. R. (2005). Major and trace element composition of the depleted MORB mantle. *Earth and Planetary Science Letters*, 231(1–2), 53–72. <https://doi.org/10.1016/j.epsl.2004.12.005>
- Xu, W., Lithgow-Bertelloni, C., Stixrude, L., & Ritsema, J. (2008). The effect of bulk composition and temperature on mantle seismic structure. *Earth and Planetary Science Letters*, 275, 70–79. <https://doi.org/10.1016/j.epsl.2008.08.012>
- Yagi, T., Akaogi, M., Shimomura, O., Suzuki, T., & Akimoto, S. (1987). In situ observation of the olivine-spinel transformation in  $\text{Fe}_2\text{SiO}_4$  using synchrotron radiation. *Journal of Geophysical Research*, 92, 6207–6213.
- Zha, C.-S., Mao, H.-K., & Hemley, R. J. (2000). Elasticity of  $\text{MgO}$  and a primary pressure scale to 55 GPa. *Proceedings of the National Academy of Sciences*, 97(25), 13,494–13,499. <https://doi.org/10.1073/pnas.240466697>
- Zhang, J., Liebermann, R. C., Gasparik, T., Herzberg, C. T., & Fei, Y. (1993). Melting and subsolidus relations of  $\text{SiO}_2$  at 9–14 GPa. *Journal of Geophysical Research*, 98(B11), 19,785–19,793. <https://doi.org/10.1029/93JB02218>
- Zhang, L., Ahsbahs, H., Kutoglu, A., & Geiger, C. (1999). Single-crystal hydrostatic compression of synthetic pyrope, almandine, spessartine, grossular and andradite garnets at high pressures. *Physics and Chemistry of Minerals*, 27, 52–58.
- Zibera, L., Klemme, S., & Nimis, P. (2013). Garnet and spinel in fertile and depleted mantle: Insights from thermodynamic modelling. *Contributions to Mineralogy and Petrology*, 166, 411–421. <https://doi.org/10.1007/s00410-013-0882-5>
- Zou, Y., Irifune, T., Gréaux, S., Whitaker, M. L., Shinmei, T., Ohfuji, H., ... Higo, Y. (2012). Elasticity and sound velocities of polycrystalline  $\text{Mg}_3\text{Al}_2(\text{SiO}_4)_3$  garnet up to 20 GPa and 1700 K. *Journal of Applied Physics*, 112, 014910. <https://doi.org/10.1063/1.4736407>